HI JENA

Helmholtz Institute Jena

ANNUAL REPORT 2021

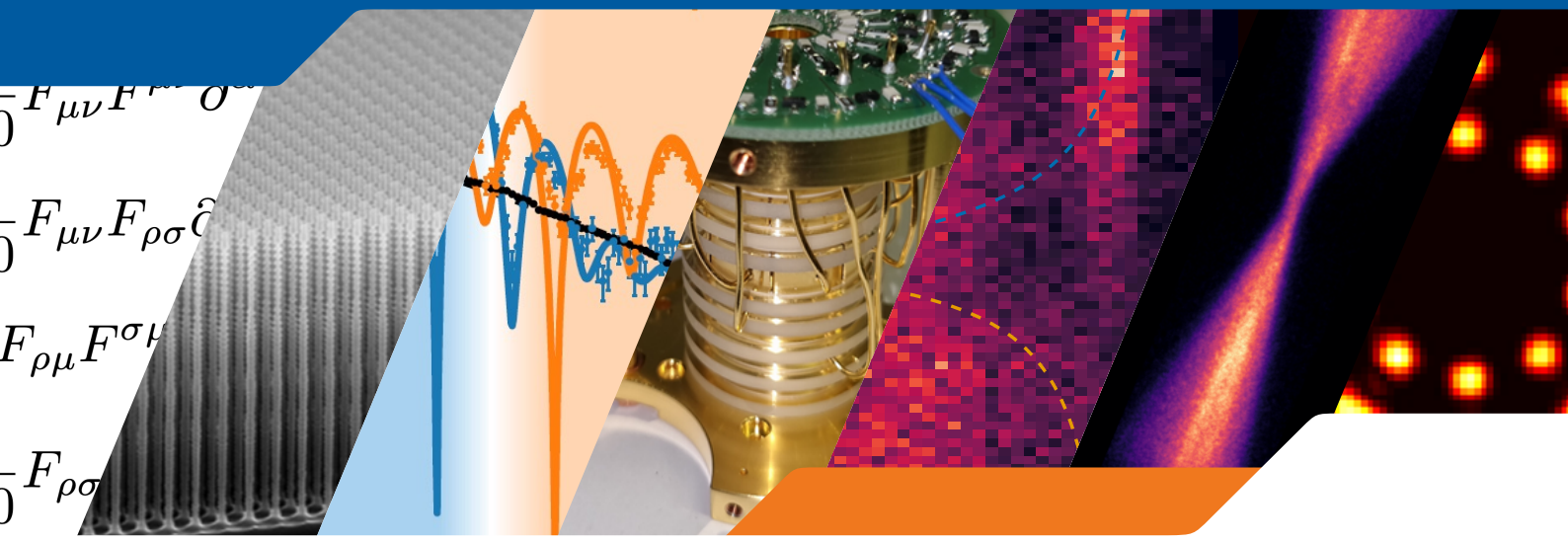

GSI

FRIEDRICH-SCHILLER-
UNIVERSITÄT
JENA

HZDR
HELMHOLTZ ZENTRUM
DRESDEN ROSSENDORF

DESY.

HELMHOLTZ INSTITUTE JENA

ANNUAL REPORT 2021

IMPRINT

Publisher:	Helmholtz-Institut Jena, Fröbelstieg 3, 07743 Jena, Germany (http://www.hi-jena.de) @ GSI Helmholtzzentrum für Schwerionenforschung GmbH Darmstadt, Germany (http://www.gsi.de) GSI is member of the Helmholtz association of national research centers (http://www.helmholtz.de).
Editors:	Daniel Seipt and Arno Klenke
DOI:	http://dx.doi.org/10.15120/GSI-2022-00212
Publication date:	July 2022

CONTENTS

FOREWORD

Dear friends and members of the Helmholtz Institute Jena,

we'd like to start this annual report with some good news: The scientific mutual exchange and life has obviously returned to the institute during recent months. While the outbreak of the pandemic in 2019 had a rather abrupt impact on our everyday lives, with home office, safety measures and emphasis on health, it also restricted the social contacts and may occasionally have affected motivation and efficiency. With advancing vaccination efforts, and a steady decrease of incidence rates, we now shall enjoy again joining physics discussions, workshops, and conferences, while still managing the risks that remain with Covid and its possible resurgence in the autumn. Carpe diem for doing good physics and science (again). Another, more somber, shadow that is currently lying over us and will likely affect many future developments, arose from Russia's attack upon the sovereign and independent Ukraine. This war not only encroaches on the territorial integrity of Ukraine but also violates our values of freedom, peace and independence as basis for all democratic developments, in science and society. It is this attack which forces us now to take position and support scientists in Ukraine, as well as Russian colleagues who may have to leave their country for political reasons.

Despite these quite serious challenges, however, research at the Helmholtz Institute has progressed actively during the past year with several – newly developed or ongoing – experiments as well as a good number of well-received publications. Strategically, the recent focus of the institute has been placed on enabling techniques for particle acceleration, quantum technology and data science. As such, HI-Jena had in 2020 joined the common effort of research institutions in Thuringia forming the "Quantum Hub Thuringia", as well as the German "Consortium for Cryogenic Detectors and Superconducting Electronics", activities which demonstrate the close contact between HI-Jena and the University of Jena, and especially with the Institutes of Quantum Optics, Solid State Physics and Theoretical Physics. These contacts also constitute a crucial part of the Helmholtz Quantum Strategy program, and in particular the Distributed Detector Lab initiative, which was positively evaluated in 2021 and has been recommended for funding. Many of these efforts are directly embedded into the research field "Matter" of the Helmholtz Association, where the institute participates in the programs "From Matter to Materials and Life" as well as in "Matter and Technology".

This continuous expansion of the institute's research program has also caused lab and office space at the institute to become increasingly scarce. Thanks to the generous support by the Federal State of Thuringia, the extension building of the HI-Jena will be inaugurated in the fall of 2022, and will provide room for further growth of HI Jena, as well as enhance the available high-power laser infrastructure. The newly-constructed building is located at the campus of the FSU Jena, in direct vicinity of the main institute building at Fröbelstieg 3, and impresses with its austere charm and panorama windows on all sides. Both buildings are readily connected via a tunnel that will facilitate the use of laser and experiment equipment from both buildings. A long-time objective of the institute has been the promotion of young scientists during their PhD studies and in the early phases of their scientific careers. Most of our doctoral students are supported by the research school RS-APS of HI Jena, whose scientific program has been continued

in 2021 despite the pandemic, though often through digital formats. In particular, the RS-APS seminars were held via Zoom, as was the annual Lecture Week of RS-APS in October 2021. The virtual four-day event saw a record attendance of 24 participants, highlighting that such opportunities for scientific exchange are sorely needed. In addition, together with the partner graduate school HGS-HIRe for FAIR, a number of dedicated soft skills series for scientists were offered by virtual workshop series. At present, the RS-APS supports 54 members, 7 of which finished their PhD in 2021. Approximately half of the students are financed by 3rd party funding.

Since its foundation in 2010, the Helmholtz Institute Jena has provided excellent research opportunities by operating own infrastructures that have proven to be highly attractive for students and young scientists. Being hosted at the campus of the FSU, the close contact of HI-Jena with the research groups from the university helped establish not only the high-power laser systems POLARIS and JETi200 but also specialized x-ray and cryo laboratories, bolstering the institute's active involvement in the strategic missions of GSI, with the Helmholtz centers DESY and HZDR as additional partners. Today, many experimental research projects are exploiting the unique research infrastructures of the large-scale facilities at GSI at Darmstadt and DESY including the flagship projects FAIR and XFEL. This Annual Report 2021 concisely documents the progress and research highlights from the last year. In addition, quite a few important R&D projects are currently pursued at the institute and reflect the important contributions by 3rd party funding.

View of the existing Helmholtz Institute Jena building together with the new laboratory and office building visible to its left (Photo by Felix Karbstein).

Status of the Research School of Advanced Photon Science

R. Märtin*[1,2], C. Hahn[1,2], G. Weber[1,2], C. Spielmann[1,3], and Th. Stöhlker[1,2,3]

[1]HI Jena, Fröbelstieg 3, 07743 Jena, Germany; [2]GSI; [3]IOQ, FSU Jena

The research school RS-APS exists now for 9 years and is a well-established institution to support the PhD projects of young researchers working at the Helmholtz Institute or at its associated Helmholtz centres.

Compared to the early days of the pandemic in 2020, the access to and the working conditions at the institute and the Helmholtz centers was improved due to adaptation to the various safety measures. The continuation of the research work has been of great importance especially for those students working on PhD projects focused on experimental work, while others had at least the possibility to continue their doctoral work from home. RS-APS also continues with its program and mission to provide doctoral students with structured PhD education. Taking the still existing safety measures into consideration while fostering the scientific exchange between the participants, the research school RS-APS continued with their entire academic program in a modified online version similar to 2020.

In October 2021 the Research School RS-APS of the Helmholtz Institute Jena organized the already ninth edition of its annual Lecture Week. Due to the Covid-19 situation the lecture week could not be held as a face-to-face event in the traditional format (see Fig. 1). Different from the previous year's installment, the online Lecture Week consisted not only of a series of lectures but was also complemented with group working sessions in the afternoon. For four days the 24 doctoral students learned about various aspects of "Novel applications triggered by modern laser technologies". RS-APS was fortunate to recruit four experts addressing subtopics of this research field: César Jauregui (IAP, University of Jena) gave an introduction to "Fundamentals of ultrafast lasers" and Vincent Bagnoud (GSI and TU Darmstadt) continued with an "Introduction to plasmas and relativistic laser–plasma interactions". Jens Osterhoff (DESY Hamburg) contributed a lecture focusing on the "Physics of Plasma and Laser-Plasma-Accelerator systems". In addition, Peter Thirolf (LMU Munich) made an excursion to "High Precision Laser Spectroscopy" and gave an inside view on the status of nuclear clocks. Overall the online version of the Lecture Week was very well received and led to fruitful discussions between students and lecturers.

*r.maertin@hi-jena.gsi.de

During the biweekly RS-APS seminar the PhD students have the possibility to present their research project in a rather casual format to other students and members of the Helmholtz Institute. The flexible online format paid off in 2021 since RS-APS encountered on average more attendees compared to the years before.

To ensure the regular supervision and discussion of the doctoral student with its supervisor regular PhD committee meetings had been installed already long before the pandemic. Nevertheless home office and decentralized working in-creased the importance of the regular exchange and hence was pushed by RS-APS even more.

The partnering Graduate School HGS-HIRe for FAIR provided the members of the school with courses to foster transferable skills, addressing topics such as career development or working in research environments.

Despite the overall success of the pandemic-adapted program the social aspect and triggered scientific exchange of face-to-face events cannot be neglected. For this reason a hybrid solution for the program for the upcoming time will be considered.

By the end of 2021, 54 PhD students were actively participating in the program of the research school of the HI Jena. 25 doctoral researchers are directly financed by the Helmholtz Institute while 29 students are third-party funded. As was the case in the first year of the pandemic (2020), seven students graduated successfully in 2021.

Two students received special honors for their scientific work. One student received the SPARC PhD Award while one student was awarded by the Giersch foundation for special achievements during the doctoral work.

Figure 1: Screenshot of the participants during the Lecture Week, conducted virtually in October 2021.

HIGH POWER LASER DEVELOPMENT

POLARIS: Laser Frontend Upgrade

M. Hornung*[1,2], M. Hellwing[1,2], F. Schorcht[1], G. A. Becker[2], M. B. Schwab[2], A. Kessler[1], J. Hein[1,2], and Malte C. Kaluza[1,2]

[1]Helmholtz Institute Jena, Fröbelstieg 3, 07743 Jena, Germany; [2]Institute of Optics and Quantum Electronics FSU Jena, 07743 Jena

The oscillator, parts of the first of two CPA stages and the temporal contrast cleaning stage of the POLARIS laser system were replaced by optimized versions. The optimized version was developed during the last three years within the ATHENA project.

The POLARIS laser [1] consists of two CPA stages and an intermediate XPW-stage to temporally clean the laser pulses before their final amplification. In order to increase the performance of the POLARIS laser system in terms of stability, temporal pulse contrast, timing jitter and spectral phase an optimized frontend was installed. Within the ATHENA (**A**ccelerator **T**echnology **HE**lmholtz i**N**fr**A**structure) project two identical frontend systems were developed [2]. One system will be shipped and installed to the PEnELOPE system located at HZDR. The second system, which is subject of this report, was developed for the POLARIS laser system.

After more than 20 years of operation the POLARIS oscillator was replaced by a commercial Kerr lens mode-locked, directly diode-pumped Yb:KGW oscillator (FLINT, Light Conversion UAB, Lithuania). The pulses are emitted with a repetition rate of 75.84 MHz and an average power of 4.58 W which correspond to a pulse energy of 60 nJ. The pulse duration is 75 fs and the pulses are emitted with a power stability $< 0.09\,\%$ during 15 hours. All parameters were significantly improved with respect to the previously used oscillator and since this device is a turn-key system, stable and simplified use of the POLARIS frontend is ensured. The previously used stretcher-compressor system for POLARIS's first CPA system was also replaced completely. The old system was limited in its stretching/compression ratio, its efficiency, its general optical performance and its mechanical stability. The recently installed pulse stretcher uses an Offner configuration with a 1480 l/mm diffraction grating. The efficiency was measured with 79 % and the oscillator seed pulse is stretched to 80 ps. The corresponding pulse compressor also uses 1480 l/mm gold gratings and has a free circular aperture of 20 mm. The angle of incidence for both devices is close to 56° and the devices are separately housed for improved stability. The combination of enlarged compression aperture and increased stretched pulse duration with respect to the formerly used system allows for a significantly increased output energy of POLARIS's first CPA stage. Once the system is finally commissioned the output energy could be further enhanced if desired.

Currently, the frontend replacement is still ongoing and the pulses were amplified with the POLARIS amplifier A1 to a pulse energy of 1.5 mJ. Measurements of the high dynamic temporal pulse structure of the compressed 115 fs (FWHM) laser pulses are shown in figure 1 and 2.

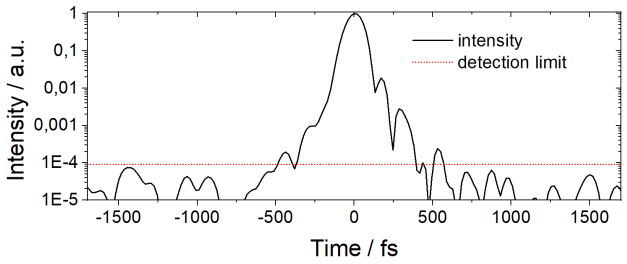

Figure 1: Wizzler measurement of the temporal pulse structure of the compressed pulses.

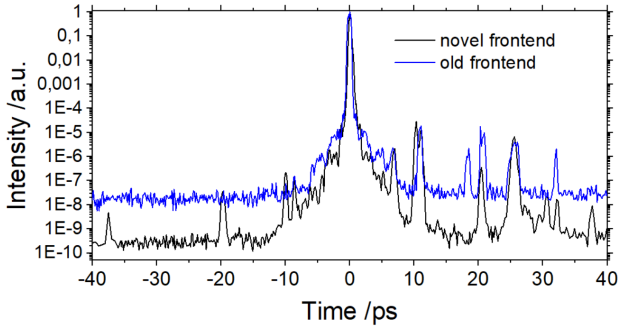

Figure 2: Preliminary temporal pulse contrast measurement before the XPW cleaning process.

The subsequent XPW system is fully assembled and the accurate position-controlled crystal mounting will ensure stable and reproducible operation. The polarization contrast of the XPW polarizers was measured with an extinction ratio better than 10^{-6} with full aperture. Assuming a conservative XPW efficiency of 10 % a temporal contrast improvement of the amplified pulses (cf. Figs. 1 and 2) of 10^5 is expected.

The next steps are to finalize and characterize the newly installed XPW stage to generate highly stable, ultra-high temporal contrast seed pulses for POLARIS's second CPA stage.

References

[1] M. Hornung *et al.*, Opt. Lett., **41**, 5413 (2016).

[2] M. Hornung *et al.*, HI Jena Annual Report, p. 14 (2020).

*M.Hornung@gsi.de

ATHENA: Frontend Development for PEnELOPE and POLARIS

M. Hornung*[1,2], D. Albach[3], G. A. Becker[2], J. Hein[1,2], M. Hellwing[1,2], A. Kessler[1], M. Löser[3], F. Schorcht[1], M. B. Schwab[2], M. Siebold[3], U. Schramm[3], and Malte C. Kaluza[1,2]

[1]Helmholtz Institute Jena, Fröbelstieg 3, 07743 Jena, Germany; [2]Institute of Optics and Quantum Electronics FSU Jena, 07743 Jena; [3]Helmholtz Center Dresden-Rossendorf, Germany

In this report we present the status of HI-Jena's contribution to the ATHENA project to develop technology for generating ultra-high intensity laser pulses with high temporal contrast. One scope of ATHENA was the development of a frontend laser system for the PEnELOPE laser system at HZDR. This system will soon be transferred from HI-Jena to HZDR.

Within the ATHENA (**A**ccelerator **T**echnology **HE**lmholtz i**N**fr**A**structure) project two basically identical frontend systems have been developed during the last three years [1]. One system will be used in the POLARIS laser system [2] and the second system, which is subject of this report, was developed for the PEnELOPE laser system [3]. This system will be shipped to and installed at the PEnELOPE laser. In order to simplify and share further developments, e.g. about the essentially required high-contrast frontends, for the diode-pumped solid-state lasers PEnELOPE and POLARIS the decision was made to use identical setups in both lasers. Due to space constraints in the POALRIS laboratories the setup of the PEnELOPE frontend system was split into two parts. The first part was the CPA system consisting of an oscillator, a pulse picking unit, a pulse stretcher, an amplifier and a pulse compressor. This system was commissioned in Jena and presented in 2019 [4]. The amplifier is shown in Figure 1.

The second part of the frontend consists of a high polarization unit and an XPW vacuum setup. This system was presented in 2020 [1] and is operational in parallel to the existing POLARIS frontend. Here we generated high temporal contrast seed-laser pulses, which can either be used for PEnELOPE or POLARIS. Without reaching the damage threshold limitations of the system, final pulse energies up to 150 µJ with a 35 nm spectral FWHM bandwidth were generated. The system exhibits high pulse to pulse stability with a repetition rate of 1 Hz at a centre wavelength of 1033 nm.

As the next step, the frontend will be transferred to the HZDR laboratories and commissioned in the PEnELOPE environment. For that, all required electronic drivers, vacuum accessories, chillers and corresponding devices were procured with respect to compatibility. Also, a full diagnostic package consisting of CCD cameras, spectrometers, photo diodes, oscilloscope and a high dynamic Wizzler for temporal pulse characterization was acquired.

For the delivery of the system the main components stretcher, compressor and amplifier were prepared in advance of the assembly with appropriate baseplates and housings. They were packed under clean conditions and finally, with all the additional required technical equipment, a bunch of four pallets and five additional boxes is currently ready for transport.

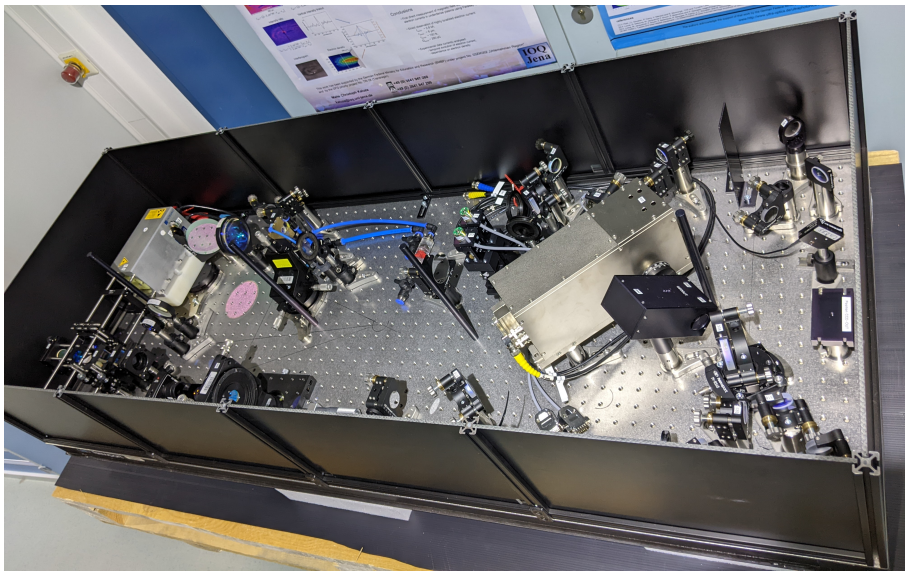

Figure 1: The amplifier section of the PEnELOPE frontend before packing and preparation for transport.

References

[1] M. Hornung *et al.*, HI Jena Annual Report, p. 14 (2020).

[2] M. Hornung *et al.*, Opt. Lett., **41**, 5413 (2016).

[3] D. Albach *et al.*, HPLSE **7**, e1 (2019).

[4] M. Hornung *et al.*, HI Jena Annual Report, p. 17 (2019).

*M.Hornung@gsi.de

1.65 mJ ultrafast coherently combined Tm-doped fiber laser system at 100 kHz repetition rate

T. Heuermann*[1,2,3], Z. Wang[1], M. Lenski[1], M. Gebhardt[1,2,3], C. Gaida[1,4], M. Abdelaal[1], J. Buldt[1], M. Müller[1,5], A. Klenke[1,2,3], and J. Limpert[1,2,3,6]

[1]IAP Jena, Albert-Einstein Straße 15, 07745 Jena, Germany; [2]HI Jena, Fröbelstieg 3, 07743 Jena, Germany; [3]GSI, Planckstraße 1 , 64291 Darmstadt, Germany; [4]Present address: Active Fiber Systems GmbH, , Ernst-Ruska Ring 17, 07743 Jena, Germany; [5]Physics department, University of Neuchatel, Avenue de Bellevaux 51, CH - 2000 Neuchatel, Switzerland; [6]Fraunhofer IOF, Albert-Einstein Straße 7, 07745 Jena, Germany

High power ultrafast laser souces in the short wavelength infrared region emitting between 1.3 µm and 4 µm have become indispensable tools in industrial applications and research. Here, we report our results on the coherent combination of 4 thulium-doped fiber amplifiers at a central wavelength of 1920 nm. The ultrafast chirped pulse amplification system produces 1.65 mJ of pulse energy at a repetition rate of 101 kHz with a pulse duration of 85 fs and a peak power of 15 GW. This system proofs the scalability of coherent combining techniques in the short wavelength infrared and paves the way towards multi-mJ, multi-100 W thulium-doped fiber lasers .

In recent years the development of high power, ultrafast laser sources around 2 µm wavelength have seen a rapid development. This is a consequence of their applicability to many wavelength regions, which well-established 1 µm sources fail to address power scalably. This holds true, amongst others, in the field of high field sciences. Here, the wavelength scaling of high harmonic generation identifies sources around 2 µm wavelength as a resonable tradeoff between efficiency and phase matched cut-off energy into the application relevant water window (300 eV-500 eV) [1]. In this wavelength region water is transparent, while biologically relevant compounds like carbon and oxygen remain opaque. Addressing this wavelength region with high photon flux could therefore be a major game changer in the fields of biological research, enabling techniques like time resolved spectroscopy [2] or coherent diffractive imaging [3] in a tabletop format to study fundamental biological processes with unprecedented resolution. Especially thulium-doped fiber lasers have been identified as an easy power-scalable solution for the generation of 2 µm radiation. Due to the excellent transparency of fused silica in this wavelength region, they can resort to fiber designs, which have proven successful in the 1 µm-wavelength region [4]. In this report we demonstrate an ultrafast Tm-doped fiber laser system emitting 1.65 mJ of pulse energy and sub-100 fs pulses at 101 kHz repetition rate. To the best of our knowledge, this represents not only the first mJ class ultrafast Tm-doped fiber laser system, but also the highest average power mJ-class SWIR laser system to date. The front end of the laser system delivers stretched pulses with a pulse duration of 1.2 ns and a pulse energy of 9 µJ. The pulses are afterwards split into 4 replicas utilizing intensity beamsplitters and launched into four Tm-doped large pitch fibers with a core diameter of around 80 µm and a length of 1.3 m [4]. Each channel amplifies the signal to a pulse energy of 495 µJ. The pulses are recombined using a similar set of intensity beam splitters and compressed in a Treacy-type compressor. The interferometer is stabilized using the LOCSET-Algorithm [5] and piezo-driven mirrors in front of the main amplifiers. The combining efficiency of this system is around 90 % and the compression efficiency is around 91 % resulting in an overall output energy of 1.65 mJ. The output pulse of the system is depicted in Figure 1. This system represents a milestone in Tm-doped fiber laser development and can enable high-power frequency conversion into the soft X-ray, THz and mid-infrared spectral region. Further power scaling of the system can not only be achieved by exploiting the scalability of coherent beam combination via adding more amplifiers channels, but also by further scaling the single channel performance by increasing the fiber core size and the stretched pulse duration. This would pave the way for multi-mJ, multi-100 W emission at around 2 µm wavelength.

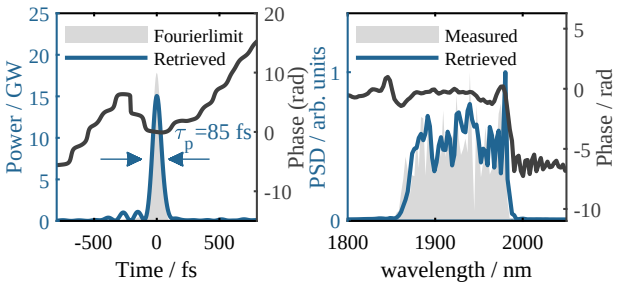

Figure 1: Reconstructed output pulse of the system measured via frequency resolved optical gating.

The authors acknowledge funding from SALT (ERC, 835306) and MIRROR (BMBF, 01DR20009A).

References

[1] D. Popmintchev *et al.*, Phys Rev Lett. **120**, 093002 (2018).

[2] N. Saito *et al.*, Optica **6**(12), 1542 (2019).

[3] J. Rothhardt *et al.*, J. Opt. **20**, 113001 (2018).

[4] J. Limpert *et al.*, Light Sci. Appl. **1**, e8 (2012).

[5] T.M. Shay *et al.*, IEEE J. on Sel. Top. Quantum Electron. **13**, 480 (2007).

*tobias.heuermann@uni-jena.de

500W average power rod-type multicore fiber CPA system

A. Klenke*[1,2], A. Steinkopff[2], C. Aleshire[2], C. Jauregui[2], S. Kuhn[3], J. Nold[3], C. Hupel[3], S. Hein[3], S. Schulze[3], S. Haarlammert[3], T. Schreiber[3], A. Tünnermann[1,2,3], and J. Limpert[1,2,3]

[1]HI Jena, Fröbelstieg 3, 07743 Jena, Germany; [2]FSU Jena, Albert-Einstein-Str. 15, 07745 Jena, Germany; [3]Fraunhofer IOF, Albert-Einstein-Str. 7, 07745 Jena, Germany

We present a femtosecond fiber laser system based on coherent combination of the output from an in-house designed rod-type multicore fiber. It delivers up to 500W of average power while maintaining a high combination efficiency of 85%.

Multicore fibers have the potential to combine the advantages of optical fibers (such as their high average power capability, high efficiency and good beam quality) with those stemming from the large beam areas commonly used in other laser architectures. Coherent combination can then be employed to achieve a single, high-quality, output beam [1]. However, to reach, and even surpass, the performance of state-of-the-art laser systems comprising multiple separate fiber amplifiers, multicore fibers need to leverage the same technological advancements. One example is the use of a rod-type geometry combined with large core diameters to mitigate detrimental nonlinear effects.

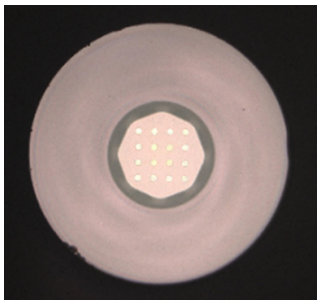

Figure 1: Image of the fiber end-facet showing the 16 cores and the octogonal cladding for guiding of the pupmp light.

We have realized an all-glass, rod-type, multicore fiber, whose basic structure is shown in figure 1. The fiber contains 16 ytterbium-doped cores in a square arrangement. An embedded octagonal fluorine-doped ring enables for pump light guidance with a NA up to 0.22. While the fiber was drawn to different sizes, the one with 21 µm diameter of the cores was chosen for the combination of femtosecond pulses, since it provided a good compromise between single-mode operation and sufficient core diameter for energy extraction. The core-to-core pitch is 58 µm in this case and the pump cladding has a diameter of 310 µm. The fiber length is 1.1 m to ensure sufficient pump absorption.

The fiber is seeded by a frontend that emits stretched femtosecond pulses with a duration of 1 ns. The incoming beam is split up into a 4x4 beam array using segmented-mirror splitters (SMS). This beam array then goes through a piezo actuator array to allow phasing of the beam for the beam combination step. Finally, the input beam array is directly imaged to the fiber cores with a 4f optical setup [2]. Due to the non-polarization maintaining structure of the fiber, waveplate arrays are inserted to ensure the same polarization state of all cores at the output of the fiber. The fiber is bi-directionally pumped with two fiber-coupled pump diodes. At the output, the beam array from the fiber is imaged again to SMS elements, here used for beam combination. A fraction of the beam arrays, resulting from the non-combining parts in the combination process, is guided towards two photodiode arrays. These arrays are connected to a multichannel phase detection system [3] that drives the piezos, located at the input. This allows for a compensation of path length mismatches in the different channels and with it for maximum output power. Finally, the combined beam passes through a grating compressor which results in the emission of femtosecond pulses at the output.

The so-called combination efficiency is determined as the main quality factor for coherent combination. It is defined as the combined output power over the total emitted linearly-polarized power coming from the fiber. In our experiments, a value of around 85% over a broad average power at 10 MHz repetition rate can be achieved. We achieve up to 507 W of average power after the compressor. Finally, the repetition rate is decreased to 687 kHz to investigate the energy scalability of the setup. In this configuration up to 412 W average power is achieved, which corresponds to 600 µJ of pulse energy. The combination efficiency drops marginally to 83% in this case.

Autocorrelation traces show a duration of 400 fs and 420 fs in the high and low repetition regimes, respectively. The M^2 measurement at full average power shows a value of less than 1.1x1.1. In summary, the presented system demonstrates a laser architecture that already shows competitive performance while also having a large scaling potential. Future developements will focus on realizing multicore fibers with larger core diameters and further increasing the channel count to scale to the multi-100 mJ pulse energy rande in combination with multi-kW average powers.

The authors acknowledge funding from BMBF PINT, FhG CAPS, ERC SALT, ESF RATI, TAB-FGR0074, DFG (416342637 and 259607349/GRK2101)

References

[1] T. Y. Fan, IEEE J. Sel. Top. Quantum Electron. **11**, 567–577 (2005).

[2] A. Klenke *et al.*, Opt. Lett. **43**, 1519-1522 (2018).

[3] A. Klenke *et al.*, Opt. Express **26**, 12072-12080 (2018).

*a.klenke@hi-jena.gsi.de

Status of mid IR high intensity laser development

J. Körner*[2], C. Anschütz[1,2], J. Reiter[2], J. Hein[1,2], and M.C. Kaluza[1,2]

[1]HI Jena, Fröbelstieg 3, 07743 Jena, Germany; [2]IOQ, FSU Jena

Scaling the wavelengths of ultra-high intensity lasers to longer wavelength offers a range of advantages compared with today's laser technology in the 1 micron wavelength range. A promising approach is using chromium doped host materials, which have a spectral characterisitic comparable to titanium sapphire but centered around 2.5 µm. The key technology required to be able to scale according laser systems to high energy are multi-Joule nanosecond pump lasers emitting around 1.8 µm. For this we develop laser systems based on thulium doped yttrium aluminum garnet (Tm:YAG). Our prototype recently achieved about 500 mJ output pulse energy from a compact unstable cavity layout.

As pump lasers for future chromium doped ultra-high intensity laser systems we developed a compact high energy q-switch laser based on thulium doped yttrium aluminum garnet (TM:YAG). The laser utilizes a novel unstable cavity approach, which uses gain shaping instead of a graded reflectivity mirror [1]. Such an approach allows for higher round-trip feedback and therefore eases the application of this technology for the low gain material Tm:YAG.

As the pump source we use a 3.5 kW laser diode stack at a center wavelength of 781 nm. The beam was homogenized to a hexagonal tophat profile using an imaging micro lens array and was imaged directly into the Tm:YAG laser crystal. The crystal was cooled to approx. 100 K to intensify the 1.88 µm emission line corresponding to the desired output wavelength [2].

The setup is shown in figure 1. To suppress the absorption of the laser radiation due to humidity in air and also to prevent condensation on the cold laser crystal surfaces the whole setup is placed in a high-vacuum chamber. The unstable resonator consists of a concave (radius 5 m) and a convex mirror (radius 4 m) in confocal configuration resulting in a cavity length of 0.5 m and a magnification of 1.2. The cavity is folded by a dichroic mirror close to the laser crystal allowing for a material double path for each half round-trip. The q-switch is realized using a rubidium titanyle phosphate (RTP) Pockels cell with an aperture of 15×15 mm^2 in combination with a quarter wave plate and a thin film polarizer.

In quasi CW operation mode the output pulse energy scaled approximately linearly with pump pulse duration, which was tested up to 3.7 ms sufficient for 1 J output energy. Up to 0.5 Hz repetition rate no significant influence of thermal effects was observed. In Q-switch operation the output energy was about 80% of the output energy under

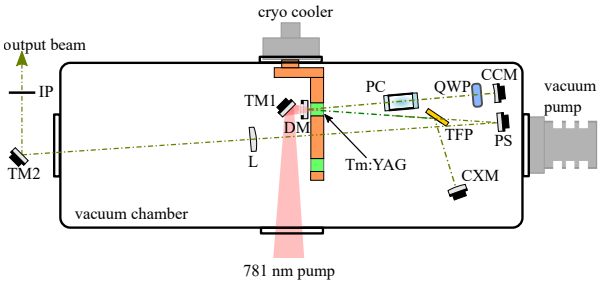

Figure 1: Schematic layout of the laser system. It is: PC...pockels cell, CCM...concave mirror (f = 2 m), CXM...convex mirror (f=2.5 m), DM...dichroic mirror, TM...turning mirror, PS...periscope, TFP...thin film polarizer, QWP...quarter wave plate, IP...image plane, L...lens (f=250 mm).

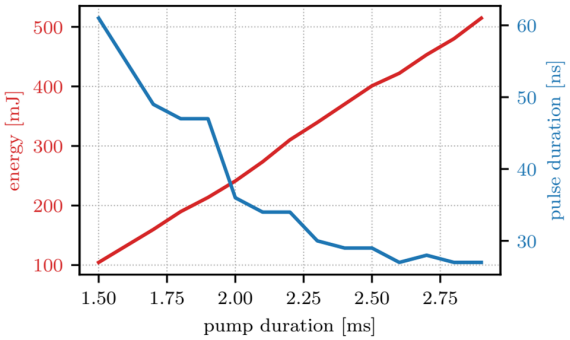

Figure 2: Output pulse energy and pulse width as function of pump duration in q-switch mode.

quasi CW operation. Stable operation was possible up to a pump duration of nearly 3 ms, resulting in more than 0.5 J output energy in a sub 30 ns pulse (c.f. figure 2). During further scaling damage occurred on the laser crystal, which seemed to be a secondary effect caused by ablation from the Pockels cell's aperture.

The achieved parameters fulfill the required parameters for a pump laser system for Cr:ZnSe (or Cr:ZnS) exceeding the TW-level. With further improvements on the setup, like a non ablating aperture of the Pockels cell, we expect to obtain output energies in excess of 1 J in the future.

References

[1] J. Körner, S. Zulić, D. Rostohar, A. Lucianetti, and T. Mocek, Optics Express **27**, 21622 (2019).

[2] J. Körner *et al.*, Journal of Luminescence **202**, 427 (2018).

* joerg.koerner@uni-jena.de

Enhancing compression factor and peak power in bulk spectral broadening using multi-pass cells

M. Seidel[1] and C. M. Heyl*[1,2,3]

[1]Deutsches Elektronen-Synchrotron DESY, Notkestrasse 85, 22607 Hamburg; [2]HI Jena, Fröbelstieg 3, 07743 Jena; [3]GSI Helmholtzzentrum für Schwerionenforschnung GmbH, Planckstrasse 1, 64291 Darmstadt

Spectral broadening and subsequent pulse compression is a highly efficient method for enhancing laser peak power and likewise increasing temporal resolution in pump-probe experiments. Post-compression based on the optical Kerr effect in bulk nonlinear media has mainly been exploited by lasers with tens of MW peak power as operation deep in the critical self-focusing regime limited the nonlinear phase. We have now demonstrated that the use of multiple thin-plates in a Herriott-type multi-pass cell overcomes the limitations posed by self-focusing, reporting more than 30 times pulse duration shortening to less than 40 fs at peak powers exceeding the GW regime. Furthermore, we have employed simulations to show that the approach is scalable to TW peak powers by rearranging the multi-pass cell employing a bow-tie configuration.

Multi-pass cells (MPCs) have leveraged nonlinear spectral broadening and post-compression to new average power and pulse energy levels as described in detail in our recent review article [1]. For lasers with peak powers around 100 MW, MPCs typically rely on cumbersome overpressure gas-filled chambers. Alternatively, solid Kerr media can be inserted into an MPC. The latter approach has been limited so-far to a nonlinear phase acumulated per pass of less than $\pi/5$, which typically resulted in moderate spectral broadening factors not exceeding 10 per stage. We hybridized the MPC technique with the multi-plate method where clearly higher nonlinear phases per Kerr medium ($\approx \pi$) were reported [2]. Our approach yielded significantly larger spectral broadening factors than achieved with either method alone (see Figure 1) [3], supporting cleanly compressed pulses with a high energy content in the main peak (see Figure 2). The method has exhibited excellent noise properties and is very robust while using only standard mirrors and anti reflection-coated windows. A basic version of our scheme was implemented in the most frequently used pump-laser at DESY's free-electron laser (FEL) user facility FLASH [4]. It has been highly reliable so-far, supporting multiple user-experiments.

*c.heyl@hi-jena.gsi.de

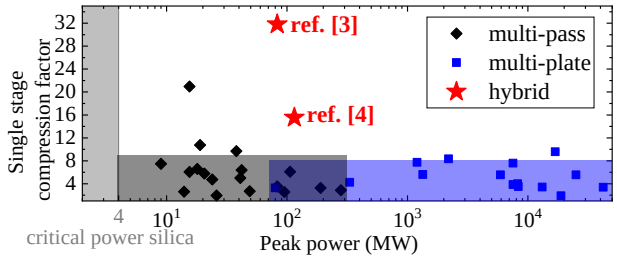

Figure 1: Reported single-stage compression factors from bulk-MPC, multi-plate continuum and our hybrid schemes. Adapted from [3].

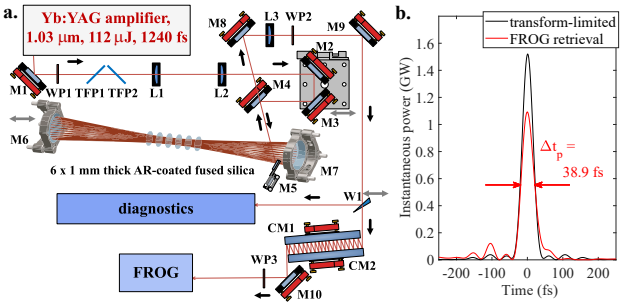

Figure 2: **a.** Hybrid pulse multi-pass multi-plate setup. **b.** Pulses compressed to sub-40 fs with GW peak power. Reprinted from [3].

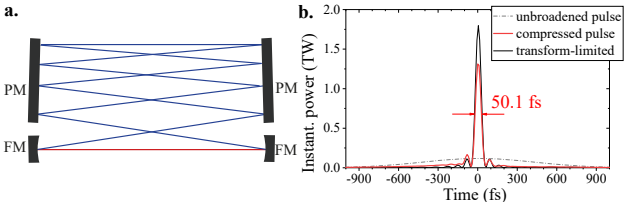

Figure 3: **a.** Bow-tie MPC consisting of a long, strongly folded collimated beam path between the plane mirrors (PM) and a shorter focusing beam path between the focusing mirrors (FM). **b.** Simulated compression of 125 mJ energy, 1 ps duration pulses to 50 fs duration and 1.3 TW peak power in an only 2 m long cell. Reprinted from [5].

In addition, we have theoretically and numerically studied the energy-scalability of the MPC approach. We have proposed the use of bow-tie MPCs to down-size high-power MPCs to usual laboratory dimensions [5]. Figure 3 shows a simulation that predicts compression of 125 mJ pulses to TW-level peak powers by spectral broadening in a bow-tie MPC with two 1 mm thin Kerr media, demonstrating attractive energy and peak-power scaling options.

We acknowledge DESY, a member of the Helmholtz Association HGF, for the provision of experimental facilities.

References

[1] A.-L. Viotti *et al.*, Optica **9**, 197 (2022).

[2] C.-H. Lu *et al.*, Optica **1**, 400 (2014).

[3] M. Seidel *et al.*, Ultrafast Science *in press* (2022).

[4] M. Seidel *et al.*, Laser Photonics Rev. **16**, 2100268 (2022).

[5] C. M. Heyl *et al.*, J. Phys. Photonics **4**, 014002 (2022).

Focal spot imaging for precision high power laser diagnostics

X. Huang*[1,2], A. Sävert[1], B. Heinemann[2], and M. Zepf[1]

[1]Helmholtz Institute Jena, Fröbelstieg 3, 07743 Jena, Germany; [2]DESY, 22607 Hamburg, Germany

The LUXE (Laser Und XFEL Experiment) project at DESY Hamburg aims to measure processes in the strong-field quantum electrodynamics regime with high precision by colliding electrons or a high-energy photon beam with high-power, tightly focused laser beam at a repetition rate of 1Hz. Simulations [1] predict that pair production probability responds highly non-linearly to the laser strength parameter. To achieve high precision measurements, it is crucial to measure laser intensity with precision of better than 1%. The laser beam must be reimaged from the interaction point to a diagnostic table 40 meters away for LUXE. Care must be taken to avoid altering the beam profile and introducing systematic errors. In this report, we compare the simulation results of two imaging setups using Zemax.

In the LUXE experiment [1], a 350 TW laser pulse is focused to intensity $> 10^{20}$ W/cm^2 and interacts with a 16.5 GeV electron bunch from the XFEL electron accelerator. After the interaction, the laser propagates to the diagnostic room which is about 40 meters away above the XFEL tunnel. To guarantee the precision of laser intensity diagnostic $< 1\%$, the focus at diagnostic table must be identical to the interaction point (IP), but as shown in Fig. 1 free propagation without imaging leads to significant changes in the beam profile.

Aiming to reconstruct an identical focus at diagnostic system, two setups are simulated as shown in Fig. 2. At plane A in Fig. 2(a), the incident beam is defined the same as in Fig. 1(a). The first off-axis parabolic mirror (OAP) with $f/3$ focuses the laser to IP. The beam is recollimated by OAP2 and transported through the 40m laser path to the diagnostic table. An identical focus IP' is obtained using the same focusing OAP.

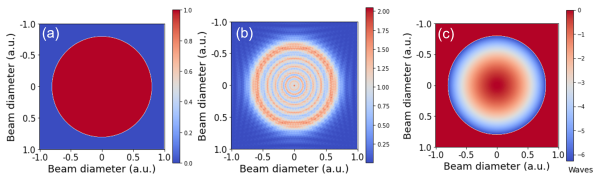

Figure 1: To show the importance of imaging the beam to the diagnostic table, simulation using Zemax shows that long-distance propagation causes significant distortion on laser profile . (a) The initial beam is defined with top-hat profile and flat wavefront with central wavelength 800 nm. After propagation in vacuum for 40m, (b) beam intensity profile distorts and (c) wavefront has peak-to-valley value 6.25λ and rms 1.8λ.

* xinhe.huang@uni-jena.de

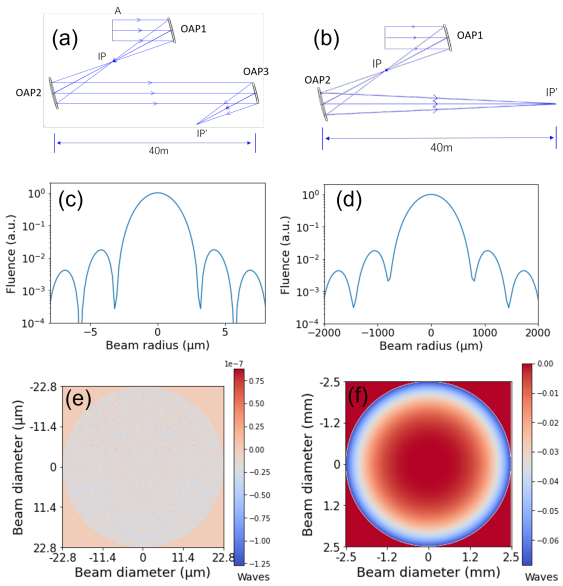

Figure 2: The setup and simulation results of imaging IP to diagnostic system. (c) is the intensity profile of the focus cross section at IP and IP' from setup (a) and (e) the wavefront. (d) and (f) are the focus intensity and wavefront of IP' in setup (b).

While in principle feasible, this approach requires very high surface precision for two imaging OAPs and all large aperture mirrors in between. Any surface irregularity of the optics introduces extra wavefront distortion and degrades the imaging performance. What's more, misalignment of incident beam causes astigmatism of IP, which is compensated by the recollimating OAP2.

An alternative system was considered in setup 2 in Fig. 2(b). The initial beam settings and OAP1 are the same as in (a). OAP2, instead of collimating the beam, shifts slightly off position and converges beam over a distance of 40m, directly imaging IP to IP'. An OAP was considered as off-axis ellipsoids are not readily available. This set-up eliminates the uncertainties associated with the second OAP and has smaller beam diameter on the subsequent optics. The wavefront aberration in (f) for setup 2 with PtV 0.07λ and rms 0.02λ is within acceptable range.

In conclusion, the imaging of the IP over 40 m is feasible using a single OAP, greatly simplifying the setup and minimizing risks. We will compare these simulation results in an experiment in the near future.

References

[1] LUXE CDR, arXiv:2102.02032 [hep-ex]

Neural Networks for HI Jena Laser Plasma Accelerators

A. Sävert*[1], G. Schäfer[1], and M. Zepf[1]

[1]Helmholtz Institute Jena, Fröbelstieg 3, 07743 Jena, Germany

The beam pointing of a high power laser is crucial for applications in high intensity experiments. Either to hit a small target the size of the laser focal spot or to reduce the pointing fluctuations in laser driven electron acceleration. A typical source for beam pointing issues are air fluctuations and strong vibrations on optical tables. Here we show that a neural network can be used to predict the position of the laser beam with good accuracy and reduce the jitter by one order of magnitude

The JETi200 laser system at the Helmholtz Institute Jena has been used in various experiments like laser and particle driven wake field acceleration, surface high harmonic generation and ion acceleration from thin foils and mass limited targets. These experiments require a high degree of control of the used laser pulses and stable shot to shot operation. JETi200 can provide compressed laser pulses up to 5 J in energy with an rms jitter of $< 0.5\%$ and a pulse duration < 20 fs with an rms jitter < 0.2 fs. The beam quality, which is optimized by a deformable mirror, allows for a nearly diffraction limited focal spot with a Strehl ratio of > 0.95. Nevertheless, the direction of the laser pulses and hence the position of the focal spot varies from shot to shot. This is caused by a number of sources, e.g. air fluctuations from the air conditioning, low frequency vibrations of the building and high frequency vibrations from vacuum or cryo pumps. The latter one is the most dominant in the JETi200 laser system. Its last power amplifier is actively cooled to mitigate thermal lensing. To reach the required temperature of -180 °C a closed cycle cryocooler is used. Its strong vibration couples to the laser beam and result in a pointing jitter of the laser focal spot of more than 20 µrad rms with a broad frequency spectrum up to 30 Hz. This is much higher than the nominal repetition rate of JETi200 and more so during single shot experiments. Thus the pointing jitter can not be directly compensated using the JETi200 pulses themselves. Using a cw pilot laser beam, which follows the same beam path through the final three amplifiers, and a fast CCD camera enables to record the pointing fluctuations in real time. Here, the centroid of the laser focal spot was used and fed into a neural network to predict the position of the laser beam ahead in time. This was done purely in software for proof-of-concept. The fully connected neural network was written in LABVIEW and uses two hidden layers with 85 and 65 neurons. The network was trained using a time series of 8 seconds (500 points, see Figure 1a) of just air fluctuations alone with the cryocooler switched off.

When the algorithm converged it was possible to predict the position of the laser beam quite well for the next 8 seconds and the rms pointing jitter was reduced from 3 µrad rms to 0.3 µrad rms, see yellow curve in Figure 1b. However, at later times, Figure 1 c, the prediction got worse until the jitter of the beam was in the same order as the unoptimized beam. In this example it could be shown that a neural network can be used to reliable predict the beam fluctuation and in principle correct for them using a fast steering mirror. Still, the training of the network took much longer (10 min) compared to the required time frame (8 s) for the prediction. This could be improved by using dedicated hardware, e.g. FPGAs, to do the calculations and control of the mirror in the required time. Finally, to correct the pointing fluctuation when the cryocooler is switched on one needs a higher acquisition rate to better sample the position of the laser focal spot.

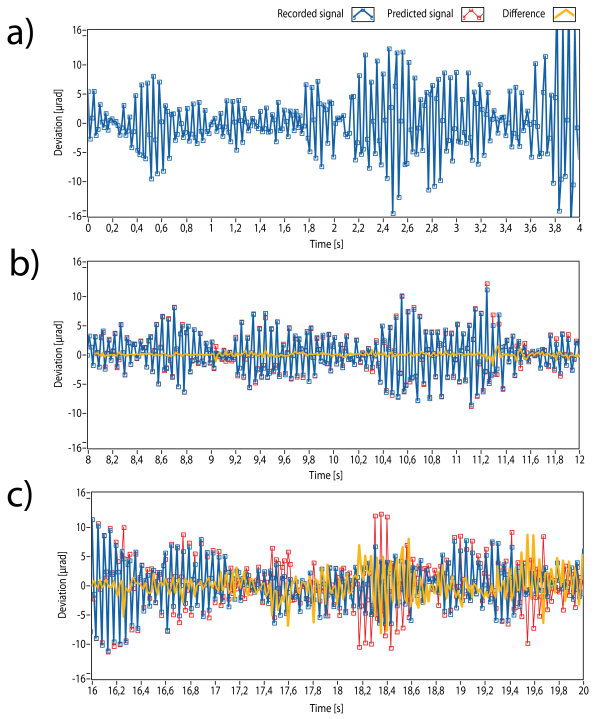

Figure 1: a): Recorded data used for teaching (blue). b): Recorded (blue) and predicted data (red), residual (yellow) results from the neutral network for the following 4 seconds. c): Long term prediction showing strong deviations.

*a.saevert@hi-jena.gsi.de

Target Area Fraunhofer: Status Update

D. Hollatz*[1], A. Sävert[1], M. Hornung[1], P. Hilz[1], M. Kaluza[1,2], and M. Zepf[1,2]

[1]HI Jena, Fröbelstieg 3, 07743 Jena, Germany; [2]IOQ, FSU Jena

Target Area Fraunhofer (TAF) is part of the new extension building at the Helmholtz-Institute Jena. It provides the opportunity to perform two beam experiments, for example proton probing of a laser wake field or pair production, with JETi200 and POLARIS, the two high-power laser systems at HI Jena. The completion of the building is planned for Summer 2022 and first hardware will be installed in late 2022. The first experiment is scheduled for early 2024. In this report, we provide a status update on the progress.

Target Area Fraunhofer provides an experimental platform for two beam experiments with JETi200 and POLARIS, for example proton probing of a laser wake field or pair production and strong field QED experiments. For many experiments, like LWFA, the f-number and thereby the focal length is an essential parameter. As lasers can be upgraded over time, the physical space in target areas is often the limiting factor. Therefore we planned TAF to be future proof at 17 metres long and 6 metres wide. A photograph of TAF in the current state can be seen on Fig. 1.

The heart of TAF is the target chamber, which is over 6 metres long and 2.5 metres wide. To accommodate large optical assemblies, the target chamber contains a monolithic 6 by 2.5 metre breadboard that is decoupled from the chamber walls. Above the breadboard, 1 metre of free space is available for the setup. A preliminary conceptual design of the target chamber is shown on Fig. 2. The scheduled delivery date is October 2022.

Figure 1: Photograph of TAF taken in March of 2022.

To enable a wide variety of experiments with JETi200 and POLARIS, we plan a dedicated beam shaping chamber containing a plasma mirror for contrast enhancement, a hollow core fibre for pulse compression and focussing optics for long focal lengths. This chamber will be installed inside TAF right before the target chamber within the coming years after first experiments. It will be 6 metres long, 2 metres wide and 2 metres high. The modular design of this beam shaping chamber will allow us to manipulate both JETi200 and POLARIS with any of the components, providing great flexibility. For first experiments in 2024, JETi200 and POLARIS will be sent into the target chamber directly.

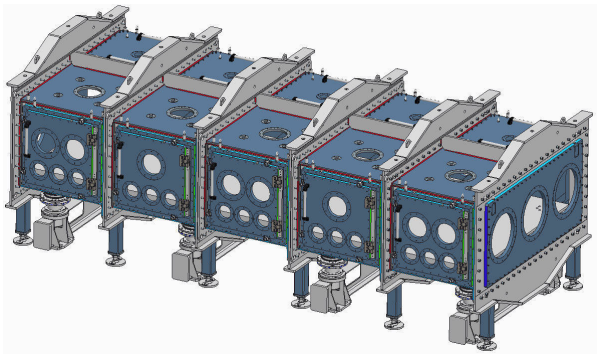

Figure 2: Conceptual design of the TAF target chamber.

To extend the variety of experiments even further, we will upgrade POLARIS by increasing the beam diameter from 140 to 190mm. This is accompanied by a completely new compressor design to handle the larger beam, which will increase POLARIS compressed pulse energy by more than a factor of two. The vacuum components for this upgrade will be installed in Winter of 2022.

Any two beam experiment in TAF will require control over the spatio temporal overlap between JETi200 and POLARIS, where the exact requirements differ from setup to setup. For proton probing or linear Breit-Wheeler pair production experiments like Ref. [1], picosecond timing is sufficient while other experiments like strong field QED experiments [2] require femtosecond accuracy. For moderate timing control above 200 fs rms, the oscillators of both lasers will be synchronised with a commercial system based on rf signals that will be available for first experiments in 2024. For high precision timing control down to 20 fs rms, a synchronisation system based on optical communication will be installed in the coming years.

Overall, the TAF project enables experiments with JETi200 and POLARIS at the Helmholtz-Institute Jena.

The authors acknowledge funding from Thüringer Aufbaubank and the Helmholtz Association.

References

[1] B. Kettle, D. Hollatz *et al.*, New J. Phys. **23**, 115006 (2021).

[2] F. C. Salgado *et al.*, New J. Phys. **23**, 105002 (2021).

*dominik.hollatz@uni-jena.de

Table-top interferometry on extreme time and wavelength scales

S. Skruszewicz[1], A. Przystawik[1], D. Schwickert[1], M. Sumfleth[1], M. Namboodiri[1], V. Hilbert[2], R. Klas*[2,3], P. Gierschke[2,4], V. Schuster[2], A. Vorobiov[5], C. Haunhorst[5], D. Kip[5], J. Limpert[2,3,4], J. Rothhardt[2,3,4], and T. Laarmann[1,6]

[1]Deutsches Elektronen-Synchrotron DESY; [2]Institute of Applied Physics, Friedrich-Schiller-University Jena; [3]Helmholtz Institute Jena; [4]Fraunhofer Institute for Applied Optics and Precision Engineering; [5]Faculty of Electrical Engineering, Helmut Schmidt University Hamburg; [6]The Hamburg Centre for Ultrafast Imaging CUI

Dynamic studies in the extreme ultraviolet (XUV) benefit from interferometric studies. In this contribution, the implementation of a Michelson-type all-reflective split-and-delay field autocorrelator (SD-AC) in combination with a table-top, high harmonic generation (HHG) based XUV source is demonstrated. The compact setup can achieve a scan length of 1 ps, corresponding to an energy resolution of E/ΔE = 2000. This opens new opportunities for soft x-ray dynamic studies on atomic time (attosecond)-scales.

Interferometry in the XUV plays a key role for attosecond metrology and applications. Its capability lies in the control of the relative phases of the two interfering beams and enables to track the propagation of quantum objects on atomic length (nanometer) and time scales (attosecond).

Many of the key requirements of an interferometer are challenging to meet in the XUV. The SD-AC used herein is an excellent device for this task [1]. It allows to split the field amplitude of the incoming beam, delay the two replicas and superpose them in a single optical element.

This common path interferometer consists of two interleaved lamellar mirrors under gracing incidence. It enables to split the XUV wavefront uniformly across the beam profile and to generate two collinearly propagating pulse replicas with a plane wave front, allowing for tight focusing while keeping a high fringe contrast. Furthermore, the grazing incidence angle results in a high transmission over a wide spectral coverage (10 nm to 1 μm).

The capability of this device has been already demonstrated in previous experiments at large scale facilities [1]. In this contribution, the combination of the SD-AC with a table-top XUV source is demonstrated [2]. For this, an HHG source, similar to the one presented in [3], is used.

*robert.klas@uni-jena.de

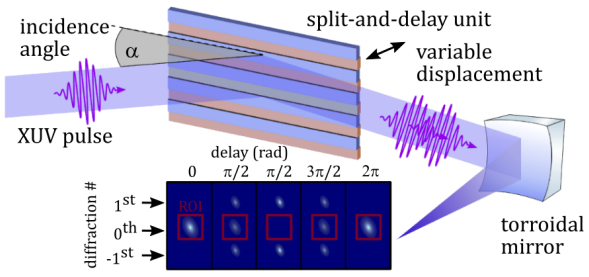

Figure 1: Illustration of the XUV Fourier-transform spectroscopy experimental setup, using a SD-AC [2].

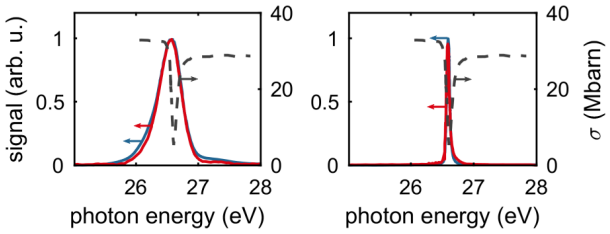

Figure 2: Spectra of HH11 at 26.5 eV measured with flat field grating based XUV spectrometer (blue) and retrieved from the FT measurement (red). The original spectral shape is shown in a) and the spectrum after propagating through 1 m of $8 \cdot 10^{-2}$ mbar of Ar is shown in b) [2].

At a repetition rate of 1 kHz and a wavelength of 47 nm (26.5 eV), it delivers an average power of up to 1 mW at a pulse duration of sub-6 fs. Upon reflection from the lamellar-mirror assembly, the XUV pulses are focused with a torroidal mirror onto a Ce:YAG scintillator. In order to obtain the AC trace of the XUV beam, the spatially integrated signal of the 0^{th} diffraction order is measured for each delay. Fourier transforming (FT) the measured AC results in the spectrum, which is cross checked with a flat field grating spectrometer.

The line width and shape can be manipulated by exploiting a window-type Fano resonance in argon [4]. For this, the XUV beam is propagated trough an argon flooded chamber. Two exemplary lines are shown in Fig. 2, demonstrating an excellent agreement of the two methods.

This demonstration paves the way for table-top XUV-pump XUV-probe experiments in the near future [5], which pushes spectroscopic studies in time and frequency domain to the ultimate limit given by the uncertainty principle. Hence, this technique opens new opportunities for soft X-ray pulse metrology, dynamic studies and nonlinear spectroscopy in matter, materials and life sciences.

This work was supported by CAPS, ECRAPS, EXC 2056 (390715994), SFB 925 (176020586), KI 482/20, LA 1431/5-1 and APPA R&D (13N12082).

References

[1] S. Usenko *et al.*, Appl. Sci. **7**, 544 (2017) .

[2] S. Skruszewicz *et al.*, Opt. Express **29**, 40333 (2021).

[3] R. Klas *et al.*, PhotoniX **2**, 4 (2021).

[4] S. L. Sorensen *et al.*, Phys. Rev. A **50**, 1218 (1994).

[5] J. Rothhardt *et al.*, X-Ray Spectrom. **49**, 165 (2020).

Towards attosecond imaging at the nanoscale using broadband holography-assisted coherent imaging in the extreme ultraviolet

S. Wang*[1,2], W. Eschen[1,2], C. Liu[1,2], M. Steinert[2], T. Pertsch[3,3], J. Limpert[1,2,3], and J. Rothhardt[1,2,3]

[1]HI Jena, Fröbelstieg 3, 07743 Jena, Germany; [2]FSU Jena, Albert-Einstein-Str. 15, 07745 Jena, Germany; [3]Fraunhofer IOF, Albert-Einstein-Str. 7, 07745 Jena, Germany

We present a broadband holography-enhanced imaging approach, which enables the combination of high-resolution coherent imaging with a large spectral bandwidth. By implementing the method in the extreme ultraviolet, we demonstrate a spatial resolution of 34 nm in combination with a large spectral bandwidth supporting attosecond pulses.

'Lensless' coherent diffraction imaging techniques can provide very high spatial resolution on the nanoscale. Fourier transform holography (FTH) is a particularly robust lensless imaging method, which directly encodes the phase of the object's exit wave in the far-field interference pattern by means of an adequately placed reference pinhole [1]. Then both amplitude and phase images can be extracted from the cross-correlation of the reference wave with the object's exit wave by a simple Fourier transform with a resolution in the order of the reference pinhole size.

For ultrafast studies, e.g. on electron- or spin-dynamics, a combination of the high spatial resolution of lensless imaging techniques with the high temporal resolution provided by attosecond pulses is desired. Unfortunately, the broad bandwidth of attosecond pulses conflicts with the temporal coherence requirement of lensless imaging. A broad spectrum generally reduces the contrast of the spatial diffraction pattern particularly at large diffraction angles and reduces the spatial resolution. In FTH, this results in an anisotropic smearing effect spoiling the image quality mostly along the axis from the object pointing to the reference pinhole. The blurred reconstruction is shown in Fig. 1a, in which the vertical smearing effect is way stronger than the horizontal direction since the pinhole is placed above the Siemens-star.

To solve the dilemma, we put forward a new method for broadband FTH. We place several pinholes around the object of interest and combine the high contrast parts of all resulting cross-correlations with direction-selective Fourier filters. This way, the nicely resolved (non-smeared) object features are selected and can be combined in the Fourier domain, generating an image with superior resolution and quality (see Fig. 1b) by applying a simple Fourier transform again.

We demonstrate our method in a proof-of-principle experiment. For this purpose we select a bandwidth of 5.5 eV centered at 92 eV (13.5 nm) from a broad XUV continuum which was generated via high harmonic generation [2]. The Siemens star-like sample with five surrounding pinholes was placed in the focus of the XUV beam. We implemented high-resolution imaging ($\approx$ 65 nm) which has been improved a lot from the lineout in Fig. 1d, compared with the resolution limit (110 nm) imposed by the broad bandwidth, supporting a theoretical Fourier-limited pulse duration of only 380 as [3]. In addition, the FTH-result can be seeded as the primary guess into a broadband iterative phase retrieval algorithm, which converges fast and refines the reconstruction, achieving a spatial resolution of 34 nm (2.5 λ) (see Fig. 1c).The presented method allows using much larger spectral bandwidth for imaging. As a result, shorter pulses are supported and ultimately temporal resolution could be added to enable nanoscale imaging of ultrafast dynamics with (sub)-fs XUV pulses after excitation with synchronized IR to UV pulses. A detection with simultaneous high temporal and spatial resolutions can be expected by applying the presented method in combination with pump-probe techniques.

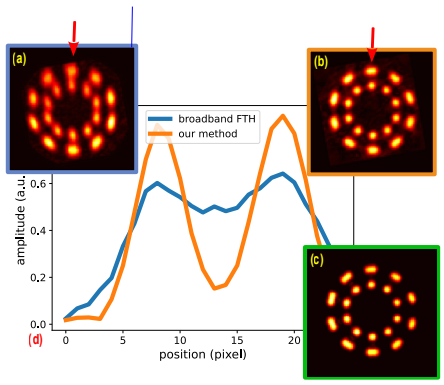

Figure 1: Reconstructions contrast before and after using our method. (a): Traditional broadband FTH. (b): Applying our improved method. (c): Further refinement of iterative phase retrieval algorithm.

This work was supported by the ESF, TAB-FGR 0076, ERC SALT, FhG CAPS and the Helmholtz Initiative and Networking Fund.

References

[1] I. McNulty *et al.*, Science **256**, 1009 (1992).

[2] R. Klas *et al.*, Optics Express **28**, 6188 (2020).

[3] W. Eschen *et al.*, Communications Physics **4**, 1 (2021).

*sici.wang@uni-jena.de

LASER PARTICLE ACCELERATION

Interplay of Ionization and Target Expansion in Laser–NanoFoil Target Interaction

Y. Azamoum*[1,2], G. A. Becker[1], S. Keppler[1,2], S. Skupin[3], G. Duchateau[4], F. Catoire[4], I. Tamer[1,2], M. Hornung[1,2], A. Kessler[1, 2], M. Hellwing[1], F. Schorcht[2], and M. C. Kaluza[1,2]

[1]Institute of Optics and Quantum Electronics, Jena Germany; [2]Helmholtz Institute Jena, Germany; [3]Institut Lumière Matière, Université Lyon 1 - CNRS, Villeurbanne, France; [4]Université de Bordeaux-CNRS-CEA, CELIA, France.

We investigate the interplay between ionization and target expansion during the interaction of intense laser pulses ($I < 10^{16}$ W/cm^2) with 5 nm thick Diamond Like Carbon (DLC) foil. Numerical calculations show that the almost totally blocked probe light through the produced plasma cannot be explained by the fully ionized target. We explore the possible expansion of the target during the interaction which may play a role to induce the very low transmission ($\lesssim 10^{-2}$) of the probe.

Relativistic laser-thin foil interactions can produce highly energetic ion beams. In this scheme, controlling the features of the pre-plasma produced by the rising edge of the laser pulse on the target is a key factor to enhance the particle beam's quality. For high power lasers, a single shot time-resolved probing diagnostic is required to overcome the shot-to-shot fluctuations. In [1] we successfully measured the spatio-temporal plasma dynamics using a single probe illumination. Furthermore, using the measured temporal intensity contrast of the laser pulse as an input parameter in our two-step numerical calculations, we reproduced the measured time constant characterizing the ionization dynamics for different materials [2]. First, the time-dependent electron density is retrieved using the ionization model. Then, the Drude model is applied together with a Maxwell solver for a plane wave to calculate the probe transmission through the plasma. In this work, we propose a reverse approach which aims to retrieve numerically the required electron density from the measured time-dependent transmission of the probe for the 5 nm thick DLC foil. First, the transmission of the probe through a 5 nm plasma slab characterized by its electron density n_e, is calculated. The result is depicted in Figure 1.

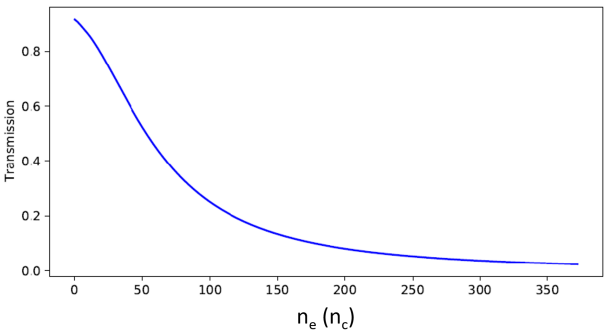

Figure 1: Calculated Transmission for the plasma electron density n_e expressed in in critical density n_c units, up to full ionization value for the DLC target, assuming that no target expansion occurs.

* yasmina.azamoum@uni-jena.de

n_e ranges from 0 (pristine target) to the fully ionized state of the DLC n_{emax} = 375 n_c, n_c is the critical density which corresponds to the probe wavelength λ = 800 nm. The calculation assumes no expansion of the plasma. In addition, the corresponding plasma optical properties for each n_e are calculated using a Drude Model with a collision time τ = 2 fs. The transmission is then calculated using a Maxwell solver for the probe propagation through the plasma. In Figure 2, the measured time-dependent transmission of the probe for a pulse intensity I $\sim 10^{15}$ W/cm^2, together with the required electron density based on the results of Figure 1 are shown.

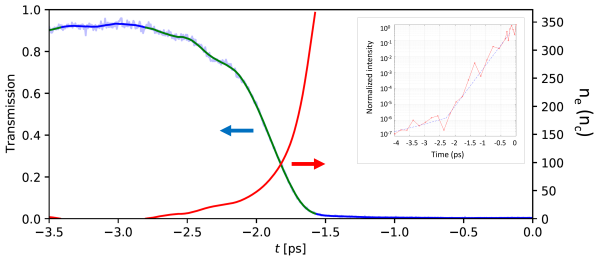

Figure 2: The measured transmission of the probe for 5 nm thick DLC target and for a pulse intensity I $\sim 10^{15}$ W/cm^2 in blue/green line. The corresponding required plasma electron density n_e (red line) deduced from Figure 1. The inset is the measured pulse temporal intensity contrast.

Figure 2 shows that the low transmission ($\lesssim 10^{-2}$) of the probe requires a plasma density that exceeds n_{emax} corresponding to the fully ionized target which is not possible. However, the model assumes that no expansion of the target occurs. This result indicates that the target expansion may play a role. In the future, to elucidate the target behavior during the interaction, we will first describe the transition from solid state to a melted target or a "cold" plasma state using the ionization model and a two-temperature model to retrieve the electron density and temperature. Finally, we will employ a Particle In Cell (PIC) code using these results as input parameters to retrieve the kinetic description of the plasma during the interaction and investigate its possible expansion. This original calculation strategy is expected to bring an unprecedented detailed insight into the target behavior during the interaction, which may help to identify the key parameters to reach high quality particle beams in laser-based accelerators.

References

[1] Y. Azamoum *et al.*, HI Jena Annual Report 2019, p. 35.

[2] Y. Azamoum *et al.*, HI Jena Annual Report 2020, p. 34.

Characterization of droplet targets and investigation of plasma expansion

G. A. Becker*[1], M. Nolte[1], T. Weickhardt[1], M. Beyer[1], D. Klöpfel[2], M. Hellwing[1], F. Schorcht[2], and M. C. Kaluza[1,2]

[1]Institut für Optik und Quantenelektronik, Friedrich-Schiller-Universität Jena, Germany; [2]Helmholtz-Institut Jena, Fröbelstieg 3, 07743 Jena, Germany

Micro-droplets are a promising target for laser-driven proton acceleration due to their limited volume and their availability at a high repetition rate. To characterize a micro-droplet source for an upcoming experimental campaign at the POLARIS laser system, a test chamber in a separate laboratory was constructed. The laboratory is equipped with a chirped pulse amplification laser system (CPA) to investigate the generation of a (pre-)plasma. Such studies are essential since the characteristics of a pre-plasma are crucial for the coupling of laser energy into the plasma and consequently for the strength of the electric field that accelerates ions.

Laser-driven ion acceleration has seen a lot of research during the last two decades. The dominant ion acceleration mechanism is the so-called Target Normal Sheath Acceleration mechanism. A high-intensity laser ($I_\mathrm{L} > 10^{18}\,\mathrm{W/cm^2}$) is usually focused onto a foil with a thickness between a few nanometers and micrometers. The rising edge of the laser pulse on a picosecond time-scale, or artificial pre-pulses, ionize the foil's front side, and a pre-plasma is generated. When the pulse peak arrives, it transfers its energy to the electrons. These electrons form a negatively charged cloud in the vacuum close to the foil's rear (and front) surface. Consequently, a quasi-static electric field between the negative space charge and the positively charged foil arises that accelerates ions and, in particular, protons to kinetic energies of several Megaelectronvolts. For applications that require a high repetition rate of proton pulses ($\gg 1\,\mathrm{Hz}$), foil targets are not suitable since they have to be replaced after every laser shot with micrometer accuracy. Additionally, the lateral extension of a foil allows electrons to escape the interaction region, which reduces the accelerating electric field. Targets with a limited spatial extension that can be generated in the interaction region with a very high repetition rate are micro-droplets. Such water droplets with a diameter of $20\,\mu\mathrm{m}$ generated by a commercial nozzle (Micro Jet Components) were successfully used in an experiment at the JETI 40 laser system. In that experiment, the second harmonic of the main pulse was used to accelerate ions, and with the broadband optical probe, the laser-plasma interaction was observed [1]. With the help of a controlled pre-pulse, the significant effect of an artificial pre-plasma on proton acceleration and plasma expansion was observed. Due to the limited laser pulse energy of the 2ω laser pulses, the maximum proton energies were only slightly above $3\,\mathrm{MeV}$ in that experiment. Consequently, a follow-up experiment with high-energy laser pulses delivered by the POLARIS laser system at the Helmholtz-Institute Jena [2] is planned. To test and characterize nozzles before the actual experiment, a test chamber was built that is situated in a separated laboratory equipped with a laser system delivering laser pulses at a repetition rate of $1\,\mathrm{Hz}$ with an energy between $2\,\mathrm{mJ}$ and $3\,\mathrm{mJ}$, and a pulse duration of about $100\,\mathrm{fs}$ [3]. A photo of the test chamber is shown in Fig. 1. The laser pulse is split by a beam splitter (90:10) before entering the target chamber. The higher energy pulse (pump) is focused by an off-axis parabola (here $f = 50.8\,\mathrm{mm}$) onto the droplets to generate a plasma that can be back-lighted by the pulse with low energy (probe). With a delay-stage in the probe's beam path outside the vacuum chamber, the time of the probe beam's arrival at the plasma's location can be changed with respect to the pump laser. Thus, the plasma's evolution as a function of time can be investigated. Fig. 2 shows an exemplary image of an expanded droplet captured $100\,\mathrm{ps}$ after the $\approx 20\,\mu\mathrm{m}$ diameter droplet was irradiated by the pump with an intensity of $10^{16}\,\mathrm{W/cm^2}$. For an optimal coupling of laser energy to electrons it is necessary to find the optimal extent and density of the pre-plasma, which is coupled, e.g., to the delay of the pre-pulse.

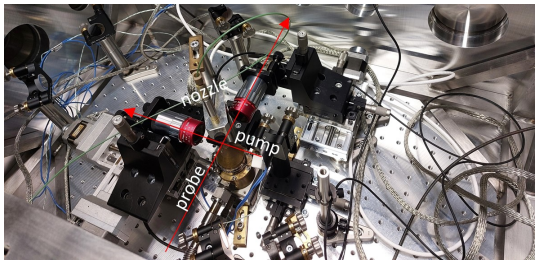

Figure 1: Top view of the test setup.

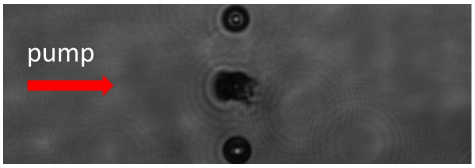

Figure 2: Part of a droplet chain. Image was taken $100\,\mathrm{ps}$ after the central droplet was irradiated by a laser pulse with an intensity of $10^{16}\,\mathrm{W/cm^2}$

References

[1] G. A. Becker *et al.*, Sci. Rep. **9**, 17169 (2019).

[2] M. Hornung *et al.*, Opt. Lett. **41**, 5413 (2016).

[3] S. Keppler *et al.*, HI Jena Annual Report, 36 (2019).

*georg.becker@uni-jena.de

Development of Plasma Probing Diagnostics for Relativistic Laser Microdroplets Interaction

M. Beyer*[1], Y. Azamoum[1,2], T. Weickhardt[1], M. Hellwing[1], M. B. Schwab[1,2], and M.C. Kaluza[1,2]

[1]Institute of Optics and Quantum Electronics Jena, Germany; [2]Helmholtz Institute Jena, Germany

We explore the possibilities of developing a time-resolved single-shot probing diagnostic for relativistic laser interactions with water droplets. The temporally stretched broadband probe pulse is used to record information on the spatio-temporal evolution of the plasma during the interaction. For the standard pump-probe configuration, we describe a different scheme to generate high energy wavelength-shifted probe pulses using self-phase modulation.

The first approach [1] utilizes a non-collinear optical parametric amplifier (NOPA) with µJ-level probe energy and broad bandwidth. The NOPA is pumped by a 2 mJ, 120 fs Yb^{3+}-based CPA system [1], and seeded with the second harmonic of the same system. An optimized cross angle and delay between pump and white light supercontinuum generates NOPA pulses. The signal's group delay dispersion (GDD) is precompensated using a chirped mirror pair to produce a nearly Fourier transform limited pulse at the output. The NOPA setup generates 12.7 µJ pulses with a spectral range from 750 to 950 nm (c. f. figure 1).

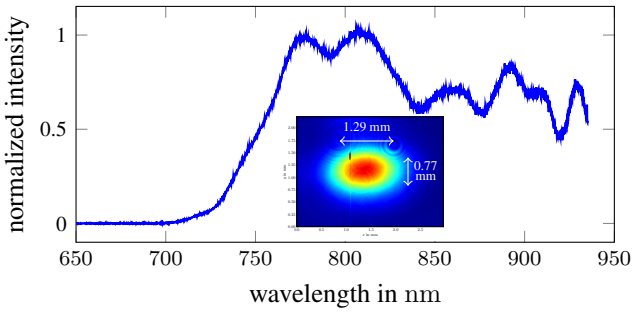

Figure 1: Spectrum of the measured NOPA beam. Inset: Spatial beam profile (dimensions at FWHM).

The second scheme [2] utilizes a simple, low-cost method of self-phase modulation (SPM) in post-CPA pulses to increase their spectral bandwidth and uses a chirped mirror pair for dispersion control. We can employ thin plastics (1 mm) with high nonlinear refractive index n_2 like allyl diglycol carbonate (CR39), which has $n_2 = 6.24 \times 10^{-7}\,\mathrm{cm^2\,GW^{-1}}$ [2] to generate strong SPM. CR39 was chosen because in addition to its high nonlinearity, the absorption across the laser pulse's spectrum should be low, particularly for the high fluences of high peak-power pulses. For the experimental setup we used the laser pulses generated from the CPA system of the supporting facility in the Abbeanum and directed them into the measurement setup depicted in Figure 2.

*m.beyer@uni-jena.de

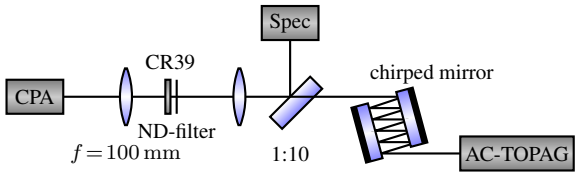

Figure 2: Schematics of the pulse compression setup. The pulse is spectrally broadened by the thin nonlinear plastic and then compressed by a chirped mirror pair.

The setup consists of a 1:1 Keplerian telescope with 100 mm focal length. A 10 % beam splitter sends part of the pulse to a VIS-NIR spectrometer (Ocean Optics Flame-S) and transmits the remaining part to a chirped mirror pair and finally to a TOPAG ASF-15 single shot autocorrelator. Without the plastic sample, the 2 mJ, 130 fs (FWHM) laser pulse was already sufficient to produce SPM in air. We inserted the 1.1 mm nonlinear CR39 plastic at its Brewster angle into the telescope at a position near the focal plane with a neutral density filter placed directly after the sample to prevent ionization of the air. The resulting spectra are shown in Figure 3.

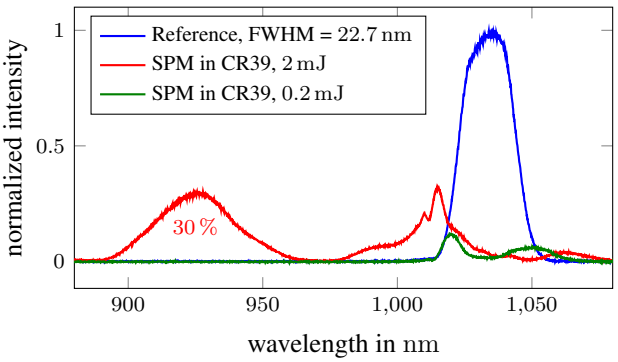

Figure 3: Spectrum of SPM (red) and reference at 2 mJ. For the green curve an ND = 1 filter was placed in front of the telescope.

We successfully generated spectral intensity far away from the central wavelength in the range of 900 nm to 950 nm with an estimated 30 % of the original pulse energy, which can be cut out and used for the probing application. The loss of energy is not prohibitive, since the initial pulse energy was magnitudes above the energy needed for the probing experiments.

References

[1] I. Tamer *et al.*, Opt. Express **28**, 19034 (2020).

[2] I. Tamer *et al.*, Opt. Lett. **45**, 6575 (2020).

Volumetric Laser-Ion-Acceleration in Target Area 2

P. Hilz*[1], J. Gebhard[2], F. Balling[2], A. Sävert[1], M. Speicher[2], J. Kalis[2], J. Schreiber[2], and M. Zepf[1]

[1]HI Jena, Fröbelstieg 3, 07743 Jena, Germany; [2]Ludwig Maximilians Universität München, Am Coulombwall 1, 85728 Garching, Germany

We report on the first ion acceleration experiment in the newly installed JeTi 200 Target Area 2 which is optimised for high intensity, short focal length experiments. The experiment used a Paul-trap to position a micrometer sized targets into the focus of the JeTi200 laser. A dedicated pre-pulse allowed the target-size and density to be controlled by pre-expansion prior to the main pulse.

The interaction of a relativistically intense light field ($I > 10^{18}\,\mathrm{W/cm^2}$) with a target, is mainly defined by the size and the density of the target. Targets with an electron density smaller than the critical plasma electron density n_c are transparent for the light, overcritical targets are opaque. Laser ion acceleration typically uses solid state targets such as thin foils with densities ranging from $100\,n_c$ to $400\,n_c$. Targets with small spatial extent and densities close to n_c represent an interesting parameter space. Unfortunately this parameter space represents a technological challenge since it can not easily be addressed via standard techniques, such as gas-jets or solid state targets.

In this experiment we used levitated spherical polystyrene targets with an diameter of $d \approx 1$ µm. We used an electrodynamic trap to position those targets[1]. This target system was already used on petawatt class lasers such as the Phelix laser in Darmstadt [2] and the Texas petawatt laser [3]. In [2] it was found that the pre-expansion in the rising edge of the $500\,\mathrm{fs}$ long laser pulse is crucial for the acceleration dynamics.

It is the first time that this target system is used on a 30fs-class laser. A dedicated pre-pulse with $I \approx 10^{16}\,\mathrm{W/cm^2}$ was installed to mimic the pre-expansion encountered in [2]. The pre-pulse allowed us to pre-expand the target. Due to the three dimensional nature of the expansion the target can significantly alter its density.

Two spectra are shown in fig 1. The upper spectrum shows the proton and carbon spectra without a pre-pulse. The lower spectrum shows the spectra with a pre-pulse. Via inline holography (also backed up by 3D PIC simulations) the peak density of the pre-expanded sphere was estimated to $n_e \approx 10\,n_c$.

The spectra extend up to $20\,\mathrm{MeV}$. To our knowledge this represents an efficiency record of $20 - 40\,\mathrm{MeV/J}$. It is also clearly visible that the maximum ion energy increases slightly in the pre-expanded case. Also the number of accelerated ions increases.

Since the total number of particles taking place in the interaction is well know it can be inferred from the spectra that the acceleration must be volumentric and directed into the forward direction.

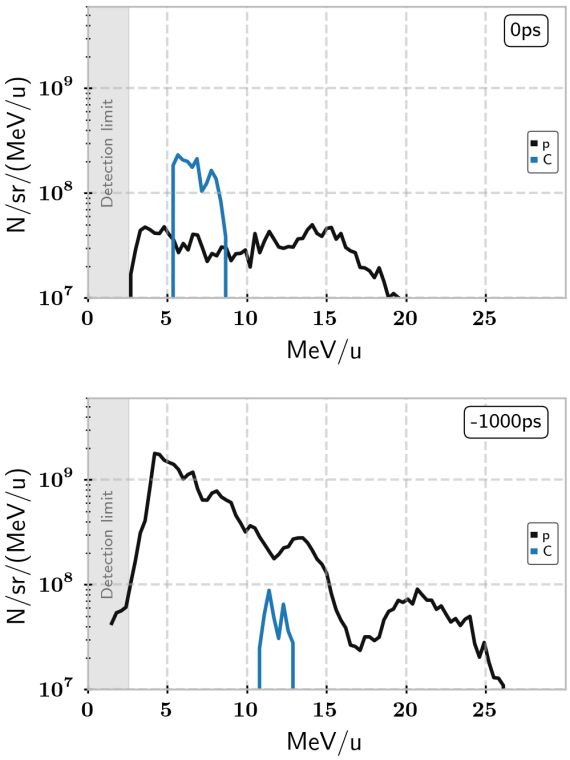

Figure 1: Obtained ion spectra without and with pre-pulse.

3D PIC simulations indicate a two staged acceleration process for the pre-expanded sphere. In a first stage the target is volumetrically accelerated followed by an directed coulomb explosion. It is interesting to note that the efficiency of the first stage is in the order of $20\,\mathrm{MeV/J}$. This is ten times more than the previous result using longer pulses $2\,\mathrm{MeV/J}$ found in [2]. In conclusion, out preliminary analysis shows volumetric acceleration to be a highly efficient approach to laser-ion acceleration.

References

[1] T. M. Ostermayr *et al.*., Rev. Sci. Instr. **89**, 013302 (2018).

[2] P. Hilz *et al.*., Nat. Commun. **9**, 423 (2018).

[3] T. M. Ostermayr *et al.*., Phys. Rev. E **94**, 033208 (2016).

*p.hilz@gsi.de

Analytical description of laser-driven holeboring into an arbitrary plasma density profile

J. Hornung*[1,2,3], Y. Zobus[4], S. Roeder[1,4], A. Kleinschmidt[1], D. Bertini[1], M. Zepf[2,3], and V. Bagnoud[1]

[1]GSI Helmholtzzentrum für Schwerionenforschung GmbH, Planckstraße 1, 64291 Darmstadt, Germany; [2]Helmholtz-Institut Jena, Fröbelstieg 3, 07743 Jena, Germany; [3]Friedrich-Schiller-Universität Jena, Fürstengraben 1, 07743 Jena, Germany; [4]Technische Universität Darmstadt, Karolinenplatz 5, 64289 Darmstadt, Germany

The measurement of the reflected light in laser-plasma-interaction experiments shows promising possibilities to be used as a preplasma diagnostic tool, as its properties are modified by the interaction. However, in order to utilize such a measurement, a sufficient description of the holeboring process is necessary, especially in the presence of a non-uniform density distribution. Therefore, we developed an analytical description of holeboring into an arbitrary density profile, which correlates its velocity to the scale length of the plasma, picoseconds prior to the laser peak intensity.

In laser-driven ion acceleration experiments, the properties of the dense plasma developing during the last instant prior to the arrival of the peak laser irradiation is critical for the outcome of the acceleration process. During such an interaction, the spectral properties of the reflected laser pulse, which is modulated by Doppler-broadening due to the laser-holeboring process, can be used to get insights into the interaction process itself [1]. We therefore developed an analytical model which describes the temporal evolution of holeboring, using realistic plasma-density and laser-intensity profiles. This extends the standard equation for the holeboring velocity, by Kruer, et al. [2], by considering a temporally varying electron density $n_e(t)$. The corresponding profile can be described by the so-called plasma density scale length $L_c = n_c/\nabla n_c$, with a given gradient ∇n_c at the critical density n_c. Using the assumption of a constant scale length behind the interaction point results in a novel description of the holeboring velocity $v(t)$ which is strongly influenced by the scale length of the plasma [3]:

$$v(t) = \frac{2L_c\sqrt{I(t)}}{\int_{-\infty}^{t}\sqrt{I(\tau)}d\tau + 2L_c\sqrt{\frac{cn_cM_i}{Z\cos(\theta)}}}. \qquad (1)$$

Here, c describes the speed of light, M_i and Z the mass and charge state of the ions and θ the incidence angle between laser and target. Equation (1) shows that the holeboring velocity reduces in the presence of a shorter scale length. Increasing the scale length towards infinity results in the well known equation for the holeboring velocity for a constant electron density [2]. The influence of the scale length also changes the holeboring acceleration, e.g. the temporal derivative of the holeboring velocity, which can be extracted from the reflected light during the interaction and can therefore be used as an observable in experiments.

* j.hornung@gsi.de

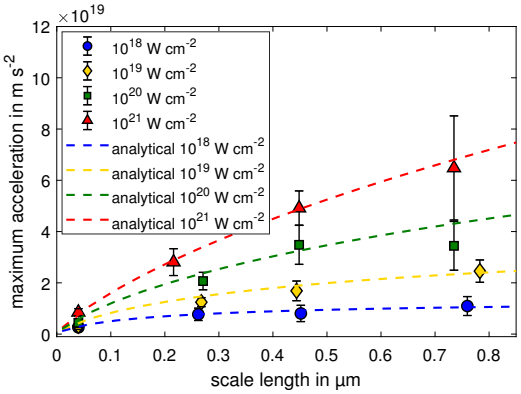

Figure 1: Maximum acceleration of the critical density surface taken from 2-D Particle-In-Cell simulations and the presented analytical description of the holeboring velocity for different density scale length and laser intensities [3].

This behavior and therefore the analytical description has been confirmed by performing 2-D Particle-In-Cell (PIC) simulations and extracting the holeboring acceleration. The results are visible in Fig. 1, showing the maximum acceleration of the critical density surface for different initial plasma scale lengths and various laser intensities, from $10^{18}\,\mathrm{W\,cm^{-2}}$ to $10^{21}\,\mathrm{W\,cm^{-2}}$. The calculated maximum acceleration for the same laser and plasma parameters is visible by the dashed lines for the respective laser intensity, which shows a very good agreement with the simulations.

Comparing measurements of the spectral shift, introduced by the moving reflective surface, with the analytical spectral shift additionally enables the possibility to indirectly measure the gradient of the plasma in experimental conditions [3]. This would ease the measurement of short scale lengths in the sub-micrometer regime, which is required for many advanced laser-ion acceleration schemes.

This work was carried out within the framework of the EUROfusion Consortium and received funding from the Euratom Research and Training Programme 2014-2018 and 2019-2020 under Grant Agreement No. 633053. The views and opinions expressed herein do not necessarily reflect those of the European Commission.

References

[1] M. Zepf *et al.*, Phys. Plasmas **3**, 3242 (1996).

[2] W. Kruer *et al.*, Phys. Rev. Lett. **35**, 1076 (1975).

[3] J. Hornung *et al.*, Nat Commun **12**, 6999 (2021).

Nanosecond Living Hot and Dense Plasma and High Energy Particles from Relativistic Laser-Nanowire Interaction

E. Eftekhari-Zadeh*[1,4], M. Gyrdymov[2], P. Tavana[1,2], R. Loetzsch[1,4], I. Uschmann[1,4], T. Siefke[3], T. Käsebier[3], U. Zeitner[3,5], A. Szeghalmi[3,5], O. Rosmej[2], D. Kartashov[1], and C. Spielmann[1,4]

[1]IOQ, FSU Jena; [2]IAP, GU Frankfurt am Main; [3]IAP, FSU Jena; [4]HI Jena, Fröbelstieg 3, 07743 Jena, Germany; [5]Fraunhofer IOF, Albert-Einstein-Str. 7, 07745 Jena, Germany

Structuring the target surface at micro and nanoscale significantly improves the laser energy deposition into the target volume resulting in remarkable enhancement of the flux and energy of generated particles and also yield of X-rays [1, 2]. We report strong enhancement in energy and flux of protons and existence of kiloelectron-volt temperature, high-density plasma with nanosecond scale lifetime from composite nanowire arrays, irradiated by ultrahigh temporal contrast, relativistically intense laser pulses.

The experiments were conducted at the JETI 40 laser system delivering 0.7 J, 30 fs, 0.8 μm, 10 Hz laser pulses. To ensure high temporal contrast, the laser pulses were frequency doubled to 400 nm resulted in a temporal contrast $\leq 10^{-12}$. The second harmonic beam was focused normally on the target reaching intensities $\geq 3 \times 10^{19}\mathrm{W/cm^2}$ ($a_0 \approx 2$). Two crystal spectrometers equipped with X-ray CCD cameras as detectors were used for high resolution measurements of X-ray line emission from Si and Ti ions. We also employed particle diagnostics consisting of electron and ion magnet spectrometers with image plates as detectors, located at the front and at the rear sides of the targets. The targets consist of low-Z (Si), 100 nm diameter, core NWs that were etched into a 50 μm thick Si membrane and subsequently coated by a 25 nm thick layer of TiO_2 (high-Z cladding) using the atomic layer deposition technique. The fabricated NWs are ≥ 5 μm long, and have 400 nm regular spacing and an overall diameter of 150 nm (44% of solid density) (Fig. 1a). As reference targets we employed a 50 μm thick Si substrate coated with 25 nm Ti layer.

The measured proton spectra ejected from the front side of the NWs show 3× increase in the effective proton temperature and also $>$ 3x increase in cut-off energy as compared with protons generated from the reference target (Fig. 1b). Cut-off energy of high energetic protons from NWs exceeds 5 MeV and was out of the detection range of our spectrometers (inset in Fig. 1(b)). Meanwhile, measured electron spectra at the front and rear sides of the targets demonstrate almost equal effective hot electron temperature for both flat and NWs. However, the total number of electrons with energies in the range of 0.4-8 MeV which were accelerated from NWs is by a factor of 4 higher than from the reference target.

The spectral analysis of K-shell X-ray emission lines revealed stronger (>4×) emission from Si^{12+} and Si^{13+} ionic states of Si from NWs compared to the reference target.

*e.eftekharizadeh@uni-jena.de

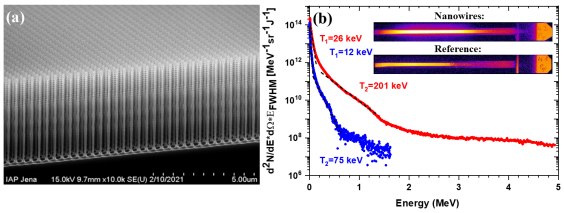

Figure 1: Side view SEM images of NWs (a), measured proton spectra (c) for nanowires (solid red line) and for reference target (solid blue line). In-sets: raw IP images of proton spectra for the reference and NWs.

Also, the X-ray emission from He-like ionic state (Ti^{20+}) ions show more than an order of magnitude increase for the NWs compared to the reference target (Fig. 2). The emission of He-like Ti^{20+} X-ray originates from a thin layer near the target surface for the reference target (Fig. 2a), whereas for the NW arrays the emitting volume is spatially extended up to 1 mm from the target surface (Fig. 2b). Considering extremely high radiative decay rate of excited states in He-like Ti ions ($2.4 \times 10^{14}\,\mathrm{s^{-1}}$) responsible for the observed emission lines, and 4.7 keV transition energy, Fig. 2b suggests existence of relatively dense, keV temperature plasma long after the interaction with the laser pulse. Namely, estimating the speed of hydrodynamic expansion of this plasma, the 1 mm spatial extension corresponds to several ns' life time. We assume that hot and relatively dense plasma living at ns time scale is the result of strong magnetic fields generated in the process of plasma evolution after the laser pulse interaction with NWs.

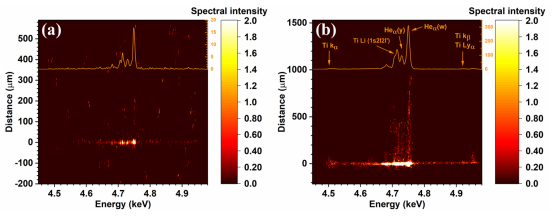

Figure 2: CCD X-ray images for the reference target (a) and composite NWs (b) providing 1D spatial imaging of the Ti X-ray source. Insets: spatially integrated X-ray spectra.

References

[1] M. A. Purvis *et al.*, Nat. Phot. **7**, 796 (2013).

[2] E. Eftekhari-Zadeh *et al.*, Phys. Plasmas **29**, 013301 (2022).

Rear Side Optical Radiation from High-Intensity Laser-Solid Interaction

S. Hell*[1], Y. Azamoum[1,2], G. A. Becker[1], M. Hornung[1,2], M. Hellwing[1], A. Kessler[1], F. Schorcht[2], and M. C. Kaluza[1,2]

[1]Institute of Optics and Quantum Electronics, FSU Jena, Germany; [2]Helmholtz Institute Jena, Germany

Rear side optical radiation emitted by relativistic (hot) electrons in high-intensity laser-plasma experiments has been studied as a function of target thickness and laser intensity. Fitting a coherent transition radiation model to the experimental results, the changes in plasma heating at the target front and hot electron temperature with laser intensity have been investigated.

During high-intensity laser-solid interactions, hot electrons are periodically accelerated by the laser once every optical cycle $\mathcal{T}_\mathrm{L}$ (through resonance absorption and vacuum heating mechanisms) and twice every $\mathcal{T}_\mathrm{L}$ (through relativistic $\vec{j}\times\vec{B}$ heating) at the target front towards the target rear [1] where they emit coherent optical radiation (COR). The COR spectrum shows peaks at multiples of the central laser frequency ω_L [2].

Laser pulses of the POLARIS laser system were focused at normal incidence onto thin aluminum foil targets ($d_0 = 0.4 - 8\,\mu\mathrm{m}$) to reach relativistic intensities ($I_\mathrm{L} \sim 10^{19}\,\mathrm{W/cm^2}$) at which the target is rapidly ionized. Using beam splitters, the rear side COR was imaged at an angle of 37° by a microscope objective and a field lens onto three cameras. Camera 1 investigated the COR at $2\omega_\mathrm{L}$ using a (520 ± 20) nm bandpass filter, camera 2 was equipped with a 1000 nm longpass filter to image COR at ω_L and camera 3 measured COR between 900 nm and 1000 nm.

Comparing the area of the COR emission spot imaged onto camera 1 and 3 shows that the COR's source size increased from 1.2 µm to 2.3 µm with target thickness, which is significantly smaller than the laser focal width (4 µm). Thus, the propagation of the diverging hot electron current was probably influenced by filamentation or pinching [3].

The total emitted COR energy W_COR (proportional to the total camera pixel count) decreases strongly with increasing target thickness d_0 (see Fig. 1). Due to the varying velocities of the hot electrons in a bunch, the longitudinal extend of the hot electron bunches increases with d_0. This results in a coherence loss which rapidly decreases the COR intensity at multiples of ω_L. A 1D CTR model [3], which assumes hot electron bunches accelerated at ω_L and $2\omega_\mathrm{L}$ with a relativistic Maxwellian energy distribution, has been fitted to the data in Fig. 1. The CTR fit converged for $T_\mathrm{h} \approx (292 \pm 22)\,\mathrm{keV}$. Additionally, the converged fit parameters show that $\simeq 60\,\%$ of the hot electrons were accelerated at $2\omega_\mathrm{L}$ and $\simeq 40\,\%$ at ω_L, in very good agreement with [2] and unaffected by I_L between $7.5 \times 10^{18}\,\mathrm{W/cm^2}$ and $1.9 \times 10^{19}\,\mathrm{W/cm^2}$. Hence, hole boring deformed the plasma surface an thus resulted in a large fraction of electrons accelerated at ω_L. The scaling of T_h with I_L can be

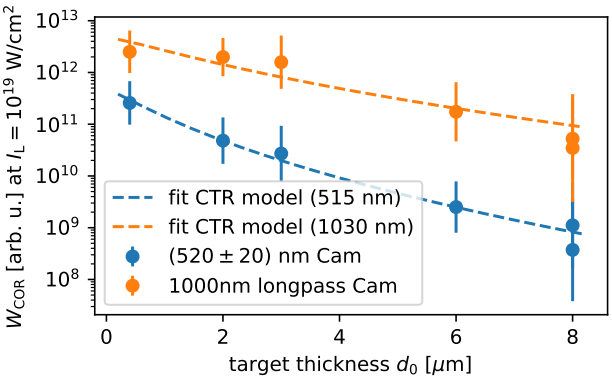

Figure 1: The COR energy W_COR emitted at 515 nm and at 1030 nm as a function of target thickness for a fixed laser intensity $I_\mathrm{L} = 10^{19}\,\mathrm{W/cm^2}$. Additionally, a CTR model [3] is fitted to the experimental data.

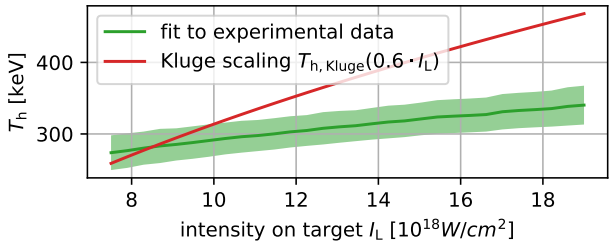

Figure 2: The hot electron temperature T_h obtained from CTR model fits (see Fig. 1) as a function of I_L. The predicted hot electron temperature [4] is plotted in red.

obtained from repeating the CTR model fit in Fig. 1 for various I_L, as shown in Fig. 2. T_h increases with I_L but less than predicted[1] by Kluge *et al.* [4]. Acquiring more data for a larger range of d_0 and I_L should be profitable for future experiments to investigate the interplay of the absorption processes and the transport of hot electrons through dense matter. This may lead to an optimal relativistic electron beam suitable for laser-based ion acceleration.

References

[1] A. Macchi *et al.*, Rev. Mod. Phys. **85**, 751 (2013).

[2] H. Popescu *et al.*, Phys. Plasmas **12**, 063106 (2005).

[3] S. Hell, Master thesis, Friedrich Schiller University Jena, 2021.

[4] T. Kluge *et al.*, Phys. Rev. Lett. **107**, 205003 (2011).

*sebastian.hell@uni-jena.de

[1]The experimental data suggests that the actual laser intensity on target is 60 % lower than the calculated value of I_L. This is included in the prediction by calculating $T_{\mathrm{h},\,\mathrm{Kluge}}$ for a reduced laser intensity of $0.6 \cdot I_\mathrm{L}$.

Betatron Radiation from Rotating Shock Front in a Laser-Driven Plasma Wakefield

Harsh Harsh*[1], Daniel Ullman[1], Felipe C. Salgado[1,2], Andreas Seidel[2], Alex Sävert[1], Ingo Uschmann[2], and Matt Zepf[1,2]

[1]Helmholtz Institute Jena, Fröbelstieg 3, 07743 Jena, Germany; [2]IOQ, FSU, Jena

Since the experimental demonstration of Laser Wakefield Accelerated (LWFA) electrons in 2004 [1], there have been various techniques developed [2] to control the injection process of electrons in the plasma bubble, which in turn affect the resultant electron beam characteristics. With a goal to produce a mono-energetic electron beam at JETI200, we implemented shock-induced density down-ramp injection and by rotating this shockfront we anticipated a change in the Betatron radiation, which is a by-product of LWFA processes. With μm source size, fs pulse duration and high photon energy (1-100 keV), Betatron radiation hence produced has multiple applications namely in pump-probe experiments and in material and biological sciences [4].

As stated in [3], the steep density drop in the down-ramp region, induced by a shock, triggers the localised injection of electrons in plasma bubble only in the down-ramp region resulting in narrow energy spread and low emittance of the electron beam. This was achieved by using Jet-Blade assembly (with He+N_2 (95% + 5%) mixture) and by varying the shock profile, position, angle and the blade coverage of the 5mm gas jet. The electron beam produced has charge $\approx$ 40 pC, divergence $<$ 10 mrad, and $\Delta E/E_{\mathrm{FWHM}} < 10$ % (Figure 2).

It has been experimentally observed that Betatron oscillations occur in the wiggler regime [4]. The radiation spectrum is a function of electron γ-factor and the electron transverse oscillation amplitude and is similar to that produced by synchrotrons. The on-axis radiated spectrum can be simplified as:

$$\left.\frac{d^2I}{dwd\Omega}\right|_{\theta=0} \simeq N_\beta \frac{3e^2}{2\pi^3\hbar\varepsilon_0 c}\gamma^2\xi^2\kappa_{2/3}^2(\xi)\,,$$

where N_β is the number of oscillations, $\hbar$ the reduced Planck constant, $\kappa_{2/3}$ the modified Bessel function of the second kind and $\xi = \frac{E}{E_{crit}}$ [3]. E_{crit} is the energy within the distribution above and below which lies half of the radiated power and is given as:

$$E_{crit} = \hbar w_{crit} \simeq 5\times10^{-24}\gamma^2\frac{n_e}{\mathrm{cm}^3}\frac{r_\beta}{\mu\mathrm{m}}\,\mathrm{keV}\,,$$

where n_e is plasma density and r_β is the source size [4]. One of the methods to find the betatron energy spectrum and photon number density is to use Ross filters [4]. By using least squares method for the filter transmission T,

$$\chi^2_{E_{crit}} = \sum_{filter}[T^{filter}_{predicted} - T^{filter}_{measured}]^2\,,$$

*harsh.harsh@uni-jena.de

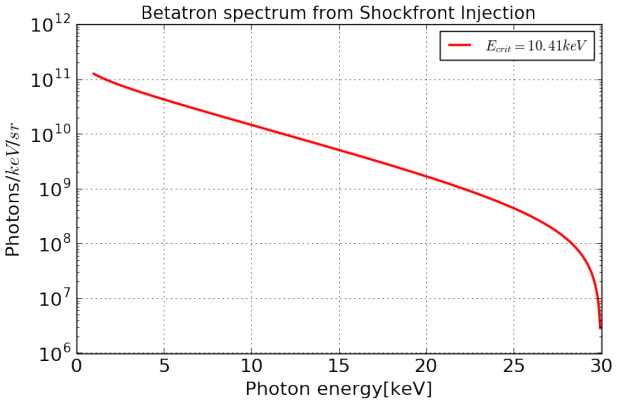

Figure 1: The beam size was 5×10 mrad^2 (FWHM), source-detector distance was 2300 mm and the source size $<$ 5 µm. The betatron spectrum peaked at 4.3 keV and E_{crit} = 10.41 keV. The peak brilliance was $\sim$ 10^{22} [Photons/(s.mm^2.mrad^2.0.1%BW)], taking source size as 1 µm and 10 fs pulse duration. A 50 µm Be filter provides the low energy cut-off ($>$ 1 keV).

we determine the critical energy (E_{crit}) where the fit-residual $\chi^2_{E_{crit}}$ reaches a minimum. Using the transmission data of the used filters from [5], quantum efficiency (QE) of the ANDOR CCD used and experimental data, we get the betatron spectrum from the shock-front injected electrons (Figure 1).

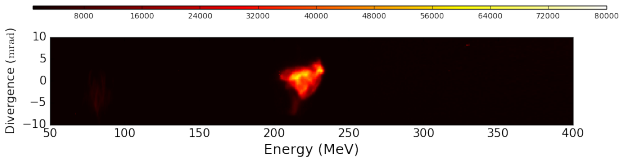

Figure 2: Quasi mono-energetic electron beam from shock-front injection recorded on a Lanex screen having $\frac{\Delta E}{E} <$ 10 % and $<$ 10 mrad divergence. The blade coverage of the jet was 30%, plasma density = 2×10^{18} cm^{-3}, with laser spot size $\approx$ 20 µm, and $\approx$ 20 fs pulse duration.

The authors acknowledge funding from ESF, EU and Freistaat Thüringen.

References

[1] S. P. D. Mangles *et al.*, Nature **431**, 535 (2004).

[2] S. Karsch, arXiv:2007.04622v1

[3] H.-E. Tsai *et al.*, Phys. Plasmas **25**, 043107 (2018).

[4] M. Schnell *et al.*, Phys. Rev. Lett. **108**, 075001 (2012).

[5] `https://henke.lbl.gov/.html`

Experimental results of the effect of laser polarization on the electron pointing jitter

A. Seidel*[1,2], C. Zepter[1,2], B. Lei[1], D. Seipt[1], and M. Zepf[1,2]

[1]HI Jena, Fröbelstieg 3, 07743 Jena, Germany; [2]IOQ Jena, Fürstengraben 1, 07743 Jena, Germany

We have performed experiments to characterize the effect of laser polarization on the electron pointing jitter. Results have shown, pointing stability in most scenarios is ultimately limited by polarization induced oscillations in the rising edge of the drive pulse.

Laser wakefield acceleration is a proven concept for the generation of extremely short electron bunches (fs) at very high energies (GeV) [1]. In the past decade, many improvements have been made to increase the performance of LWFAs in terms of reaching higher electron energies [2] and a smaller energy bandwidth [3]. However, most studies neglect the investigation of the electron pointing and its possible reduction to enable high precision electron beam positioning for subsequent applications. We conducted experiments at the Jeti200 facility to study the electron pointing. The laser delivered 2.5J on target at a wavelength $\lambda_0 = 800$ nm and pulse duration $\tau = 23$ fs resulting with an $f/24$ focusing off-axis parabola in an laser strength of $a_0 \approx 2.4$. As target, a self-developed gas cell [4] was used with an acceleration length of around 7 mm. Pure helium and a helium nitrogen gas mixture were used to deliver a plasma density in the range of $n_p = 2 \ldots 5 \times 10^{18}$ cm^{-3} enabling pure self-injection in the former case and ionization-injection in the latter one.

Experimental results for the electron pointing for horizontal(blue) and vertical(red) laser polarization indicate an increased electron pointing jitter in the direction of the laser polarization as it is shown in Figure 1. Other effects such as laser-nearfild, laser-farfield, and plasma-density gradient modulations contribute to an increased electron pointing jitter too. Note that the overall electron pointing jitter for self-injection is larger by a factor of 1.5 compared to the ionization-injection case. To estimate the effect of laser polarization on electron jitter, the ratio of horizontal and vertical electron jitter was calculated for horizontal and vertical polarization respectively as shown in Figure 2. Assuming that the total electron jitter $\sigma_T = \sigma_0 + \sigma_P$ is a superposition of polarization independent part σ_0 and polarization dependent part σ_P one can write $(\sigma_P/\sigma_0)^2 \approx \sigma_H/\sigma_V$. Averaging over all the different electron densities gives for $\sigma_P/\sigma_0 \approx 1.2$ and estimates the average effect of laser polarization on the total electron jitter to be 20% of the total electron jitter. However many factors such as the electron acceleration length, electron injection position, the blowout bubble size, and the laser pulse length are factors that contribute to the final pointing of an electron bunch. Here we reported on our experimental observation of laser polarization dependent electron beam pointing jitter. The emergence of this phenomenon can be understood in terms of a resonance between betatron oscillations and polariztion dependent bubble wobble oscillations. A detailed description of this theoretical model can be found in [5].

* seidel.andreas@uni-jena.de

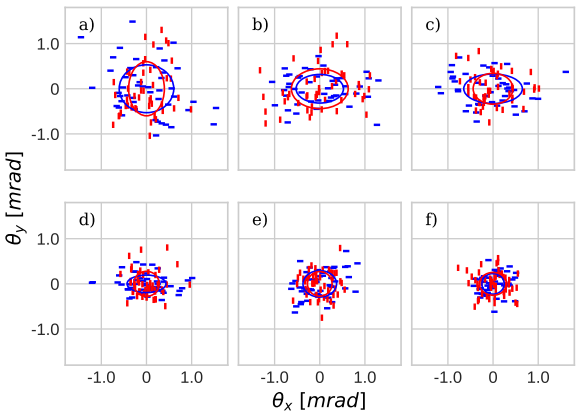

Figure 1: Experimentally measured electron pointing data in red for vertical laser polarization and blue for horizontal laser polarization. (a-c) pure Helium (self injection), and (d-f) a 95 % Helium + 5 % Nitrogen mixture (ionization injection).

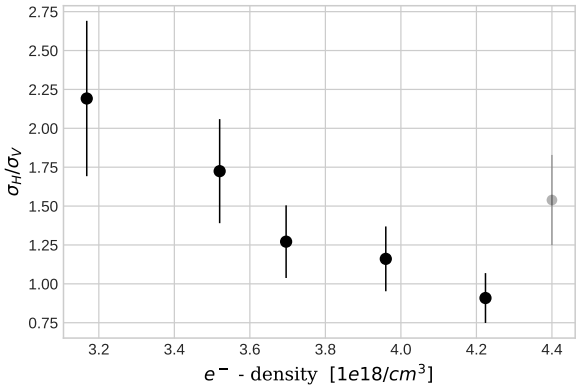

Figure 2: Magnitude of laser polarization induced electron jitter. The ratio σ_H/σ_V was calculated from data with both vertical and horizontal laser polarization.

References

[1] C. G. R. Geddes *et al.*, Nature **431**, 538 (2004)

[2] A. J. Gonsalves *et al.*, Phys. Rev. Lett. **122**, 084801 (2019)

[3] S. Jalas *et al.*, Phys. Rev. Lett. **126**, 104801 (2021)

[4] S. Kuschel *et al.*, Phys. Rev. Lett. **121**, 154801 (2018)

[5] See contribution by B. Lei *et al.* in this Annual Report.

Development of single-shot multi-frame shadowgraphy in laser-plasma interactions

Y. Zhao*[1,2], A. Sävert[1,2], and M. C. Kaluza[1,2]

[1]HI Jena, Fröbelstieg 3, 07743 Jena, Germany; [2]IOQ, FSU Jena

Ultrafast shadowgraphy with few-cycle transverse probe pulses enabled direct observation of laser-plasma interactions. However, in previous studies, only one shadowgram could be captured from each shot of the laser-plasma interaction processes. This limits our understanding of laser-plasma interactions due to the shot-to-shot fluctuations of a high-power laser system. In this study, we introduce a feasible single-shot multi-frame shadowgraphy technique based on sequentially timed all-optical mapping photography (STAMP). The experimental plans and some preliminary results are discussed in this report.

Ultrafast shadowgraphy has been successfully utilized in investigating laser-plasma interactions, which has reached femtosecond time and micrometer space resolution. In previous studies, a lengthening of the first plasma period was visualized by ultrafast shadowgraphy with near-infrared probe-pulses, providing a deeper understanding of the self-injection in laser wakefield accelerators (LWFAs) [1, 2]. However, in previous studies, only one shadowgram could be captured from each shot of the laser-plasma interaction processes. This limits our understanding of laser-plasma interaction processes because the influence of shot -to-shot fluctuations of a high-power laser system is not negligible.

In this study, we are developing a single-shot multi-frame shadowgraphy technique based on sequentially timed all-optical mapping photography (STAMP) to investigate laser-plasma interactions [3,4]. Instead of using few-cycle femtosecond probe pulses in a conventional ultrafast shadowgraphy setup, linearly chirped pulses are used as the probe. After the probe propagates through the interaction area, it is imaged by a microscopic STAMP system, which is shown in Fig. 1. A diffractive beam splitter (DE 224) is used to split the probe into five replicas (not shown in Fig. 1). Five different narrow bandpass filters (BPFs) are placed in front of a CCD camera to capture five frames that correspond to different time delays from a laser-plasma interaction. To keep the visibility of images after filtering, 10 nm (FWHM) BPFs are chosen in the current setup. The phase velocity of the laser wakefield is close to the speed of light. Thus, a sub-10 fs temporal resolution is necessary to resolve the fine structures in laser-plasma interactions. The temporal resolution of STAMP system can be estimated by [4, 5]

$$\Delta t = D \cdot z \cdot \Delta\lambda_{BPF}$$

where D (ps/km·nm) is the dispersion parameter, z (km) is the length of the dispersive media, and $\Delta\lambda_{BPF}$ (nm) is the spectral bandwidth (FWHM) of a BPF. The transmitted wavelength of a BPF depends on the incident angle [6]. Therefore, it is vital to keep all the BPFs at normal incidence. Since a diffractive beam splitter is used to split the probe, the spatial resolution of the first-order diffraction image will be distorted by chromatic dispersion. A resolution test result (Fig. 2) shows even with chromatic dispersion, the microscopic STAMP system can resolve $\sim 5\,\mu m$ lines. With this resolving power, one should be able to resolve $\sim 10\,\mu m$ fine structures in laser wakefields. This setup is planned to be tested in the upcoming beam time at the JETi200 lab this year.

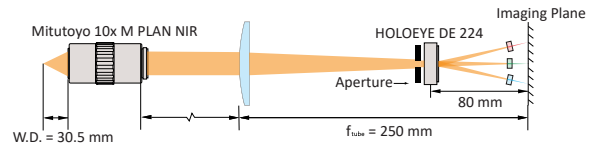

Figure 1: Schematics of the microscopic STAMP system.

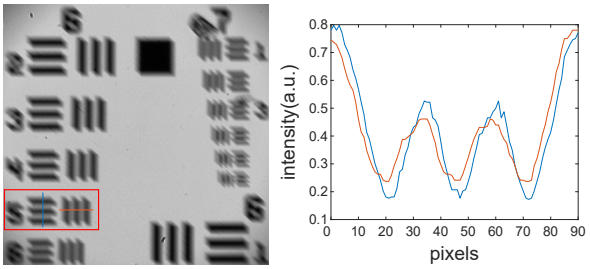

Figure 2: (a) The first-order diffraction image of a USAF 1951 resolution test target. The target was illuminated by a halogen lamp, a 10 nm (FWHM) BPF with a center wavelength at 532 nm is placed in front of the camera. The width of one line inside the red rectangular is 4.92 µm. (b) The lineout of a group of horizontal lines and vertical lines in (a), respectively.

References

[1] M. B. Schwab *et al.*, Appl. Phys. Lett. **103**, 191118 (2013).

[2] A. Sävert *et al.*, Phys. Rev. Lett. **115**, 055002 (2015).

[3] K. Nakagawa *et al.*, Nature Photonics **8**, 695 (2014).

[4] T. Suzuki *et al.*, Optics Express **23**, 30512 (2015).

[5] D. Polli, D. Brida, S. Mukamel, G. Lanzani, and G. Cerullo, Phys. Rev. A **82**, 053809 (2010).

[6] P. Gabolde and R. Trebino, J. Opt. Soc. Am. B **25**, A25 (2008).

*yu.zhao@uni-jena.de

PHOTON AND PARTICLE SPECTROSCOPY

Second Harmonic Generation in the XUV

T.Helk*[1], E. Berger[2], L. Hoffmann[3], A. Kabacinski[4], J. Gautier[4], F. Tissandier[4], J. P. Goddet[4], S. Sebban[4], C. Spielmann[4], and M. Zuerch[2,3]

[1]Helmholtz Institute Jena, Fröbelstieg 3, 07743 Jena, Germany; [2]Department of Chemistry, University of California, Berkeley, CA 94720, USA; [3]Fritz Haber Institute of the Max Planck Society, 14195 Berlin, Germany; [4]Laboratoire d'Optique Appliquee, ENSTA Paris, Ecole Polytechnique, CNRS, Institut Polytechnique de Paris, Palaiseau, France

Nonlinear responses of matter enable unique insight into properties and dynamics of matter itself. Most notably, second harmonic generation (SHG) and sum-frequency generation spectroscopy in the near infrared and optical range have enabled intriguing insights into surface properties. We report the first generation of second harmonic emission in the extreme ultraviolet (XUV) at the titanium M-edge with a high-harmonic seeded soft X-ray laser, bringing nonlinear XUV spectroscopy with atomic specificity to the table-top.

SHG facilitate that the second-order nonlinear response is only allowed at inversion symmetry broken surfaces and interfaces in otherwise inversion symmetric bulk materials [1]. A high-harmonic seeded SXRL beam [2] with an input energy of (111 ± 23) nJ, pulse duration of (1.73 ± 0.13) ps, wavelength of 32.8 nm (37.8 eV) and a Gaussian-like beam profile was tightly focused, using an Au-coated ellipsoidal mirror, onto a 50 nm Ti foil (4.5 ± 1.5) μm, and average intensity of $(4.1 \pm 1.9) \times 10^{11}$ W/cm^2. The fundamental SXRL beam and second harmonic at 75.6 eV, are refocused using a toroidal mirror onto a deep-cooled charged coupled device (CCD) [3]. The observed line width is poorly resolved in this experiment where the spectrometer was optimized to cover more than one octave at low resolution to achieve a high sensitivity to observe the SHG signal (see Fig. 1).

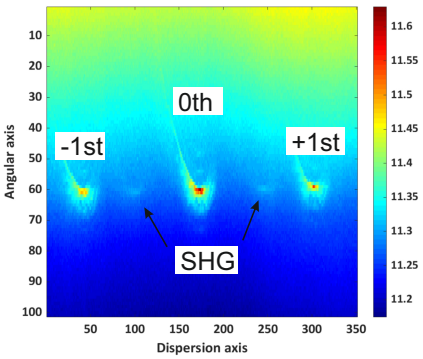

Figure 1: Experimental results. Accumulation of 146 raw shots. Zeroth and ±1st order of diffraction can been seen, arrows pointing at the weak SHG-signal.

An additional observed broadened line width of the second harmonic is due to aberrations of the imaging spectrometer. Each laser shot was sorted into a histogram, classified by the yield of the first diffraction order signal (positive and negative) of the fundamental and SHG signal. As a result, Fig. 2 depicts a quadratic dependence of the SHG signal (red curve). result, Fig. 2b depicts a quadratic dependence of the SHG signal (see red curve in Fig. 2b). Using the measured mean yield of the SHG and fundamental, one can estimate the photon flux at the titanium foil. The pulse energies of (6.2 ± 0.2) pJ and (3.04 ± 0.2) nJ for the SHG and the fundamental, respectively, correspond to a conversion efficiency $\eta = (0.023 \pm 0.005)$.

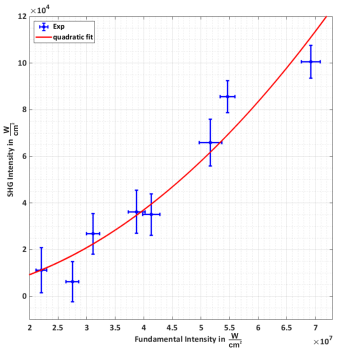

Figure 2: SHG-Intensity dependence from fundamental input. Back-calculated intensities at the surface of the Ti-foil. The quadratic dependence of the SHG is indicated with a quadratic fit, red line.

In conclusion, we have shown the first successful demonstration of SHG in the XUV. The experiments were done at a table-top source showing great promise for more widespread use of this new realm.

The authors acknowledge funding from European Community's Horizon 2020 research and innovation program under grant agreement No. 654148. This work is supported by Investissements dAvenir Labex PALM (ANR-10-LABX-0039-PALM).

References

[1] R. Boyd, Nonlinear Optics (Third Edition), Academic Press (2008).

[2] S. Sebban *et al.*, Plasma Physics and Controlled Fusion **60**, 014030 (2017).

[3] T. Helk *et al.*, Science Advances **7**, 21 (2021).

*tobias.helk@uni-jena.de

Investigation of encapsulated graphene using XUV coherence tomography

F. Wiesner*[1,2], S. Fuchs[1,2], S. Skruszewicz[3], J. Reinhard[1,2], M. Wünsche[1,2], J. J. Abel[2], J. Nathanael[1,2], C. Rödel[1,2,4], and G. G. Paulus[1,2]

[1]Helmholtz Institute Jena, Fröbelstieg 3, 07743 Jena; [2]Institute of Optics and Quantum Electronics, Friedrich Schiller University Jena; [3]Deutsches Elektronen Synchrotron DESY, Notkestraße 85, 22607 Hamburg ; [4]Institute of Nuclear Physics, TU Darmstadt, Schlossgartenstraße 9, 64289 Darmstadt

We present results of the characterization of graphene flakes buried beneath 200 nm of silicon using extreme ultraviolet coherence tomography. In the tomograms, mono-, bi- and trilayers of graphene can be identified and the thickness of a capping layer is characterized. Furthermore, we can estimate the quality of the graphene interface by incorporating a model that includes the interface roughness.

Extreme ultraviolet coherence tomography (XCT) is a non-destructive cross-sectional imaging technique [1] with high sensitivity and an axial resolution on the order of a few ten nanometers. XCT is performed in a common-path interferometric scheme (Fig. 1a)). Broadband extreme ultraviolet light from a high-harmonic source is focused onto a sample and the reflection is measured with a high-resolution spectrometer. Interference from light reflected in different depths of the sample modulates the reflected spectrum. Hence, the depth structure can be recovered by a Fourier-based algorithm. However, this method reconstructs the autocorrelation of the sample's depth structure rather than the actual structure because the necessary phase information is lost in the detection process. Nevertheless, with a one-dimensional phase retrieval algorithm (PR-XCT) the reconstruction of the sample structure from its autocorrelation becomes possible [2]. Combined with lateral scanning of the sample, three-dimensional artifact-free tomograms can be generated.

Here, we used XCT to investigate graphene layers encapsulated in a Si matrix. Different sample consisting of different amounts of graphene buried under $200\,\mathrm{nm}$ thick capping layers of amorphous silicon [3] have been characterized. In order to investigate areas of $25\,\mathrm{mm}^2$, a lateral stepsize of $250\,\mu\mathrm{m}$ was chosen. The depth resolution is about $\Delta z = 27\,\mathrm{nm}$. 3D tomographic images (Fig. 1b)) show that the reflectivity is enhanced in the area where the graphene layer is deposited. A weak background signal of a native oxide layer beneath the graphene is also visible. XCT is able to differentiate between monolayers, bilayers, and trilayers of graphene by measuring a reflectivity that increases with the number of layers (Fig. 1c)). In addition to the number of graphene layers, the reflectivity is strongly affected by roughness and the formation of native oxides at the interfaces. We show that by incorporating these effects in a parameterized model, the experimentally obtained reflectivities can be reproduced. As a result, even the roughnesses and oxide thicknesses can be quantified. The application of XCT on the characterization of 2D materials is not restricted to graphene encapsulated in Si. A wide range of functional layers and encapsulating materials can be imaged. We expect that XCT can be developed as an important tool for quality control of nanoelectronic devices and as a method for studying the physics of such devices.

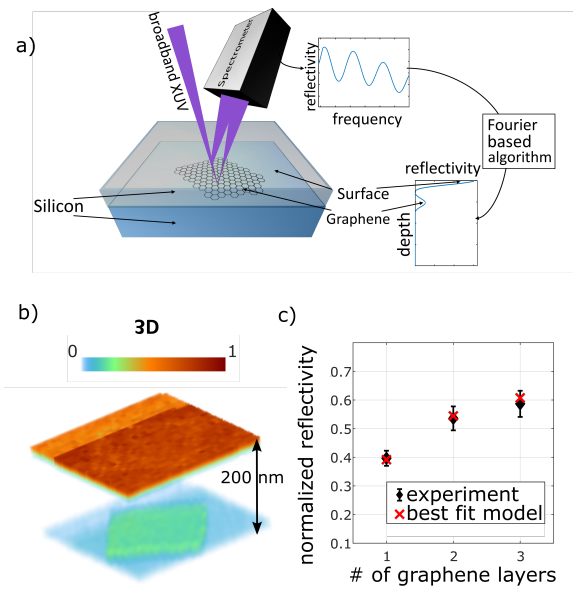

Figure 1: Measurement of encapsulated graphene using XUV coherence tomography: a) Broadband XUV is focused onto a sample which consists of graphene encapsulated in silicon. Interference of the reflections at different depths modulates the reflected spectrum. Through a Fourier-based reconstruction algorithm the sample structure can be obtained. b) Tomogram of a graphene monolayer under a 200-nm capping layer. c) Averaged normalized reflectivities for three samples with monolayer, bilayer and trilayer of graphene in comparison to a model incorporating interface roughness and native oxidation.

The authors acknowledge funding from the Thüringer Aufbaubank (2015FGR0094, 2018FGR0080) , the DFG (Beethoven 2 Lab-XCT) and the Helmholtz excellence network (ExNet).

References

[1] S. Skruszewicz *et al.*, Appl. Phys. B **127**, 55 (2021).

[2] S. Fuchs *et al.*, Optica, **4**, 903 (2017).

[3] F. Wiesner *et al.*, *to be submitted.*

* felix.wiesner@uni-jena.de

Photon counting of high harmonics using a superconducting nanowire single-photon detector

S. Fuchs*[1,2], J. J. Abel[2], J. Nathanael[1,2], J. Reinhard[1,2], F. Wiesner[1,2], M. Wünsche[1,2], S. Skruszewicz[3], C. Rödel[4], D. Born[5], H. Schmidt[5], and G. G. Paulus[1,2]

[1]Helmholtz Institute Jena, Fröbelstieg 3, 07743 Jena; [2]Institute of Optics and Quantum Electronics, Friedrich Schiller University Jena; [3]Deutsches Elektronen Synchrotron DESY, Notkestraße 85, 22607 Hamburg ; [4]Institute of Nuclear Physics, TU Darmstadt, Schlossgartenstraße 9, 64289 Darmstadt; [5]Leibniz Institute of Photonic Technology (IPHT), Albert-Einstein-Str. 9, 07745 Jena

We present, in a proof-of-concept experiment, that superconducting nanowire single-photon detectors (SNSPD) can be utilized for photon counting of a laser-driven extreme ultraviolet (EUV) source based on high harmonic generation (HHG). SNSPDs are dark-count free and accommodate very high count rates - a perfect match for high repetition rate HHG sources. The ability to count single photons paves the way for very promising applications in quantum optics and quantum imaging with high energetic radiation.

In the past, photon counting in the EUV and SXR range has usually been implemented by applying electron multiplier multichannel plates (MCP). However, these devices suffer from low efficiencies limited by the open area ratio of the device, high dark count rates, and limited count rates. For harder X-rays, CCD cameras can detect single photons and thus can be used as counting detectors, but the above-mentioned readout-time limits persist. For lower energy photons, counting with CCDs is not possible due to read-out noise.

Here, we demonstrate that superconducting nanowire single-photon detectors (SNSPDs) [1], which originally were designed for infrared radiation, can directly be utilized for photon counting of EUV radiation from laser-driven high harmonic sources [2]. These detectors, invented almost two decades ago, are based on breaking cryo-cooled superconductivity in a very thin and narrow cryogenic-cooled nanowire when a photon is absorbed. When applied to EUV radiation, SNSPDs have two major advantages in comparison to other single-photon detectors like above-mentioned avalanche photo diodes or multiplier tubes. The recovery time lies in the range of a few nanoseconds or even picoseconds and thus SNSPDs can achieve count rates up to several GHz. This makes SNSPDs a perfect match to the repetition rate of state-of-the-art high-flux HHG sources driven by a repetition rate of several 100 kHz.

For the proof-of-concept study a SNSPD was illuminated with EUV radiation from an HHG source. EUV photons up to an energy of 72 eV were used. The SNSPD consists of a 10 nm thick and 100 nm wide meandered niobium nitride nanowire with a gap size of 100 nm, resulting in an active area of about $4.8 \times 4.8\,\mu m^2$. It was placed in the diverging EUV beam. At a bias current of 62 μA, a photon count rate of 940 events per minute was achieved.

*silvio.fuchs@uni-jena.de

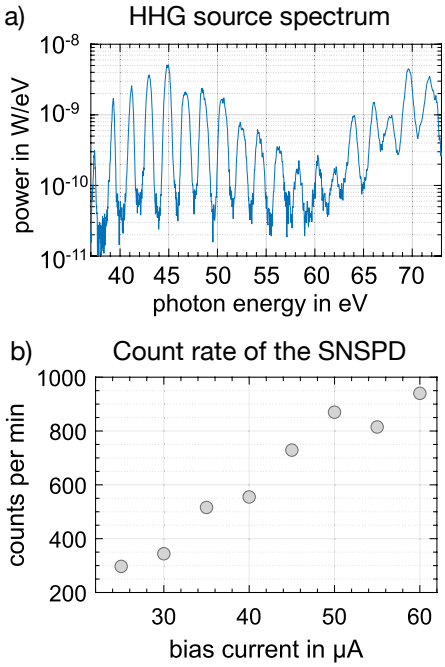

Figure 1: a) Spectrum of the HHG source. b) Count rate of the SNSPD depending on the bias current through the nanowire

Our findings prove that a single-photon detector based on superconducting nanowires can be utilized for photon counting of EUV photons in particular from a laser-driven HHG source with very low dark count rates. The presented proof-of-concept paves the way for future applications of SNSPDs and other cryogenic detector schemes like microcalorimeters or superconducting tunnel junctions for laser-based high harmonic light sources in coherent imaging, EUV quantum optics, and quantum imaging.

The authors acknowledge funding from the Thüringer Aufbaubank (2015FGR0094, 2018FGR0080 and Quantum Hub 2021FGI0049), the German Federal Ministry for Education (BMBF) (VIP "X-CoherenT"); AppQuant (ZF4006821DF9) and German Research Foundation FG IR-TG Meta Active (DFG-RTG 2675).

References

[1] E. Knehr *et al.*, Supercond. Sci. Technol. **32**, 125007 (2019).

[2] S. Fuchs *et al.*, Applied Phys. B, **128**, 26 (2022).

Improvements of Computational Ghost Imaging by Using Sequenced Speckle Patterns

Sukyoon Oh*[1,2], Zhe Sun[1,2], and Christian Spielmann[1,2]

[1]Institute of Optics and Quantum Electronics, Max Wien Platz 1, 07743 Jena, Germany; [2]Helmholtz Institute Jena, Fröbelstieg 3, 07743 Jena, Germany

In this report, the influence of the sequenced speckle pattern on the contrast-to-noise ratio (CNR) is examined in Computational Ghost imaging. The result shows that the sequential Ghost Imaging method provides ghost images with a better CNR compared to the traditional GI (TGI) at the almost same resolution. We verify also better CNR in certain speckle composition groups, which is over 10 times faster than traditional methods with close resolution.

Ghost imaging (GI) nonlocally obtains the object information by correlating two beams, one beam interacts with an object and is collected by a single-pixel detector, the other beam has never interacted with the object and is recorded by a spatially resolved array detector. The first GI experiment relied on quantum entangled photons generated by spontaneous parametric down-conversion. Later, the GI was also demonstrated with thermal and pseudo-thermal light based on random patterns [1]. In the computational GI (CGI), the scatter beam generated after a laser beam transmitted through a spatial light modulator (SLM) or a digital micro-mirror device (DMD) [2]. In this way, GI can be simplified as one beam path with only a single-pixel detector, by precomputing the speckle patterns. An indirect imaging method that acquires the image of an object through spatial intensity correlation measurements both in the PGI and the CGI [3, 4].

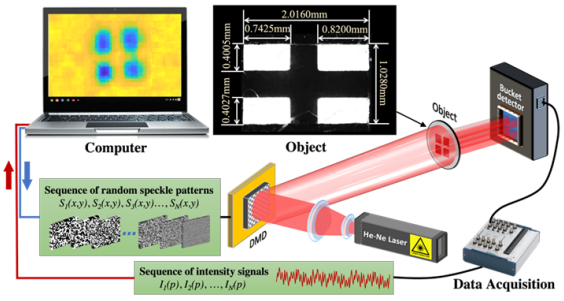

Figure 1: Side view SEM images of NWs (a), measured proton spectra (c) for nanowires (solid red line) and for reference target (solid blue line). Insets: raw IP images of proton spectra for the reference and NWs.

The experimental setup to study the influence of the sequenced speckle pattern on the CNR of ghost image is shown in Figure 1. A He-Ne laser is expanded and then randomly modulated by the DMD. The random speckle pattern projection system was based on a DMD as the intensity modulation element. In the experiment, we sequentially displayed a set of 1024×768 digitally micro-scanned patterns on DMD. The sequenced random speckle patterns pass through the object to be imaged. The transmitted intensity signals are received by the bucket detector. The retrieved ghost image is reconstructed by the correlation of the intensity signals and the sequenced random speckle patterns. To demonstrate the feasibility and performance of SGI, a laser-cut window-shaped transmitting object was prepared as the object.

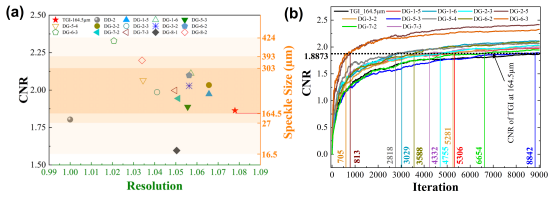

Figure 2: CCD X-ray images for the reference target (a) and composite NWs (b) providing 1D spatial imaging of the Ti X-ray source. Insets: spatially integrated X-ray spectra.

In conclusion, the sequenced random speckle patterns with different speckle sizes are beneficial to the quality of the reconstructed image in the DMD-based CGI. Compared to the traditional random speckle patterns, better CNR and resolution can be achieved with fewer iterations, especially when reconstructing images with suitable sequenced speckle patterns is used. The best image quality in the SGI is obtained when the speckles area is in the range of 1/10 to 3/10 of the reference object area. This provides a reference to further optimize the imaging quality of the SGI.

Work supported by State of Thuringia within the project "Quantum Hub Thüringen"; DAAD (Deutscher Akademischer Austauschdienst) German Academic Exchange Service, Funding programme.

References

[1] Z. Sun, F. Tuitje, and C. Spielmann, J. Microsc. **284**, 3 (2021).

[2] W.-K. Yu, X.-F. Liu, X.-R. Yao, C. Wang, Y. Zhai, and G.-J. Zhai, Sci. Rep. **4**, 5834 (2014).

[3] Z. Sun, F. Tuitje, and C. Spielmann, Opt. Express **27**, 33652 (2019).

[4] Z. Sun, F. Tuitje, and C. Spielmann, Appl. Sci. **11**, 2621 (2021).

* Sukyoon.oh@gsi.de

Advanced X-ray polarimeter design for nuclear resonant scattering

B. Marx-Glowna*[1,2], I. Uschmann[2,1], K.S. Schulze[1,2], H. Marschner[2], H.-C. Wille[3], K. Schlage[3], Th. Stöhlker[1], R. Röhlsberger[1,2,3], and G.G. Paulus[2,1]

[1]Helmholtz-Institut Jena, Fröbelstieg 3, 07743 Jena, Germany; [2]Institut für Optik und Quantenelektronik, Friedrich-Schiller-Universität Jena, Max-Wien-Platz 1, 07743 Jena, Germany; [3]Deutsches Elektronen-Synchrotron DESY, Notkestr. 85, 22607 Hamburg, Germany

We have developed an advanced X-ray polarimeter for nuclear resonant scattering experiments, which is now available for users at beamline P01 of the storage ring PETRA III. The new polarimeter provides a hitherto unachieved degree of polarization purity of 2×10^{-9} for the nuclear resonance of ^{57}Fe. The mounting of the analyzer on a 2θ-arm of a $\theta - 2\theta$ goniometer allows users to perform polarization-dependent investigations of layer systems in reflection geometry.

Nuclear resonant scattering of synchrotron radiation (NRS) is an established methodology ranging from the study of structure and dynamics of condensed matter to the realization of quantum optical phenomena. Nuclear resonances have a very narrow energy bandwidth of typically 10^{-7} to 10^{-11} eV. In case of ^{57}Fe the natural linewidth is 4.7 neV. One possibility to separate the resonantly scattered photons from the energetically broad synchrotron beam is to use the time discrimination method in combination with polarization filtering. The polarization filtering technique makes use of the strong optical activity that is inherent to the nuclear scattering process. By using an X-ray polarimeter it is possible to filter the resonantly scattered photons that have undergone a change in their polarization state, e.g. if the nuclei are exposed to a symmetry breaking magnetic or electric hyperfine interaction. Our polarimeter was developed for a permanent installation at the High-Resolution Dynamics Beamline P01 at PETRA III (DESY, Hamburg). To polarize the radiation, we use crystalline reflections with Bragg angles close to $45°$ which is the Brewster angle for hard X-rays. The silicon (840) reflection provides a Bragg angle of $\theta_B = 45.1°$ for the 14.4 keV nuclear resonance of ^{57}Fe. The use of four asymmetric reflections at asymmetry angles of $\alpha_1 = -28°$,$\alpha_2 = 28°$,$\alpha_3 = -28°$ and $\alpha_4 = 28°$ for the polarizer as well as the analyzer (see Fig. 1) allows on the one hand a better suppression of the π-component and on the other hand an improvement of the angular acceptance for the incoming radiation. For a permanent installation of the polarimeter on beamline P01 the four-reflection channel-cut of the polarizer is separated into two two-reflection channel-cuts in antiparallel (n,+n) setting. This allows the polarimeter to be inserted into the beam path without leading to a beam offset. We have characterized the performance of the polarimeter at beamline P01 by measuring the degree of polarization purity. The degree of polarization purity δ_0 is defined as the ratio of the transmission of the π-polarization component to the transmission of the σ-polarization component. We could determine δ_0 to $2.2 \cdot 10^{-9}$. Fig. 2 shows as an example a temporal beat pattern from a 9.3μm ^{57}Fe enriched film, measured with the designed polarimeter. The use of the polarimeter allows for an almost full suppression of non-resonantly scattered photons, indicated by the green arrow in Fig.2. In contrast to other NRS methods, in this experiment the polarization filtering allows to record the delayed nuclear resonant scattering already 1.5 ns after excitation. This will enable, for example, to probe short-lived isotopes like ^{169}Tm and ^{187}Os with lifetimes of 5.9 and 3.4 ns, respectively. Moreover, the early times after resonance excitation are highly interesting to reveal the early-stage temporal dynamics of cooperative effects like superradiance or the collective Lamb shift in x-ray quantum optics.

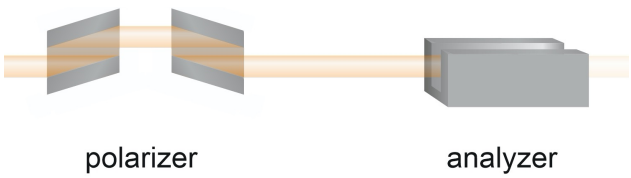

Figure 1: Schematic setup of the polarimeter. This consists of a four-reflection polarizer without beam offset and a four-reflection analyzer.

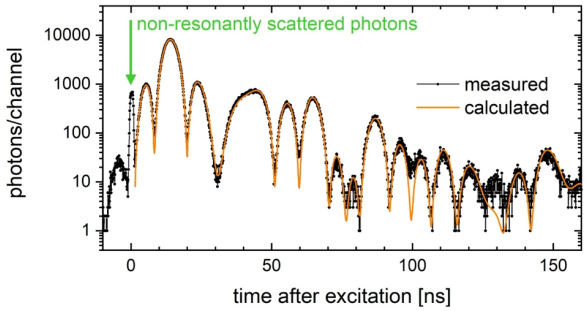

Figure 2: Temporal beat pattern of a 9.3 μm thick foil of ^{57}Fe, magnetized at $45°$ to the incident σ polarization.

The authors acknowledge funding from the BMBF project 05K2013 PolarX..

References

[1] B. Marx-Glowna, I. Uschmann, K. S. Schulze, H. Marschner, H.-C. Wille, K. Schlage, Th. Stöhlker, R. Röhlsberger, G. G. Paulus, J. Synchrotron Rad. **10**, 28 (2021).

*berit.marx@uni-jena.de

Cross section analysis in Rayleigh scattering of linearly polarized x-rays

W. Middents*[1,2], G. Weber[2,3], M. Vockert[1,2], U. Spillmann[3], P. Pfäfflein[1,2,3], A. Gumberidze[3], T. Krings[4], N. Kurz[3], S. Strnat[5,6], A. Surzhykov[5,6], and Th. Stöhlker[1,2,3]

[1]IOQ Jena, FSU Jena, Max-Wien-Platz 1, 07743 Jena, Germany; [2]HI Jena, FSU Jena, Fröbelstieg 3, 07743 Jena; [3]GSI Darmstadt, Planckstr. 1, Darmstadt; [4]IKP Jülich; [5]PTB Braunschweig; [6]TU Braunschweig

Analyzing the angular distribution of Rayleigh scattered x-rays allows for a determination of the polarization of the incident photon beam when relying on precise theoretical calculations.

For photon energies below 1 MeV elastic scattering of photons on atomic targets is dominated by Rayleigh scattering. This second order quantum electrodynamical process describes scattering of a photon by an atomic electron without loss or gain of energy [1]. The angular-differential scattering cross section of a linearly polarized incident photon beam is given by [2]

$$\frac{d\sigma}{d\Omega} = \left(|A_{\parallel}|^2 + |A_{\perp}|^2\right) + \left(|A_{\parallel}|^2 - |A_{\perp}|^2\right) \cdot \left(P_{1i}\cos(2\varphi) + P_{2i}\sin(2\varphi)\right) \quad (1)$$

with P_{1i} and P_{2i} being the Stokes parameters of the incident beam polarization and φ being the azimuthal scattering angle between the polarization plane of the incident beam and the wave vector of the scattered photon. The parallel $A_{\parallel}$ and perpendicular $A_{\perp}$ scattering amplitudes, depending on the photon energy $\hbar\omega$ and the polar scattering angle θ between incident and scattered photon, describe the scattering process. They were calculated within the independent particle approximation (IPA) which is known to work well in the regarded energy regime [3].

In October 2020 we performed a measurement at PETRA III facility at DESY on scattering of a highly linearly polarized synchrotron beam ($\hbar\omega = 175$ keV) on a thin gold target. This experiment focused mainly on the polarization characteristics of the scattered photon beam under different polar and azimuthal scattering angles utilizing a 2D sensitive Si(Li) strip detector as Compton polarimeter [4]. Additionally the angular scattering distribution was analyzed both with a standard Germanium detector that was positioned within the synchrotron plane ($\varphi = 0°$) and with the Si(Li) detector under different azimuthal scattering angles.

The angular-differential scattering cross sections measured with the Germanium detector is shown in Fig. 1. We also present theoretical predictions, based on IPA theory in which the summation over occupied electron shells is restricted to K, KL and KLM shells. For the comparison with the experimental data eq. 1 is fitted to the data with $\varphi = 0°$ and P_{1i} as fitting parameter. While for larger scattering angles the cross section is dominated by scattering on K-shell electrons, contributions from higher electron shells become dominant at forward scattering angles. Fig. 2 shows the angular-differential scattering cross section, also including the data taken with the Si(Li)-detector for $\varphi \neq 0°$. A fit of eq. 1 allowed us to determine the linear polarization of the incident synchrotron beam to $P_{li} = (0.989 \pm 0.003)$. The shown results are only preliminary and so far unpublished.

*wilko.middents@uni-jena.de

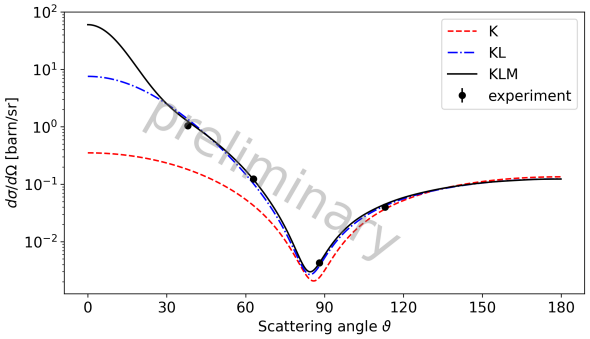

Figure 1: Angular-differential cross section of Rayleigh scattering of 175 keV x-rays on a gold target. The sacttered photons were detected within the polarization plane of incident radiation. The theoretical curves rely on calculations within the IPA were only the K , KL or KLM shells were considered.

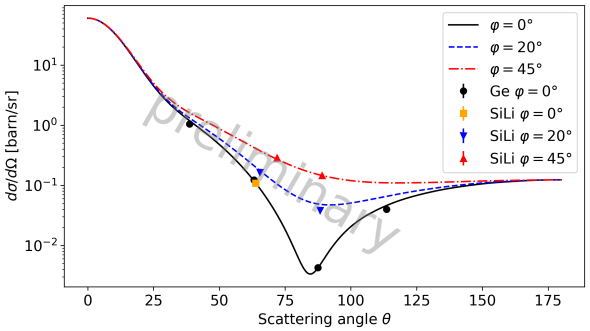

Figure 2: Angular-differential cross section for Rayleigh scattering of 175 keV x-rays on gold within and out of the polarization plane of the incident beam. The lines provide a theoretical fit according to eq. 1.

The authors acknowledge funding from ErUM-FSP APPA (BMBF n° 05P19SJFAA).

References

[1] S. Roy *et al.*, Rad. Phys. Chem. **41**, 725 (1993).
[2] S. Roy *et al.*, Phys. Rev. A **34**, 1178 (1986)
[3] A. Surzhykov *et al.*, Phys. Rev. A **98**, 053403 (2018)
[4] W. Middents *et al.*, HI-Jena annual report (2020)

Avoiding Umweganregungen in X-ray polarizers

W. Hippler*[1], K. S. Schulze[1], R. Loetzsch[2], B. Marx-Glowna[1], I. Uschmann[1,2], and G. G. Paulus[1,2]

[1]HI Jena, Fröbelstieg 3, 07743 Jena, Germany; [2]IOQ, FSU Jena

High purity X-ray channel-cut polarizers are based on Bragg diffraction at 45°. Umweganregungen, i.e. Bragg diffraction involving more than one lattice plane, can lead to a degradation of polarization purity. In order to avoid it, the azimuthal orientation of the channel-cut crystal has to be adjusted very precisely. We developed a new method to accomplish this by measuring the Umweganregungen directly with the Borrmann effect. With this method, the crystal can be aligned as precisely as 0.01° in a comparatively short time.

Following the development of polarimeters with extremely high linear polarization purities, new interesting experiments come into reach of experimental capabilities. One of these is the measurement of the birefringence of vacuum exposed to very strong electromagnetic fields. However, there are two fundamental limitations for the polarization purity of channel-cut polarizers, namely the divergence of the source and Umweganregungen inside the polarizer crystals. Calculations for different channel-cuts, especially for high photon energies, show that polarization purities of better than 10^{-11} are only achievable, if the azimuthal angle with respect to the incident beam is very precisely adjusted. Often an alignment better than $\pm 0.01°$ around the sweet spot of an azimuthal angle of 45° is required [1].

The developed method to achieve this is based on the anomalous transmission close to Bragg reflections, known as Borrmann effect. Besides the incident angle Θ and the azimuthal angle, the tilt of the crystal turned out to be very important as well. In Fig. 1 the dependence of the simulated transmission of Cu-Kα-radiation through a 1-mm Silicon crystal on Θ and the azimuthal angle is shown for two different tilt angles. The 400 Bragg reflection is at $\Theta = 34.5°$. The basic idea of the adjustment method is to find intersection points of reflections, that are symmetrical to the azimuthal angle of 45°. These intersections are exactly on the azimuthal sweat spot, provided the tilt angle is zero. Therefore, in a first step, the tilt has to be adjusted by measuring the difference of the azimuthal angles of two intersection points. The tilt is zero, when this difference equals zero. With adjusted tilt, the intersection points already mark the right azimuthal angle.

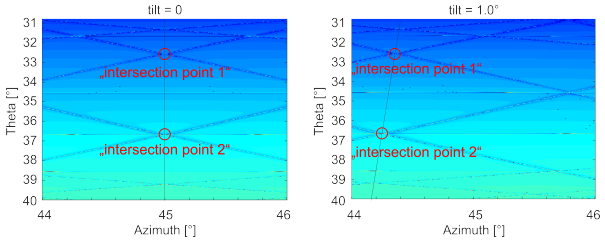

Figure 1: Simulated Transmission of Cu-Kα-radiation through a 1-mm Silicon crystal.

In a proof-of-principle experiment, we performed this method on a thin silicon crystal and a thin diamond crystal, both with a 400 surface. The experiment was set up at a rotating anode X-ray tube. Within one hour, it was possible to adjust the tilt such that two intersection points had the same azimuthal angle and to measure this angle with an error of $\pm 0.01°$. Fig. 2 documents the alignment process for the diamond crystal. Since diamond absorbs much more intensity than silicon, here we did not use the anomalous transmission, but the anomalous absorption. At brilliant sources such as XFELs or synchrotrons, first results show that this method will work there even better than with the test setup. For a recent campaign at the HED beamline of EU-XFEL, a Si-800 cannel-cut polarizer was modified by extruding one of its walls to a thin "lip", that served for the procedure just described. For future experiments, our new method offers an approach to achieve excellent polarization purities in a short time.

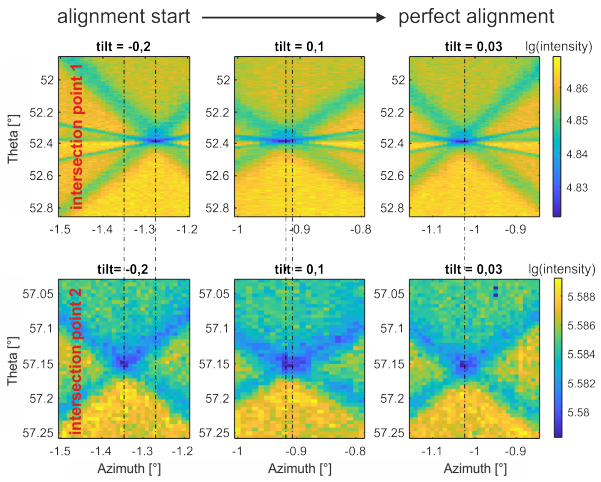

Figure 2: Measured Transmission of Cu-Kα-radiation through a 1-mm diamond crystal.

References

[1] K. S. Schulze, APL Photonics **3**, 126106 (2018).

*willi.hippler@uni-jena.de

Darkfield Set-up for X-ray scattering experiments

D. Ullmann[1,2], I. Uschmann[1,2], and M. Zepf[1,2,3]

[1]Faculty of Physics and Astronomy, Friedrich-Schiller-Universität Jena, 07743 Jena, Germany; [2]HI Jena, Fröbelstieg 3, 07743 Jena, Germany; [3]GSI Helmholtzzentrum für Schwerionenforschung, Planckstraße 1, 64291 Darmstadt, Germany

X-ray scattering experiments are frequently limited by direct x-rays from the primary beam masking the desired scattering signal. We investigate the level of primary beam suppression that can be achieved in a matched aperture set-up with the aim of eliminating primary beam components which are indistinguishable from the scattered signal just prior to the experiment.

X-ray scattering techniques are ubiquitous in modern synchrotrons and FELs. For FELs the short pulse duration and excellent focusability allow ultrafast phenomena to be probed efficiently. The typical limit of any scattering set-up are the primary beam photons that propagate along the same path as the scattered x-ray signal. For an x-ray beam with a notional Gaussian distribution, the actual signal level can exceed that of an ideal Gaussian by many orders of magnitude.

We report on an experiment using an X-ray tube set-up to estimate the improvement that is possible with a matched aperture set-up. Figure 1 depicts the experimental concept. The collimated x-ray beam is shaped using a beam block matched to a selecting aperture with the aim of establishing the reduction that is available in such a straightforward set-up. A portion of the beam is blocked by an opaque object, e.g. by an Au wire, therefore generating a shadow blocking certain spatial/angular components of the beam. A matched downstream aperture blocks the remaining primary beam resulting in a dark-field type set-up, with any scattering taking place between block and the aperture providing signal against a low back-ground. We note that geometries with a focusing geometry should deliver fundamentally the same results.

The success of this concept crucially depends on the efficiency of the x-ray block. We quantified the shadow purity in a series of experiments at the Helmholtz Institute Jena using a 1.2 kW copper anode. This beam is collimated by a confocal multilayer optic yielding approximately 5×10^9 Cu-Kα 8 keV photons per second with a divergence of 0.4 mrad within a rhombic beam profile with side lengths of 2 mm. An Au wire of 500 µm diameter serves as beamstop and photons beyond this region are blocked by a 2 mm tungsten slit. We reduce the scattering from the wire and slit by placing the wire-slit assembly between two parallel, polished Si crystals using the 400 reflex. The resulting signal is recorded on an x-ray CCD (Roper PI-MTE:2048B). Images without the slit and wire were acquired over 500 ms and serve as reference for the results of the shadow images, which were exposed for 1000 s.

The background subtracted results are projected along the shadow axis and shown in Fig. 2. In case of the unblocked beam, approximately 75×10^3 photons/s were detected within the slit region, whereas 3 photons were observed in a 1000 s exposure in case of the shadow setup. Including the different exposure times, we obtain a signal reduction by 8 orders of magnitude, 100 $\times$ less than the scatter observed from a Si-crystal.

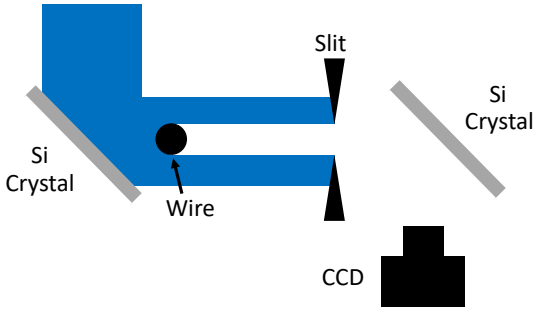

Figure 1: Experimental setup. The x-ray beam (blue) is blocked by a wire and casts a x-ray shadow. The remaining beam fraction is stopped by the slit. The shadow is recorded on a CCD camera.

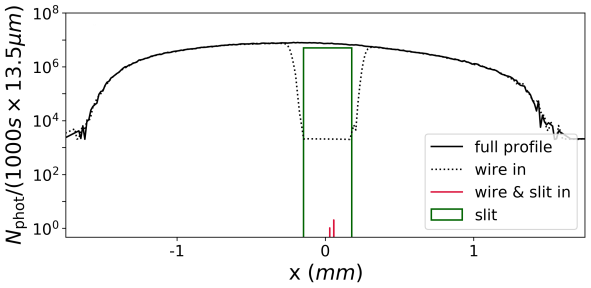

Figure 2: Resulting x-ray profile after background subtraction and projection along the wire shadow. Shown are the full profile (black), full profile with inserted Au wire and the resulting shadow for installed wire and slit. The green box indicates the slit position.

Clearly, the reduction of the background significantly improves the signal to noise ratio. This enables laboratory investigation of very low scattering levels in a variety of experiments ranging from linear to non-linear scattering phenomena. We anticipate benefits for experimental exploration of scattering phenomena at the Helmholtz International Beamline for Extreme Fields (HIBEF) at the European XFEL.

References

[1] S. Baumbach *et al.*, Rev. Sci. Inst. **86**, 083708 (2015)

Coherent X-ray optical control of nuclear excitons

K. P. Heeg[1], A. Kaldun[1], C. Strohm[2], C. Ott[1], R. Subramanian[1], D. Lentrodt[1], J. Haber[2], H.-C. Wille[2], S. Goerttler[1], R. Rüffer[3], C. H. Keitel[1], R. Röhlsberger[2,4,5], T. Pfeifer[1], and J. Evers[1]

[1]Max-Planck-Institut für Kernphysik, Heidelberg, Germany; [2]DESY, Hamburg, Germany; [3]The European Synchrotron Radiation Facility (ESRF), Grenoble, France; [4]Helmholtz Institute Jena, Germany; [5]Friedrich-Schiller-Universität Jena, Germany

Coherent control of quantum dynamics is key to a multitude of fundamental studies and applications. In the visible or longer-wavelength domains, near-resonant light fields have become the primary tool with which to control electron dynamics. At hard-X-ray energies, Mössbauer nuclei feature narrow nuclear resonances due to their recoilless absorption and emission of light, and spectroscopy of these resonances is widely used to study the magnetic, structural and dynamical properties of matter. It has been shown that the power and scope of Mössbauer spectroscopy can be greatly improved using various control techniques. Here we employ the tunable phase between two X-ray pulses to switch the nuclear exciton dynamics between coherent enhanced excitation and coherent enhanced emission.

Here we demonstrate the coherent control of the dynamics of Mössbauer nuclei using X-ray light. To achieve this goal, we shape double-pulse sequences from given incident X-ray pulses with a tunable relative phase using the mechanical motion of a resonant absorber (Fig. 1a). In the experiment, we use the first (excitation) pulse of such sequences to induce a nuclear exciton in the target; that is, a single excitation coherently distributed over a large ensemble of nuclei. Controlling the relative phase of the second (control) pulse then enables us to switch the subsequent target dynamics between coherent enhanced excitation and coherent enhanced emission of the nuclear exciton (Fig. 1b). Using an event-based time- and energy-resolved detection scheme, we experimentally access the time-dependent magnitude and phase of the spatially averaged transition dipole moment induced in the target, and demonstrate the few-zeptosecond temporal stability of our phase-control scheme. We note that the coherent enhanced emission, reminiscent of stimulated emission, is possible here because of the coherent nature of the exciton, which enhances the coupling to the controlling light, whereas the observation of stimulated emission of incoherently excited nuclear states remains challenging even at present-day X-ray sources.

As a result of our experiment, we have developed a method of shaping single pulses delivered by state-of-the-art X-ray facilities into tunable double pulses, and demonstrate a temporal stability of the phase control on the few-zeptosecond timescale. Our results unlock coherent optical control for nuclei, and pave the way for nuclear Ramsey spectroscopy and spin-echo-like techniques, which should not only advance nuclear quantum optics, but also help to realize X-ray clocks and frequency standards. In the long term, we envision time-resolved studies of nuclear out-of-equilibrium dynamics, which is a long-standing challenge in Mössbauer science.

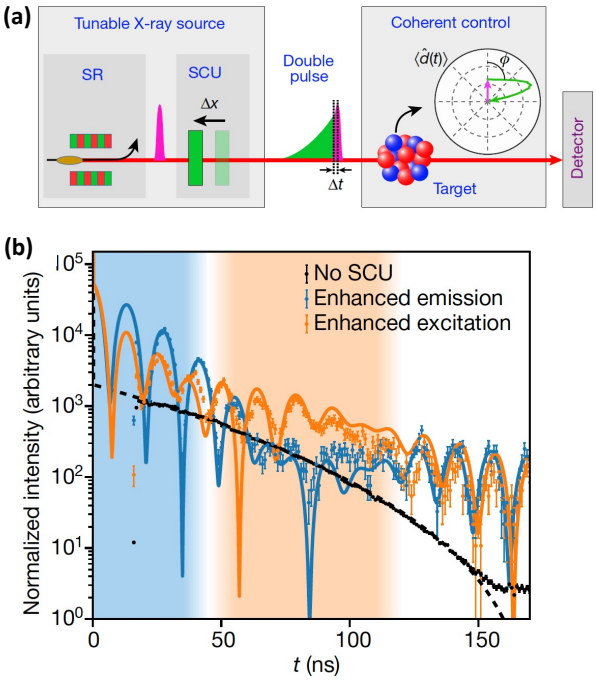

Figure 1: (a) A short synchrotron (SR) X-ray pulse is shaped into a double pulse using a resonant absorber acting as a delay stage, which we denote as the split-and-control unit (SCU). A fast displacement Δx of the SCU controls the relative phase ϕ between the two pulses corresponding to a relative delay Δt, thus forming a tunable X-ray double-pulse source. The double-pulses are used to coherently control the dynamics of the target nuclei. (b) Time-resolved intensities recorded in the forward direction for two different double-pulse sequences corresponding to coherent enhanced emission and enhanced excitation of the target nuclei.

We acknowledge a consolidator grant from the European Research Council (X-MuSiC-616783) and support by the DFG SFB 1225 (ISOQUANT)

References

[1] K. P. Heeg *et al.*, Nature **590**, 401 (2021).

High-resolution X-ray Spectroscopy with PolarX-EBIT at PETRA III

S. Bernitt[1,2,3,4], S. Kühn[3], R. Steinbrügge[5], M. Togawa[3], C. Shah[6], M. A. Leutenegger[6], J. Buck[7], M. Hoesch[5], Th. Stöhlker[1,2,4], and J. R. Crespo López-Urrutia[3]

[1]HI Jena, Fröbelstieg 3, 07743 Jena, Germany; [2]GSI Helmholtzzentrum, Planckstraße 1, 64291 Darmstadt, Germany; [3]MPI für Kernphysik, Saupfercheckweg 1, 69117 Heidelberg, Germany; [4]IOQ, Friedrich-Schiller-Universität, Max-Wien-Platz 1, 07743 Jena, Germany; [5]DESY, Notkestraße 85, 22607 Hamburg, Germany; [6]NASA/GSFC, 8800 Greenbelt Rd, Greenbelt, MD 20771, USA; [7]Christian-Albrechts-Universität, Leibnizstraße 11-19, 24098 Kiel, Germany

The compact electron beam ion trap PolarX-EBIT provides targets of trapped highly charged ions for UV and X-ray radiation at ultrabrillant synchrotron light sources, allowing studies of processes involving resonant excitation of ions by absorbtion of single photons. Such measurements can provide valuable data about atomic processes, relevant for X-ray astrophysics and fundamental atomic structure theory.

In PolarX-EBIT, a monoenergetic electron beam is used to get ions into high charge states by electron impact ionization. These ions are trapped by the electron beam and additional electrodes, and are overlapped with a synchrotron photon beam. The trap's compact structure, based on permanent magnets [1], and its unique off-axis electron gun facilitate novel experiments, in which the photon beam can pass the trap and is available for downstream setups, providing complementary data. Such experiments have been conducted at beamline P04 of the PETRA III synchrotron facility.

A decades long disagreement between experiment and theory regarding the oscillator-strength ratio of two $2p$–$3d$ transitions in Ne-like Fe^{16+}, commonly called 3C and 3D, has been one of the most investigated problems in X-ray astrophysics. While our own measurements with PolarX-EBIT just recently seemed to deepen this disagreement [2], improvements is the experiment setup and measurement schemes allowed us to increase spectral resolving power by a factor of 2.5 and signal-to-noise ratio by three orders of magnitude, which allowed us to identify hitherto unaccounted-for contributions to the measured line intensities [3]. Taking these into account, experiment and theory finally seem to agree. Additionally, it was possible to reconstruct the natural line widths of both lines from the measured line shapes. They also agree with theory within the experimental uncertainties.

In a new experiment at beamline P04 PolarX-EBIT provided few-electron ions of N, O, F, and Ne. Transitions in Li-like ions were resonantly excited, while transitions in H- and He-like ions, which can be calculated to sub-meV accuracy, served as energy references. The ASPHERE photoelectron spectrometer was recording energy spectra of photoelectrons from an Au target simultaneously with the fluorescence measurements (see figure 1), providing precise corrections for thermal drifts and nonlinearities in angular-encoder readouts. These were the dominant sources of systematic uncertainties in previous experiments, limiting the accuracy of absolute transition energy determinations. The combination of PolarX and ASPHERE has demonstrated the ability to overcome these limitations and to provide reliable energy calibrations with meV-level accuracy. Data analysis is still ongoing, expected to deliver benchmarks of QED calculations for Li-like systems, and future experiments with the setup are planned.

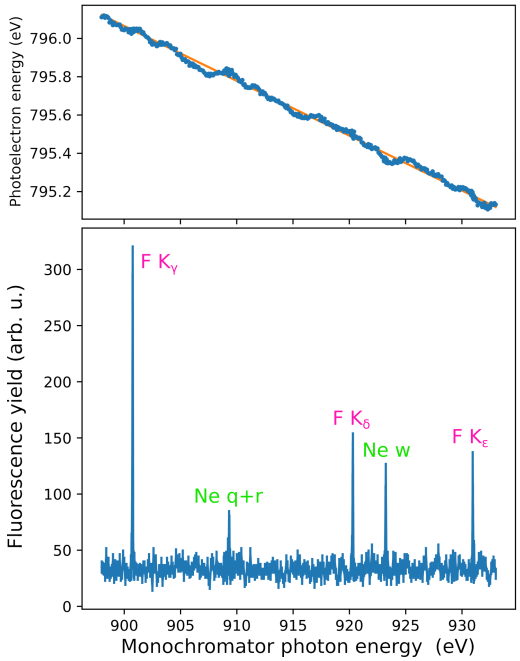

Figure 1: Resonantly excited fluorescence from few-electron ions of F and Ne (bottom), recorded simultaneously with photoelectrons from an Au target (top), which serve as precise energy reference, showing deviations of the actual photon energy from the requested one.

The authors acknowledge funding from MPG, DFG, NASA, and BMBF through project 05K13SJ2.

References

[1] P. Micke *et al.*, Rev. Sci. Instrum. **89**, 063109 (2018).

[2] S. Kühn *et al.*, Phys. Rev. Lett. **124**, 225001 (2020).

[3] S. Kühn *et al.*, `https://arxiv.org/abs/2201.09070` (2022).

Precision x-ray spectroscopy of U^{90+} using novel microcalorimeters

G. Weber*[1,2], S. Allgeier[4], S. Bernitt[1,2,3], A. Borovik[6], L. Duval[7], A. Fleischmann[4], M. Friedrich[4], O. Forstner[1,2,3], J. Glorius[2], A. Gumberidze[2], Ch. Hahn[1,2], D. Hengstler[4], M. O. Herdrich[1,2,3], P.-M. Hillenbrand[2], A. Kalinin[2], M. Kiffer[1,2,3], F. M. Kröger[1,2,3], M. Kubullek[3], P. Kuntz[4], M. Lestinsky[2], B. Löher[2], E. B. Menz[1,2,3], T. Over[1,2,3], N. Petridis[2], Ph. Pfäfflein[1,2,3], S. Ringleb[1,2,3], R. S. Sidhu[4], U. Spillmann[2], S. Trotsenko[1,2], A. Warczak[5], B. Zhu[1,2,3], C. Enss[4], and Th. Stöhlker[1,2,3]

[1]HI Jena; [2]GSI, Darmstadt; [3]IOQ, FSU Jena; [4]KIP, Heidelberg University; [5]Jagiellonian University, Krakow; [6]I. PI, Gießen University; [7]Sorbonne Université, Paris

Precision spectroscopy of x-ray transitions in few-electron, high-Z systems is an indispensable tool for the study of relativistic effects and bound-state quantum electrodynamics (QED) in the presence of strong electromagnetic fields. Such measurements are expected to significantly profit from the development of low-temperature calorimetric detectors, such as metallic magnetic microcalorimeters (MMC). Such detectors combine a high spectral resolution, similar to crystal spectrometers, with a broad bandwith acceptance that is comparable to semiconductor detectors. We report on their first application in a FAIR phase 0 experiment.

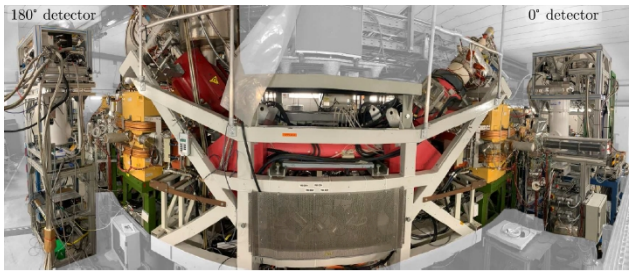

Figure 1: Photograph of the experimental setup at the electron cooler of CRYRING@ESR.

Within the spring 2021 beamtime block we studied x-ray emission from stored U^{91+} as a result of recombination between ions and electrons in the electron cooler section of CRYRING@ESR. We employed two novel maXs-100 detectors, which are optimized for photon energies of up to 100 keV [1]. The measurement was aimed at obtaining L → K transition energies with a precision of at least 1 eV to test second-order QED contributions in the regime of extreme field strengths. The experimental setup with the detectors being located at 0° and 180° view ports is depicted in Fig 1.

The ion beam was provided by the ESR with a kinetic energy of $10.255\,\mathrm{MeV\,u^{-1}}$ and typical intensities of 1×10^6 to 2×10^6 ions per injection. In CRYRING@ESR the beam was continuously electron-cooled at a voltage of $5634.5\,\mathrm{V}$ and an electron current of $30.5\,\mathrm{mA}$. The beam lifetime of 7 s to 8 s was determined in approximately equal proportions by charge exchange in the residual gas and RR in the electron cooler. As the preparation time of the beam in ESR was almost 60 s, there was a significant time gap from the moment when the beam intensity was almost gone in CRYRING to the next injection from ESR. This time window was used for taking calibration data from gamma reference sources, that were placed in front of the detectors in synchronization with the accelerator cycle.

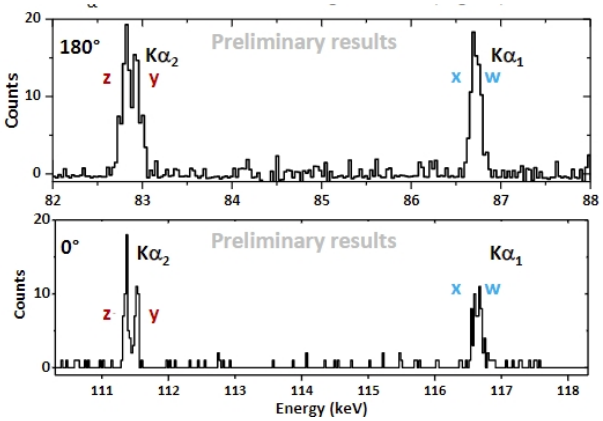

Figure 2: Preliminary spectral data of the L → K transitions in U^{90+}.

X-ray spectroscopy studies can often significantly benefit from the use of coincidence techniques, e. g. between photons and charge-changed projectile ions, to discriminate the photons of interest from unrelated radiative processes. In the present experiment we exploited for the first time the timing capabilities of MMC detectors in combination with the signals of a particle detector downstream from the electron cooler to suppress all photons that were not associated with a recombination event in the cooler.

Preliminary spectra of the L → K transitions in U^{90+} recorded at both observation angles are presented in Fig 2. The achieved spectral resolution is sufficient to resolve the splitting of the z and y lines (≈ 140 eV in the emitter system) for the first time in a high-Z system.

This work was conducted in the framework of the SPARC collaboration, experiment E138 of FAIR Phase-0 supported by GSI. We acknowledge support by the ERC under the European Union's Horizon 2020 research, by the innovation program (grants 824109 "EMP") as well as by ErUM FSP T05 - "Aufbau von APPA bei FAIR" (BMBF grants 05P19SJFAA and 05P19VHFA1).

References

[1] Ph. Pfäfflein *et al.*, submitted to Physica Scripta (2022).

*g.weber@hi-jena.gsi.de

High-Resolution Microcalorimeter Measurement of X-Ray Transitions in U^{90+} at CRYRING@ESR: Analysis of the Low-Energetic Region

F.M. Kröger*[1,2,3], S. Allgeier[4], Z. Andelkovic[3], S. Bernitt[1,2,3], A. Borovik[6], L. Duval[7], A. Fleischmann[4], O. Forstner[1,2,3], M. Friedrich[4], J. Glorius[3], A. Gumberidze[3], Ch. Hahn[2,3], F. Herfurth[3], D. Hengstler[4], M.O. Herdrich[1,2,3], P.-M. Hillenbrand[3], A. Kalinin[3], M. Kiffer[1,2,3], M. Kubullek[1], P. Kuntz[4], M. Lestinsky[3], B. Löher[3], E.B. Menz[1,2,3], T. Over[1,2,3], N. Petridis[3], Ph. Pfäfflein[1,2,3], S. Ringleb[1,2,3], R.S. Sidhu[4], U. Spillmann[3], S. Trotsenko[2,3], A. Warczak[5], G. Weber[2,3], B. Zhu[1,2,3], C. Enss[4], and Th. Stöhlker[1,2,3]

[1]IOQ, FSU Jena, Germany; [2]HI Jena, Germany; [3]GSI, Darmstadt, Germany; [4]KIP, Heidelberg Univ., Germany; [5]Jagiellonian Univ., Krakow, Poland; [6]I.PI, Gießen Univ., Germany; [7]LKB, Univ. Paris Sorbonne, Paris, France

By applying novel low-temperature metallic magnetic microcalorimeter (MMC) detectors at the electron cooler of CRYRING@ESR we obtained high-resolution x-ray spectra of transitions in U^{90+}. As this type of detector combines high resolution with broad bandwidth acceptance, it allows us to conduct the Doppler correction of the observed line positions intrinsically from the measured spectra itself by utilizing characteristic transitions with well-known line positions. Here we present a proof-of-principle of this newly available approach, which may be of critical importance for upcoming high-precision x-ray spectroscopy experiments at storage rings.

Precision x-ray spectroscopy of fast moving ions in storage rings requires an exact knowledge of the projectile velocity to transform the Doppler-shifted photon energy from the laboratory to the emitter system. Usually, this quantity is derived from the electron cooler settings, i.e. the applied voltage, to which non-trivial corrections for the space charge of the electron beam, as well as for the contact potential between cathode and collector have to be applied. Alternatively, projectile transitions with well-known energies could be employed to determine the Doppler shift, provided that such lines are observed with sufficient spectral precision. However, up to now the used detectors were either limited in their resolution (e.g. semiconductor detectors), or their spectral acceptance was too narrow to simultaneously detect the lines of interest and the aforementioned reference transitions (e.g. crystal spectrometers).

In our experiment 2021 were applied for the first time novel MMC detectors at an electron cooler of a storage ring, namely the recently commissioned CRYRING@ESR at GSI. Here we studied the x-ray emission associated with radiative recombination between cooler electrons and stored U^{91+} ions. The two 'maXs' MMC detectors used [1] achieved a resolution below 100 eV FWHM at 100 keV incident photon energy, comparable with the resolution of the FOCAL transmission crystal spectrometer [2]. In addition, the MMC detectors have a broad spectral acceptance down to a few keV. This enabled us to use selected 'M $\rightarrow$ L' transitions between states with well-known binding energies for a determination of the Doppler shift, and consequently ion beam velocity. This is illustrated in figure 1, showing the low-energetic region where these transitions in the L-shells were recorded at 0° with respect to the ion beam axis. A fit of the spectrum with the ion beam velocity as a free parameter yields $\beta = 0.14676(9)$, while from the settings of the electron cooler one would expect $\beta = 0.14696(3)$. Note that these are all preliminary values as data analysis is still ongoing.

This research was conducted in the framework of the SPARC collaboration, experiment E138 of FAIR Phase-0 supported by GSI. We acknowledge support by the ERC under the European Union's Horizon 2020 research, by the innovation program (grants 824109 'EMP') as well as by ErUM FSP T05 - "Aufbau von APPA bei FAIR" (BMBF grants 05P19SJFAA and 05P19VHFA1).

[1] D. Hengstler *et al.*, Phys. Scr. **T166**, 014054 (2015).
[2] T. Gassner *et al.*, New J. Phys. **20**, 073033 (2018).

*felix.kroeger@uni-jena.de

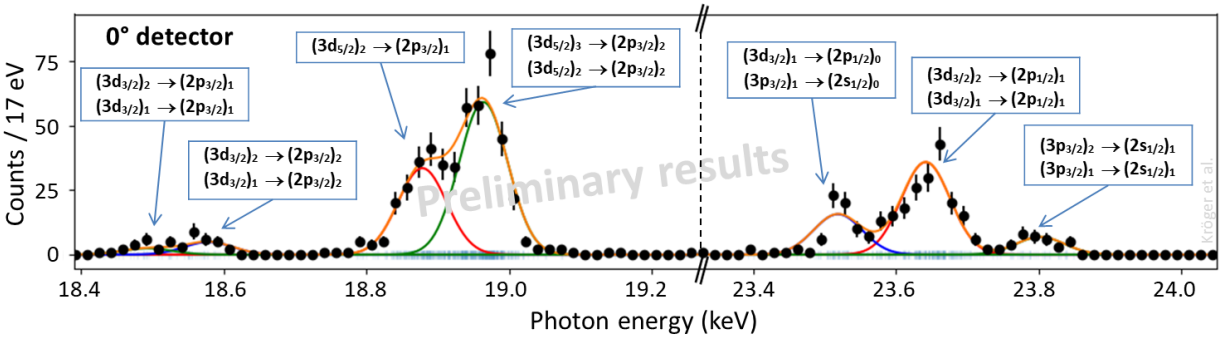

Figure 1: Preliminary fit of the data measured with the 0° detector.

Characteristic X-Ray Transitions in Hydrogen-like Lead Ions Recorded at the CRYRING@ESR Electron Cooler

B. Zhu [*1,2,3], A. Gumberidze[2], T. Over[1,2,3], U. Spillmann[2], G. Weber[1,2], and Th. Stöhlker[1,2,3]

[1]HI Jena, Fröbelstieg 3, D-07743 Jena, Germany; [2]GSI Darmstadt, Planckstraße 1, D-64291 Darmstadt, Germany; [3]IOQ, FSU Jena, Max-Wien-Platz 1, D-07743 Jena, Germany

X-ray emission as a result of Radiative Recombination (RR) at threshold energies in the electron cooler of CRYRING@ESR was studied for decelerated bare lead ions at 10 MeV/u beam energy. The recorded spectra are dominated by characteristic transitions in Pb^{81+}, namely the Lyman, Balmer and Paschen series, as a result of decay cascades from high-n states that are preferentially populated by the RR process. We present a comparison between our rigorous theoretical model and the experimental data.

Radiative Recombination (RR), the time-reversal of photoionization, can be considered as one of the most elementary and fundamental atomic processes and is the major recombination process occurring for electron beams and bare ions. In particular, it is of utmost importance for plasma population kinetics, ionization equilibrium, and radiative power losses. In this process, a free electron recombines into a bound state of an ion via the emission of a photon, carrying away the difference in energy between the initial (continuum) and final (bound) electronic states and satisfying momentum conservation.

Most of RR experiments were performed at electron cooler devices of storage rings for the low velocity regime. Recently, the first x-ray spectroscopy production runs of hydrogen-like lead was successfully conducted at the electron cooler of CRYRING@ESR [1], shipped from the Manne Siegbahn Laboratory in Stockholm to Darmstadt as a Swedish in-kind contribution to FAIR. By utilizing dedicated x-ray detection chambers installed at 0° and 180° observation geometry, it enabled us for the first time to observe the full x-ray emission pattern in a wide energy range, spanning the Paschen series up to the K-RR transition without any line distortion effects.

For the analysis of radiative cascade processes in current electron-ion recombination experiment, an elaborate theoretical model is established following the technique as discussed in detail in Ref. [2]. At a high nuclear charge of the Pb nucleus, transitions from L-, M- and N-shell to the ground state of Pb^{81+} ions are fast, even the M1 magnetic dipole transitions have to be considered as prompt. Likewise, the L-RR populating the excited L-shell sublevels in Pb^{81+} should represent the initial line intensities of Lyman-$\alpha_{1,2}$ transitions as prompt contributions. Also, the population of M-RR contributes to the initial Balmer series and Lyman-β line via fast decay at the time interval of $\Delta t \lesssim 10^{-13}$ s. The results are displayed by the shaded areas in Fig. 1 whereby the unshaded areas are identified as the delayed cascade feeding to the observed characteristic projectile x-rays. To gain further insight, we present in Table 1 the contributions from highly excited states and subsequent feeding transitions to the formation of pronounced Lyman-α_1 and Lyman-α_2 lines observed, as the transitions into different j-states of the L-shell are clearly resolved.

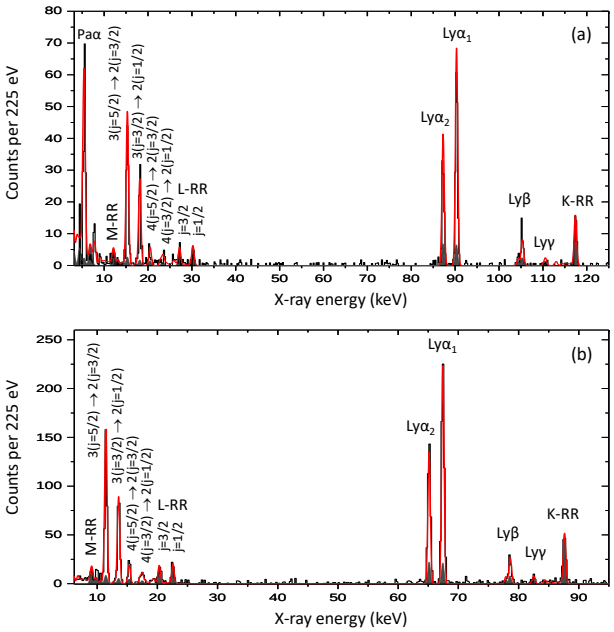

Figure 1: X-ray spectra measured (black lines) at observation angles of (a) 0° and (b) 180° by two Ge(i) detectors in coincidence with down-charged Pb^{81+} ions. The red lines give the result of time integrated spectra based on a cascade calculation. The shaded areas represent the contribution from prompt transitions assuming within the time interval of $\Delta t \lesssim 10^{-13}$ s.

Table 1: Contribution from feeding cascades to the formation of Lyman-α_1 and Lyman-α_2 lines. Uncertainties shown here are due to counting statistics whereas systematic uncertainties are neglected.

	0 deg	180 deg	Theory
Lyα_1	93.6% ± 12.0%	94.0% ± 5.5%	93.9%
Lyα_2	86.3% ± 15.6%	87.4% ± 6.5%	86.8%

The authors acknowledge funding from ErUM-FSP APPA (BMBF n° 05P19SJFAA and n° 05P19RGFA1).

References

[1] M. Lestinsky *et al.*, Eur. Phys. J.: Spec. Top. **225**, 797 (2016).

[2] B. Zhu *et al.*, arXiv: 2201.06977 (2022).

*b.zhu@hi-jena.gsi.de

Coherent control of collective nuclear quantum states via transient magnons

Lars Bocklage[1,2], Jakob Gollwitzer[1], Cornelius Strohm[1], Christian F. Adolff[1,2], Kai Schlage[1], Ilya Sergeev[1], Olaf Leupold[1], Hans-Christian Wille[1], Guido Meier[3,2], and Ralf Röhlsberger[1,2,4,5]

[1]DESY, Hamburg, Germany; [2]The Hamburg Centre for Ultrafast Imaging, Hamburg, Germany; [3]Max-Planck Institute for the Structure and Dynamics of Matter, Hamburg, Germany; [4]Friedrich-Schiller-Universität Jena, Germany; [5]Helmholtz Institute Jena, Jena, Germany

Quantum systems lie at the heart of many future technologies. In order to use quantum systems in practical applications, it is necessary to control and manipulate them with great precision. In the experiment reported here we have succeeded in controlling and measuring a quantum system with hitherto unattainable temporal precision in the regime of hard X-rays. We have managed to control and detect oscillations of a collectively excited nuclear state via the gamma radiation emitted, to within an accuracy of a few zeptoseconds. This method makes use of fundamental quasiparticle excitations that occur within a solid. Precise control of this kind is important when building novel quantum sensors, to establish extreme time standards or to detect minute changes of physical parameters.

The quantum system in our experiment was an ensemble of ^{57}Fe nuclei embedded in a solid. The solid was a thin magnetic film, just a few nanometres thick, containing the iron atoms. We used short pulses of synchrotron radiation to collectively excite the 14.4 keV nuclear resonance in the ^{57}Fe nuclei. The extremely rapid oscillation of the nuclear transition dipole moment, with a period of just 287 zeptoseconds, causes the atomic nuclei to emit gamma radiation or X-rays. The time evolution of the collective nuclear state can be controlled by short microwave pulses which cause the entire magnetic system of the solid to oscillate. The collective magnetic excitation, known as magnon, has a period on the order of nanoseconds which is much slower than the oscillation period of the atomic nucleus. This transient magnon has a pronounced effect on the temporal evolution of the collectively excited nuclear state: It induces a well defined phase shift of the emitted X-rays. Thus, after the magnon has decayed, the emitted radiation displays a brief time delay, see Fig. 1. This delay can be controlled very precisely and has been measured in our experiment with zeptosecond accuracy.

For the detection of such small temporal shifts, we used a heterodyne detection scheme that employed two hyperfine-split nuclear resonances of the ^{57}Fe, which emit gamma radiation of different frequencies, leading to a temporal beat node in the measured superposition signal. One of these two resonances is only slightly affected by the transient magnon, thus serving as a reference frequency. Therefore, if the transient magnon shifts the oscillation phase of the other resonance by a few zeptoseconds, so that the beat node in the measured signal shifts by a few nanoseconds [1]. This means that zeptosecond temporal shifts of the X-ray carrier frequency can be deduced from nanosecond shifts of the measured beat nodes in the heterodyne signal.

This illustrates that magnons enable a tremendous flexibility in controlling nuclear quantum systems via adjusting the duration and strength of the exciting microwave pulse. Due to the intrinsic relative stability of the detection scheme, temporal shifts can be measured to an accuracy of less than 50 yoctoseconds.

Our experiments mark a first step towards using this novel method of controlling an embedded quantum system by exciting the surrounding solid. Apart from magnon excitation, a number of other solid-state excitations exist, such as oscillations of the crystal lattice or the electron system which could be excited, e.g., by impulsive optical stimuli.

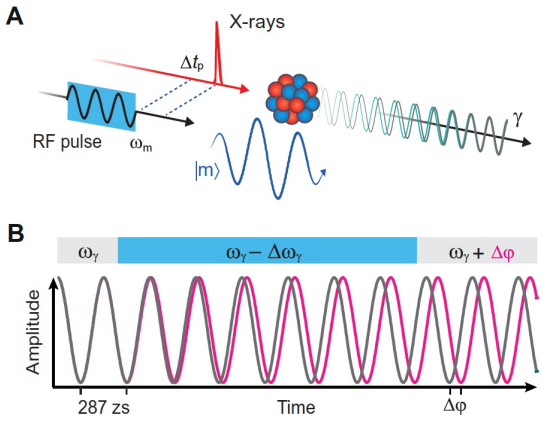

Figure 1: A) A ^{57}Fe nucleus in a ferromagnetic film is hit by a 14.4 keV X-ray pulse to excite two of its hyperfine-split nuclear resonances. A microwave pulse with delay Δt_p excites a magnon $|m\rangle$ which leads to a neV energy shift of one of the resonance lines. B) During the presence of the magnon indicated by the blue bar, a phase shift $\Delta\varphi$ developes that prevails even if the magnon is gone.

Financial support of the DFG via Cluster of excellence "The Hamburg Centre for Ultrafast Imaging" (EXC 1074, project ID 194651731) is gratefully acknowledged

References

[1] L. Bocklage *et al.*, Science Advances **7**, eabc3991(2021).

Progress Report of the Negative Ions Laser Photodetachment Project

Oliver Forstner*[1,2], Vadim Gadelshin[3], Kurt Stiebing[4], and Klaus Wendt[3]

[1]Helmholtz Institute Jena; [2]Institut für Optik und Quantenelektronik, Friedrich–Schiller–Universität Jena; [3]Institut für Physik, Johannes Gutenberg–Universität Mainz; [4]Institut für Kernphysik, Goethe–Universität Frankfurt

Within the LISEL@DREAMS project laser photodetachment of negative ions will be used to suppress isobars in high sensitive mass spectrometry. To this end an ion beam cooler for negative ions is being constructed at the University of Jena. The required tunable Ti:sapphire laser is built by the University of Mainz and currently installed at the low–energy electrostatic storage ring at the Goethe–University Frankfurt.

Laser photodetachment of negative ions can be used as an element sensitive method for the suppression of isobars. By careful tuning of the laser wavelength it is possible to neutralise the unwanted isobars while keeping the ions of interest unaffected. This method was first demonstrated successfully at the VERA AMS facility in Vienna [1]. In the BMBF funded joint project 05K2019 – LISELatDREAMS a laser photodetachment setup will be constructed at Jena for use at the DREAMS (Dresden AMS) facility at HZDR. Despite significant delays due to the SARS-CoV-2 situation the construction of the LISEL setup is progressing. Recently, the ion beam cooler was finalised and the high voltage cage was installed. High voltage tests up to the nominal voltage of 35 kV have been conducted successfully. The rf part of the cooler has been machined at the University workshop and is going to be installed in the first quarter of 2022. Fig. 1 show the current status of the LISEL setup in the dedicated laboratory at the University of Jena.

The project partner of the University of Mainz is in charge of providing the laser for LISEL. For the LISEL project a tunable Ti:Sapphire laser system has been developed by the project partner at the University of Mainz. Pumped by a 10 kHz frequency doubled Nd:YAG laser the Ti:sapphire laser produces laser radiation in the range of 690 to 960 nm with a maximum output of 3 W. The system has been installed at the low–energy electrostatic storage ring FLSR at the Goethe–University Frankfurt to perform laser photodetachment studies on stored atomic and molecular ions [2]. Fig. 2 on top shows the Ti:sapphire laser. The bottom part shows the laser hut on the right together with the laser tube (grey tube on the wall) guiding the laser to the interaction section in the ring. The laser neutralises negative ions in the ring if the photon energy is above the electron affinity of the respective ion. The neutral particles continue straight onto a position sensitive silicon strip detector. First experiments will take place in the beginning of 2022.

Figure 1: LISEL cooler setup with high voltage cage.

Figure 2: Top: LISEL Laser setup. Bottom: FLSR setup

This project is supported by funding from the German Ministry of Science BMBF, joint project 05K2019 – LISELatDREAMS.

References

[1] O. Forstner et al., The ILIAS project for selective isobar suppression by laser photodetachment, Nucl. Instr. and Meth. **B 361**, 217-221 (2015).

[2] O. Forstner et al., Opportunities for negative ions studies at the Frankfurt Low–energy Storage Ring (FLSR), Hyp. Int. **241**, 53 (2020).

*o.forstner@hi-jena.gsi.de

Connecting Fano interference and the Jaynes-Cummings model in cavity magnonics

Jakob Gollwitzer[1], Lars Bocklage[1,2], Ralf Röhlsberger[1,2,3,4], and Guido Meier[5,2]

[1]DESY, Hamburg, Germany; [2]The Hamburg Centre for Ultrafast Imaging, Hamburg, Germany; [3]Friedrich-Schiller-Universität Jena, Germany; [4]Helmholtz Institute Jena, Jena, Germany; [5]Max-Planck Institute for the Structure and Dynamics of Matter, Hamburg, Germany

We show that Fano interference can be realized in a macroscopic microwave cavity coupled to a spin ensemble at room temperature. A generalized Fano interference emerges from the photon–magnon interaction at low cooperativity. In this regime, the reflectivity of the cavity approximates the scattering cross-section derived from the Fano-Anderson model. Although asymmetric lineshapes in this system are often associated with the Fano formalism, we show that whilst Fano interference is actually present, an exact Fano form cannot be achieved from the linear Jaynes-Cummings (JC) model. In the Fano model an additional contribution arises, which is attributed to decoherence in other systems, and in this case is due to the resonant nature of the photonic mode. The formalism is experimentally verified and accounts for the asymmetric lineshapes arising from the interaction between magnon and photon channels. As the magnon–photon coupling strength is increased, these channels merge into hybridized magnon–photon modes and the generalized Fano interference picture breaks down. Our results are universally applicable to systems underlying the linearized Jaynes-Cummings Hamiltonian at low cooperativity.

Resonances in atoms, molecules, or matter reflect many of their properties. Coupling of resonances to the environment or to other resonances leads to emerging phenomena in a large variety of systems. Spurred by the possibility of coherent photon–magnon interaction and associated potential for quantum information processing, the field of cavity electromagnonics has experienced enormous growth in the past decade. A single photonic mode can be strongly coupled to a single magnon mode. Classical coherence effects reproduce the behavior predicted by quantum optical models both at cryogenic and at room temperatures. Strong magnon–photon coupling via the so-called cavity-magnon polariton has been vital to reaching photon detection via electrical spin pumping probes, dark mode memories, and magnon coupling to a qubit. Invoking the description of the polariton as a classical interaction between an electromagnetic wave and a matter polarization, strong magnon–photon coupling may be understood as the hybridization of the magnonic and photonic modes.

We have shown that a generalized Fano form emerges from the linearized JC model and verify this experimentally in a microwave cavity coupled to the Kittel mode of a permalloy film in the Purcell regime, see Fig. 1. Our model connects the microscopic parameters of the linearized JC model to the phenomenological parameters of the generalized Fano form [1]. In this way we uncover magnon–photon coupling at low cooperativity as interference between scattering of a background cavity channel and the magnon channel. These two channels have well-defined phases in accordance with the Fano interference picture. Remarkably, the physics of Fano interference becomes apparent even though the system consists of two coupled modes with finite linewidths. This opens a new view on the connection between the Fano-Anderson and the linearized JC models at low cooperativities.

Depending on the coupling strength, the magnon–photon coupling can be understood in terms of either Fano interference or mode hybridization. Finally, the linear JC model describes many types of systems in which a cavity mode interacts weakly with a matter-based harmonic resonance. The wide applicability of the linear JC model hence makes the results presented here important to many areas of physics including hard X-ray quantum optics, atomic interactions with optical cavities, and cavity electromagnonics.

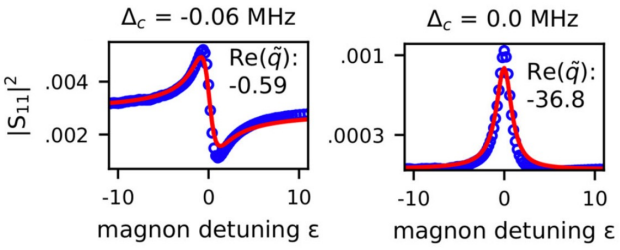

Figure 1: Measured cavity reflectivity of the interaction between a microwave cavity mode and a magnon mode for two different cavity detunings Δ_c. The data show the Purcell effect for a 10 nm thick permalloy film inserted into the cavity. The Kittel mode of the permalloy film couples to the cavity photon, which is manifested as a distortion in the cavity resonance. Red lines are fits of the lineshapes according to our theory [1] .

Financial support of the DFG via Cluster of excellence "The Hamburg Centre for Ultrafast Imaging" (EXC 1074, project ID 194651731) is gratefully acknowledged.

References

[1] J. Gollwitzer, L. Bocklage, R. Röhlsberger, and G. Meier, NPJ Quantum Information **7**, 114 (2021).

Measurement of the 2s-Lamb Shift of Lithium-Like Uranium Utilizing a Novel Metallic-Magnetic Calorimeter Based Spectrometer

M. O. Herdrich*[1,2,3], D. Hengstler[4], J. Geist[4], C. Schötz[4], M. Keller[4], P. Schneider[4], A. Fleischmann[4], C. Enss[4], T. Gassner[1,2], G. Weber[1,2], and Th. Stöhlker[1,2,3]

[1]HI Jena, Jena; [2]GSI, Darmstadt; [3]IOQ, Jena; [4]KIP, Heidelberg

We present a measurement of the 2s-Lamb shift of lithium-like uranium utilizing metallic-magnetic calorimeter detectors for high precision X-ray spectroscopy. The experiment was performed at the internal gas target of the ESR of GSI and highlights the advantages of the novel detector technology.

With metallic-magnetic calorimeters – like the maXs-series detectors developed in cooperation with the group of C. Enss in Heidelberg – a novel type of energy dispersive photon detectors for high precision X-ray spectroscopy experiments is available within the SPARC collaboration. Their unique working principle gives rise to several advantages compared to conventional spectrometer detectors. They combine the broad spectral bandwidth of semiconductor detectors with a high resolution power up to $\mathrm{E}/\Delta\mathrm{E} > 6000$ [1] comparable to crystal spectrometers. In the past years several high precision spectroscopy experiments were performed at storage rings of GSI exploiting the exceptional performance of several different maXs-series detectors.

During an experiment carried out at the internal target of the ESR, X-ray photons stemming from the collision of U^{89+} ions at $75.91\,\mathrm{MeV/u}$ with a gas-jet of N_2 [2] were observed by a maXs-30 [3] detector located at the 90°-port. The recorded spectrum (fig. 1) contains different lines from transitions into and within the L-shell of two different charge states of uranium. Subsequent relaxations resulting from the impact excitation of U^{89+} ions and non-radiative electron capture into excited states of U^{88+} ions were identified. The absolute calibration of the spectrum was performed using a ^{241}Am γ-source. Due to the fact, that at the time of recording a proper temperature correction procedure for the detector was still in development, a comparably low combined energy resolution of $36.7\,\mathrm{eV}$ (at $< 26\,\mathrm{keV}$) was achieved. Sudden shifts of the operation point of the used SQUID amplifiers led to the observation of two satellites besides each main peak. This was taken into account by using a modified fitting model. The Doppler-correction was performed by assuming that the L-α and L-β transition energies for U^{89+} and U^{88+} are sufficiently well known. A linear regression between the measured peak energies and theoretical values (provided by P. Indelicato, p.c.) was performed to determine the Doppler-shift. For the calculation of the 2s-Lamb shift of U^{89+}, initially, the assumption was made that the binding energies of the electron states $E(3d_{3/2}) \approx E(3p_{3/2})$ are degenerated as they are sufficiently far away from the nucleus. This allowed us to compare the transition energy of

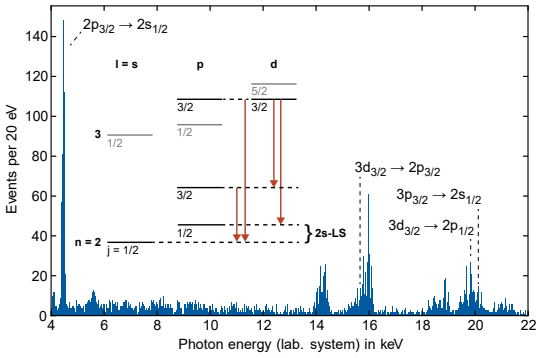

Figure 1: The spectrum containing X-ray photons from the collision of U^{89+} ions at $75.91\,\mathrm{MeV/u}$ on a N_2-target. A level scheme of U^{89+} is included and relevant transitions are indicated.

$3p_{3/2} \rightarrow 2s_{1/2}$ and $3d_{3/2} \rightarrow 2p_{1/2}$ which yields an energy difference between the $2p_{1/2} \rightarrow 2s_{1/2}$ of $273.5(51)\,\mathrm{eV}$ (the provided error is purely statistical, all results are preliminary). The slight discrepancy to literature values of theory $280.76(14)\,\mathrm{eV}$ [4] and previous experimental findings $280.645(15)\,\mathrm{eV}$ [5] might be explained by the unresolved actual non-degeneracy of the $3d_{3/2}$ and $3p_{3/2}$ states. In order to obtain the energy difference between the $2s_{1/2}$ and $2p_{1/2}$ we also made use of the prominent $\Delta n = 0$ transition clearly visible in the same spectrum: $E(2p_{1/2}) - E(2s_{1/2}) = \Delta E(2p_{3/2} \rightarrow 2s_{1/2}) - (\Delta E(3d_{3/2} \rightarrow 2p_{1/2}) - \Delta E(3d_{3/2} \rightarrow 2p_{3/2})) = 276.4(74)\,\mathrm{eV}$.

Despite the overall low event rates a determination of the 2s-Lamb shift of U^{89+} was possible demonstrating the advantage of using high resolution MMC detectors with their broad spectral bandwidth. This allowed for the simultaneous observation of highly resolved lines from multiple transitions enabled the determination of the Doppler-shift from within the spectrum, thus eliminating systematic uncertainties arsing from the experiment setup. It also made alternative approaches to the examined physics case possible.

We acknowledge financial support by the European Union and the federal state of Thuringia via Thüringer Aufbaubank within the ESF project (2018 FGR 0080).

References

[1] J. Geist, Dissertation, Heidelberg (2020).

[2] P.-M. Hillenbrand *et al.*, Phys. Rev. A **104**, 012809 (2021).

[3] D. Hengstler, Dissertation, Heidelberg (2017).

[4] V. A. Yerokhin *et al.*, Phys. Rev. Lett. **97**, 0253004 (2006).

[5] P. Beiersdorfer *et al.*, Phys. Rev. Lett. **95**, 0233003 (2005).

*m.o.herdrich@hi-jena.gsi.de

Photon Background in Potential Light-Light Scattering Experiment

Pooyan Khademi*[1], Leonard Doyle[2], Peter Hilz[1], Jörg Schreiber[2], and Matt Zepf[1]

[1]Helmholtz Institute Jena, Fröbelstieg 3, 07743 Jena, Germany; [2]Ludwig-Maximilians-Universität München, Fakultät für Physik, Fakultät für Physik, 85748 Garching, Germany.

The advent of high power, short pulsed lasers sheds light on the experimental realization of quantum vacuum effects, such as photon-photon scattering. The first challenge is the detection of few signal photons from a vast number of driving photons, $\mathcal{O}(10^{20})$. Here we represent the experimental results to quantify the background level.

The quantum vacuum is filled with fluctuations of virtual electron-positron pairs. Extremely strong electro-magnetic fields, e.g. high power ultrashort optical lasers, can couple to the virtual pairs which can then exhibit unique effects, inconceivable in classical vacuum, such as photon-photon scattering [1]. To produce photon-photon scattering signal, one collides two high intensity laser pulses in vacuum. This signal, due to its faint nature and presence of numerous driving beams photons, is challenging to detect. Also scattered photons from the rest gas particles and surfaces in the experimental chamber overwhelm the signal. Therefore one has to identify light from these noise sources i.e. background (BG), to obtain the quantum vacuum signature. To quantify the BG level, we used the JETi-200 Ti:sapphire laser at Helmholtz Institute Jena. An $800\,\mathrm{nm}$, $24\,\mathrm{fs}$ laser pulse with $175\,\mathrm{mJ}$ energy was focused to $2.2\,\mu\mathrm{m}$ with an $\mathrm{f}/1.5$ off-axis parabolic (OAP) mirror in vacuum with $34\,\%$ of energy inside the $1/\mathrm{e}^2$ radius, resulting in the peak intensity of $5 \times 10^{19}\,\mathrm{W\,cm^{-2}}$. An ICCD gated camera with $16\,\%$ quantum efficiency at $800\,\mathrm{nm}$ and $1\,\mathrm{ns}$ gate-time detected the photons through an imaging system with $20\times$ magnification, perpendicular to the beam axis at the focus, with collection efficiency of $11\,\%$ for $800\,\mathrm{nm}$. The detection was timed to the arrival of main pulse at focus. Fig1 presents detected BG photons. The main pulse follows a pedestal with enough energy to ionize the atoms in focal region (ROI). At the ROI, electrons scatter the main pulse, Thomson scattering (TS), into the imaging cone. The pressure dependence was measured with air at high pressures and He at low pressures, for horizontal and vertical polarization. Normal to the laser polarisation, TS is suppressed and a constant BG of multiple diffuse scattering is visible, Fig1. Due to $1\,\mathrm{ns}$ gate window of the camera, objects at $\leq 30\,\mathrm{cm}$ scatter light in the collection cone. The main contributors are OAP and $\lambda/2$-plate (only for V-pol), with 42 and 19 photons per $1\,\mathrm{J}$ per $100\,\mu\mathrm{m}^2$ ROI, respectively. Suppressing the BG from all the sources requires better spatio-temporal filtering of ROI. Although static scattering can be mitigated with cleverer geometry and shorter temporal-gated detection ($\sim$Rayleigh range), the TS depends on particle numbers in ROI. For an intense laser such as one used here, the ponderomotive cavitation can clear the ROI by repelling the electrons outside the laser axis. This effect was both measured and simulated, Fig 2. In conclusion, up scaling the results of this study to $10^3\times$ higher pulse energy suggests BG photons from TS are likely manageable, with utilizing the ponderomotive cavitation. Furthermore, better optical surfaces quality, avoiding direct beam paths to collection cone and shorter gating times (ns to fs), can improve reduction of static scatter by 5-6 orders of magnitude [2], providing the basis for the future experiments.

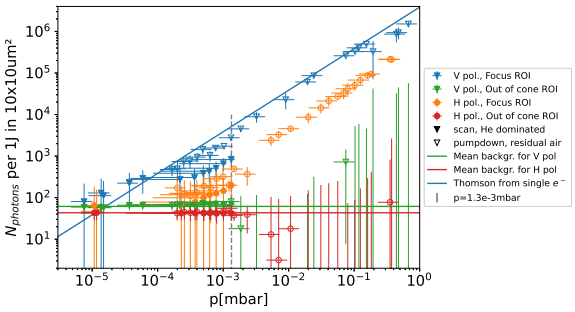

Figure 1: Pressure dependence of rest gas scattered signal for both polarization inside the focal ROI and area-equivalent for the out-of-cone ROI. Diffuse reflection becomes the dominant at lower pressures. Scaled to 1 J [2].

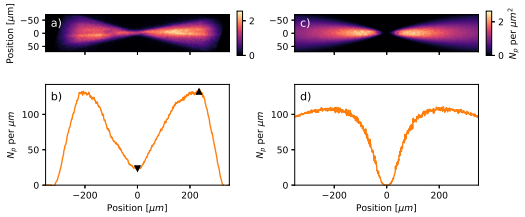

Figure 2: **a)** Photons per shot N_p per $\mu\mathrm{m}^2$, averaged over 242 shots at $\approx 1.3 \times 10^{-3}\,\mathrm{mbar}$ with $175\,\mathrm{mJ}$ pulse energy. **b)** Image a) integrated along vertical extent ($\pm 70\,\mu\mathrm{m}$), number of photons per $\mu\mathrm{m}$ slice along the optical axis. Here, the reduction factor between minimum in focus and maximum peak is $5.6\times$ (▲). **c)** Simulation with a Gaussian pulse, **d)** Image c) integrated along vertical extent [2].

Funded by DFG under Grant No. 416702141 within the Research Unit FOR2783/1.

References

[1] F. Karbstein *et al.*, Phys. Rev. D **97**, 036022 (2018).

[2] L. Doyle *et al.*, New J. Phys. **24**, 025003 (2022).

*p.khademi@hi-jena.gsi.de

Time-resolved measurement of laser-induced dissociation of the dihydrogen cation with a two-color pump-probe scheme

Maximilian Kubullek[2], Bo Ying[1,2], Matthias Kübel[1,2], Philipp Wustelt[1,2], A. Max Sayler[1,2,3], Thomas Stöhlker[1,2], and Gerhard G. Paulus*[1,2]

[1]Helmholtz Institute Jena, Fröbelstieg 3, 07743 Jena, Germany; [2]Institute of Optics and Quantum Electronics, Friedrich Schiller University Jena, D-07743 Jena, Germany; [3]Benedictine College, Atchison, KS, USA

We present time-resolved measurements of the photodissociation dynamics in the simplest molecular system, the dihydrogen cation H_2^+, utilizing a pump-probe technique involving two different colors. In the experiment, H_2^+ ions from our ion beam source are dissociated by a first laser pulse, and the ensuing dynamics are probed by a second pulse. The measured delay-dependent energy distribution of the fragments allow us to follow the breakage of the simplest molecule on the femtosecond time scale. This capability paves the way to investigate the temporal dynamics of hitherto unexplored molecular ion targets.

Observing and tracking the formation and breakage of molecular bonds on the femtosecond time scale is the central goal of femtochemistry [1] and molecular physics. This is often achieved using ultrashort laser pulses, typically inducing ionization of the neutral precursor. In the present work, we report a time-resolved measurement of photodissociation of an ionic precursor molecule, namely H_2^+, avoiding ionization in the pump step.

Our experiment relies on a pulse pair at the fundamental wavelength of 1030 nm and its second harmonic at 515 nm, with a variable delay. The pulses are focused into a molecular ion beam target and the resulting fragments are detected using coincidence 3D momentum spectroscopy. The experimental scheme displayed in Figure 1 allows us to probe the dissociation process in real time.

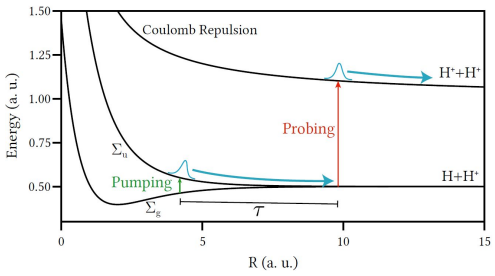

Figure 1: Schematic of the pump-probe experiment. The first pulse starts the dissociation (green arrow). After a variable time interval τ, the second pulse ionizes the dissociating molecule (red arrow).

The experimental results are displayed in Figure 2. Shown is the kinetic energy release (KER) distribution of the protonic fragments as a function of pump-probe delay. The delay dependence of the low-energy part of the signal arises from the interaction of the molecule with both laser pulses, as described above. The measured kinetic energy release (KER) depends on the internuclear distance at which the molecule interacted with the probe pulse, hence probing the dissociation dynamics. From the recorded data, we conclude that the nuclear wave packet detaches from the bound part within less than 50 fs.

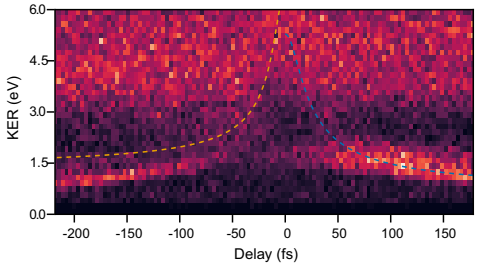

Figure 2: Measured kinetic energy release (KER) spectra for varying delay between the two laser pulses. The dashed lines show the classical estimate of the kinetic energy after coulomb explosion. On the left side of the diagram, dissociation is triggered by 515 nm and ionization by 1030 nm, on the right side vice versa.

Interestingly, our experiment allows us to observe the difference in the ionization dynamics after photodissociation by either 1030 nm or 515 nm light. In the former case (1030 nm, positive delays), the asymptotic dissociation energy is well described (dashed blue line) by a simple classical model in which we assume that dissociation starts at precisely the internuclear distance where the energy difference between the Σ_g and Σ_u states corresponds to the photon energy. In the case of 515 nm photodissociation, however, the measurement does not agree with the simple predictions (dashed green line). Further quantum mechanical simulations are on the way to clarify this disagreement.

Future experiments will aim at investigation of more complex ionic targets such as the argon dimer Ar_2^+ or exotic targets provided by our liquid metal ion source, such as the gold dimer Au_2^+ [2].

The authors acknowledge funding from the Deutsche Forschungsgemeinschaft (Priority program 1840, Quantum Dynamics in Tailored Intense Fields).

References

[1] A. H. Zewail, J. Phys. Chem. A. **104**, 5660-5694 (2000)

[2] B. Ying *et al.*, J. Phys. B. **54**, 174002 (2021)

*gerhard.paulus@uni-jena.de

Laser-induced ionization with liquid metal ion sources and two-color sculpted laser fields

F. Machalett*[1,2], B. Ying[1,2], P. Wustelt[1,2], L. Bischoff[3], N. Klingner[3], W. Pilz[3], M. Kübel[1,2], A. M. Sayler[1,2,4], Th. Stöhlker[1,2], and G. G. Paulus[1,2]

[1]Helmholtz Institute Jena, Fröbelstieg 3, D-07743 Jena, Germany; [2]Institute of Optics and Quantum Electronics, Friedrich Schiller University Jena, D-07743 Jena, Germany; [3]Helmholtz-Zentrum Dresden-Rossendorf, Bautzner Landstraße 400, D-01328 Dresden, Germany; [4]Benedictine College, Atchison, KS, USA

We have successfully employed high-brightness liquid metal ion sources (LMIS) for the investigation of the interaction of metal and metalloid ions with strong field laser beams. The gold and silicon ions, generated in the LMIS by electrostatic field ionization, can be further ionized up to Au^{11+} and Si^{4+} with Thales laser (1 kHz) at intensities of up to $4{\cdot}10^{16}$ W/cm^2. Furthermore, we employed the fiber laser with 100 kHz to manipulate the recoil momenta with subcycle resolution.

With ionic laser targets it is possible to investigate the light-matter interaction of fundamental systems, such as He^+, H_2^+ [1]. Also molecules that only arise in the ion source, can be investigated, e.g. HeH^+ [2]. In this work we generated ion beam targets for the investigation of strong-field laser interactions with metal and metalloid ions. We adapted a high-brightness liquid metal ion source (LMIS), originally applied in focused ion beam systems [3], to an ion system for 3D coincidence momentum spectroscopy (Fig. 1). Using an $E \times B$ filter in the beamline, several different ion species could be detected: Si^+, Si^{2+}, Au^+, Au^{2+}, Au_2^+, Au_3^+ and Au_3^{2+}. Monoatomic and noble metal molecular ions can be used to carry out studies on the ultrafast laser-induced fragmentation and ionization.

Moreover, we investigated the ultrafast laser-induced ionization resulting in higher charge states after the multiple ionization of Au^+ and Si^{2+} ions. Laser intensities of $4{\cdot}10^{16}$ W/cm^2 allow the tenfold ionization of the Au^+-ions and triple ionization of Si^{2+}-ions.

To control the single and double ionization processes on the attosecond time scale we applied two-color sculpted laser fields. The momentum distributions depend strongly on the relative phase of the two-color laser field. Figure 2 shows the relative phase-dependent momentum distribution, both measured and simulated, of Au^{2+} and Au^{3+} ions after single and double ionization of Au^+.

The results show that LMIS with alloys as source materials can provide a broad range of ion species for experiments of attosecond physics.

The authors acknowledge funding from the Deutsche Forschungsgemeinschaft (Priority program 1840, Quantum Dynamics in Tailored Intense Fields). We thank the IBC at Helmholtz-Zentrum Dresden-Rossendorf e.V. for support at the experiments.

*frank.machalett@uni-jena.de

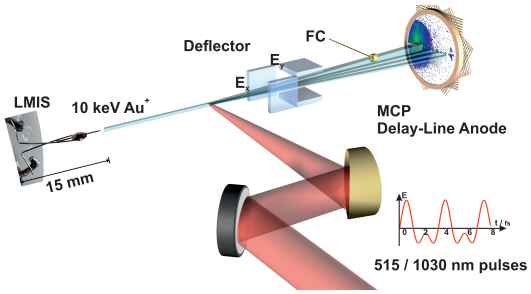

Figure 1: Fs-pulses are focused onto a 10 keV ion beam of Au^+ produced from the liquid metal ion source (LMIS), blocked by a Faraday Cup (FC). The higher charge states of Au^{q+} are detected by a combination of a multichannel plate (MCP) and a delay-line detector. Electrostatic fields perpendicular to the ion beam allow the charge state separation after laser-induced ionization [4]. On the right the asymmetric two-color electric field is shown.

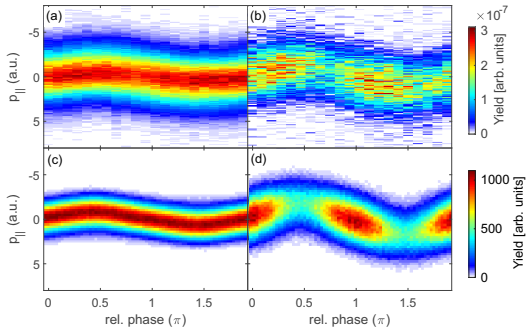

Figure 2: Momentum distribution in laser polarization direction for ionization of Au^+ ions with a laser peak intensity of $4{\cdot}10^{14}$ W/cm^2, and a pulse duration of 40 fs. Relative phase-dependent momentum distribution $p_{\parallel}$ measured (a) of Au^{2+} produced by single ionization and (b) for Au^{3+} produced by double ionization, (c) and (d) are the respective corresponding simulated distributions with a peak intensity of $2.5{\cdot}10^{14}$ W/cm^2 and a pulse duration of 40 fs [4].

References

[1] T. Rathje, *et al.*, Phys. Rev. Lett. **11**, 093002 (2013)

[2] P. Wustelt, *et al.*, Phys. Rev. Lett. **121**, 073203 (2018)

[3] F. Machalett, P. Seidel, Focused Ion Beams and Some Selected Applications, EAP, Wiley (2019)

[4] B. Ying, *et al.*, J. Phys. B: At. Mol. Opt. Phys. **54**, (2021)

Quantum Optical Phenomena in Nuclear Resonant Scattering

Ralf Röhlsberger[1,2,3] and Jörg Evers[4]

[1]DESY, Hamburg, Germany; [2]Helmholtz Institute Jena, Germany; [3]Friedrich-Schiller-Universität Jena, Germany; [4]Max-Planck-Institut für Kernphysik, Heidelberg, Germany

With the advent of high-brilliance, accelerator-driven light sources such as modern synchrotron radiation sources or x-ray lasers, it has become possible to extend quantum optical concepts into the x-ray regime. Owing to the availability of single photon x-ray detectors with quantum efficiencies close to unity and photon-number resolving capabilities, fundamental phenomena of quantum optics can now also be studied at Angstrom wavelengths. A key role in the emerging field of x-ray quantum optics is taken by the nuclear resonances of Mössbauer isotopes. Their narrow resonance bandwidth facilitates high-precision studies of fundamental aspects of the light-matter interaction at X-ray wavelengths.

A very accurate tuning of the interaction of X-rays with matter is facilitated via a controlled placement of Mössbauer nuclei in planar thin-film waveguides that act as cavities for X-rays. A decisive aspect in contrast to conventional forward scattering is that the cavity geometry facilitates the excitation of cooperative radiative eigenstates of the embedded nuclei, as elaborated in a recent review article [1]. The multiple interaction of real and virtual photons with a nuclear ensemble in a cavity leads to a superradiant enhancement of the resonant emission and a strong radiative level shift, known as collective Lamb shift [2].

Meanwhile, thin-film x-ray cavities and multilayers have evolved into an enabling technology for nuclear quantum optics [1]. The radiative coupling of such ensembles in the cavity field can be employed to generate atomic coherences between different nuclear levels, resulting in phenomena including electromagnetically induced transparency (see Fig. 2), spontaneously generated coherences, Fano resonances and others. Enhancing the interaction strength between nuclei in photonic structures like superlattices and coupled cavities facilitates to reach the regime of collective strong coupling of light and matter where phenomena like normal mode splitting and Rabi oscillations appear. These developments establish Mössbauer nuclei as a promising platform to study quantum optical effects at x-ray energies. In turn, these effects bear potential to advance the instrumentation and applications of Mössbauer science as a whole.

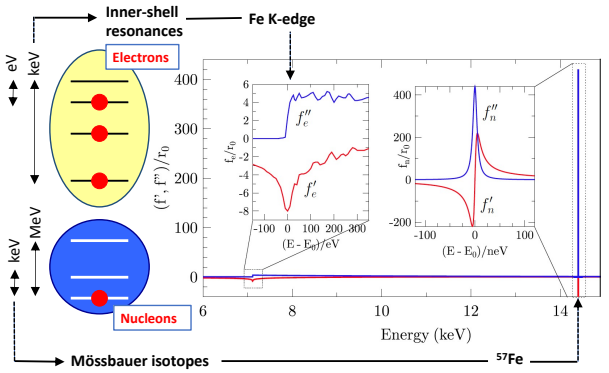

Figure 1: Left: Bound states of electrons or nucleons in atoms are the origin of electromagnetic resonances in matter with resonance energies from eV to several 100 keV. Right: Real and imaginary parts of the atomic scattering amplitudes f' and f'', respectively, in the vicinities of the Fe K-edge at 7.1 keV and the 14.4 keV nuclear resonance of ^{57}Fe. Please note their largely different energy ranges and spectral shapes. While the Fe K-edge absorption proceeds from a bound state into the continuum, the 14.4 keV transition can be considered as an almost ideal two-level system connecting two discrete nuclear levels.

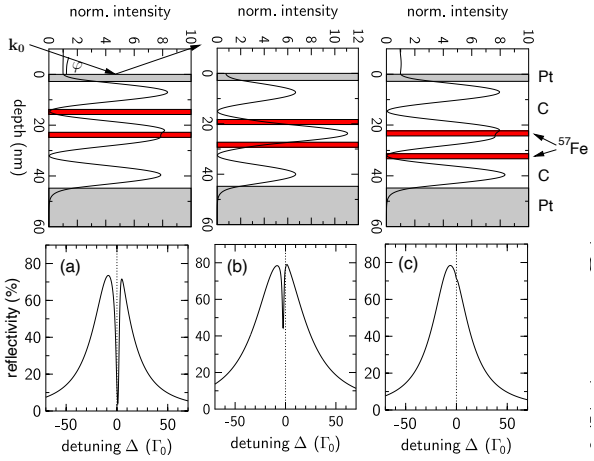

Figure 2: Top row: Geometry of a planar X-ray cavity containing two thin layers of ^{57}Fe (red) shown together with the normalized field intensity in the third-order cavity mode (solid line). Bottom row: Superradiantly broadened energy spectra of the cavity reflectivity around the nuclear resonance. The radiative coupling of the two nuclear ensembles depends on their position relative to the cavity wavefield, leading to a strong EIT transparency dip in (a) that gradually vanishes with change to configuration (c) [3].

References

[1] R. Röhlsberger and J. Evers, in: Y. Yoshida and G. Langouche (eds.), Modern Mössbauer Spectroscopy, Topics in Applied Physics **137**, Springer Nature Singapore (2021).

[2] R. Röhlsberger *et al.*, Science **328**, 1248 (2010)

[3] R. Röhlsberger *et al.*, Nature **482**, 199 (2012)

High-repetition rate optical pump-nuclear resonance probe experiments identify transient molecular vibrations after photoexcitation of a spin crossover material

S. Sadashivaiah*[1,2], J. A. Wolny[2], L. Scherthan[2], K. Jenni[2], A. Omlor[2], C. S. Müller[2], I. Sergueev[3], M. Herlitschke[3], O. Leupold[3], H. -C. Wille[3], R. Röhlsberger[1,3,4], and V. Schünemann[2]

[1]Helmholtz-Institut Jena, Fröbelstieg 3, 07743 Jena, Germany; [2]Technische Universität Kaiserslautern, 67663 Kaiserslautern, Germany; [3]Deutsches Elektronen Synchrotron, 22607 Hamburg, Germany; [4]Friedrich-Schiller-Universität Jena, 07743 Jena, Germany

Phonon modes play a vital role in the cooperative phenomenon of light-induced spin transitions in spin crossover (SCO) molecular complexes. Although the cooperative vibrations, which occur over several hundreds of picoseconds to nanoseconds after photoexcitation, are understood to play a crucial role in this phase transition, their precise identification had been elusive. Therefore, we have performed a novel optical laser pump-nuclear resonance probe experiment to determine changes in the Fe-projected vibrational density of states (pDOS) during the first few nanoseconds after laser excitation of the mononuclear Fe(II) SCO complex [Fe(PM-BiA)$_2$(NCS)$_2$]. By simulating these changes using density functional theory calculations, we identify of transient inter- and intramolecular vibrational modes activated by the light-induced spin transition.

The quest to make ever smaller and faster memory devices drives the need to understand switching of the physical state in molecular systems such as Fe^{II}-based metal-organic complexes, also called spin crossover (SCO) complexes. Various stimuli such as short laser pulses can cause a reversible switching of the Fe atom between the low spin (S=0) and the high spin (S=2) states in these complexes. Due to the small difference of energies between the two states, the dynamics of the switching transition depend on the accompanying the change in entropy of the system. The entropy changes are also caused by changes of the metal-ligand bond lengths corresponding to changes of the electron configuration during the transition. Thus, the light-driven spin transition is a cooperative phenomenon, where the switching of a few molecules can trigger the switching of a large number of molecules. Phonons play a crucial role in the cooperativity between molecules. Thus, identification of the exact inter- and intramolecular vibrational modes in the laser excited transient state, which stabilises the final state, is crucial to the understanding the light-driven SCO transition. This identification, however, has been elusive because of limitations of available techniques.

We report here on a novel optical laser pump - nuclear inelastic scattering (NIS) probe experiment using the ^{57}Fe nucleus to directly probe the vibrations involving the iron atoms, which occur within nanoseconds after photoexcitation of the SCO complex [Fe(PM-BiA)$_2$(NCS)$_2$] [1]. Synchrotron-based NIS can be regarded as an extension of the conventional, energy-resolved Mössbauer spectroscopy to energies of molecular vibrations. It is a highly sensitive technique because the metal-ligand bond lengths, and thus the vibrational modes, are specific to the spin states of the SCO complexes. It provides the full Fe-projected phonon density of states (pDOS) in a solid.

In this experiment, performed at the synchrotron source PETRA III at DESY in Hamburg, we measured the pDOS of the ground and laser-excited transient states (see Figure 1). By simulating the individual pDOS and their difference using density functional theory, we could identify the specific vibrational modes active in the transient state.

This technique can be applied to any optically excitable bulk or nanostructured solid containing the Mössbauer-active nucleus. Free electron X-ray laser sources allow a significant improvement of the time resolution of the pump-probe measurement. The experiment reported here already indicates ways for laser based coherent control of nuclear excitonic states through hyperfine interactions.

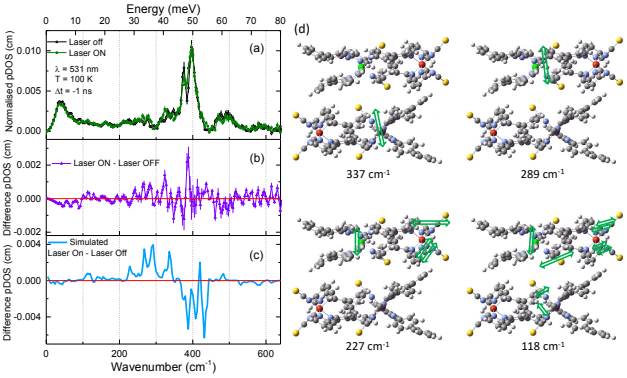

Figure 1: (a) pDOS obtained from the pump-probe experiments. (b) Difference of the ground and excited states. (c) DFT simulation of the difference. (d) The transient vibrations (green arrows) in a unit cell at various wavenumbers.

The authors acknowledge funding from the Deutsche Forschungsgemeinschaft (TRR173 268565370), the Bundesministerium für Bildung und Forschung (05K16UKA) and the Allianz für Hochleistungsrechnen Rheinland-Pfalz (TUK-SPINPLUSVIB).

References

[1] S. Sadashivaiah *et al.*, J. Phys. Chem. Lett. **12**, 3240 (2021).

*s.sadashivaiah@gsi.de

Pair Production Yield at the FOR2783/E3 Experiment at CALA

F. Salgado*[1,2], K. Grafenstein[3], D. Seipt[1], S. Karsch[3], and M. Zepf[1,2]

[1]Helmholtz-Institut Jena, Germany; [2]Institute of Optics and Quantum Electronics, Friedrich-Schiller-Universität Jena, Germany; [3]Ludwig-Maximilians-Universität München, Germany

The advent of ultra-intense lasers and GeV electron beams generated by plasma-based accelerators are ideal to experimentally test strong-field QED phenomena that remain untested in the laboratory. The collision of γ-ray photons generated from the interaction of GeV electron beams and highly-intense laser beams produces field strengths above the Schwinger limit (1.3×10^{18} V/m) in the center-of-momentum (COM) frame [1], where the probability of converting a γ-ray photon to a pair becomes high. Here, we report about 80 pairs/h generated by the nonlinear Breit-Wheeler process at the upcoming FOR2783 experiment that will be realized at the Centre for Advanced Laser Applications (CALA) for 10 pC bunch charge.

The FOR2783/E3 project is an all-optical experiment to probe electron-positron pairs, generated by photon-laser collisions for the first time - the so called nonlinear Breit-Wheeler process. High-energy γ-ray photons are produced through the interaction of monoenergetic 2.5 GeV laser accelerated electron beams with a bunch charge of 10 pC, and FWHM divergence angle of $\theta_e = 0.5\,\mathrm{mrad}$ with a thin $50\,\mu\mathrm{m}$-thick tungsten converter target. The bremsstrahlung γ-photons propagate towards the interaction point (IP) - 60 cm away from its generation, and collide with a laser beam of intensity $9.5 \times 10^{21}\,\mathrm{W\,cm^{-2}}$, which corresponds to an $a_0 \approx 66$, and pulse duration of 30 fs focused in a spot size of approximately $\omega_0 \approx 2\,\mu\mathrm{m}$. For details on the FOR2783/E3 experiment at CALA, please see Ref. [2].

The pair creation probability from the photon-laser collision is given by [1]

$$\frac{\mathrm{d}P}{\mathrm{d}t} = -\frac{\alpha m_e^2 \chi_\gamma}{16\omega_\gamma} \int_{z_0}^{\infty} \mathrm{d}z \, \frac{8u+1}{\sqrt{z}\sqrt{u^3(u-1)}} \, \mathrm{Ai}'(z)\,, \qquad (1)$$

with $z_0 = (4/\chi_\gamma)^{2/3}$ and $u = (z/z_0)^{3/2}$. The parameter χ_γ is the photon quantum nonlinear parameter, and it indicates the relation between laser and Schwinger fields in the COM frame. The laser-photon interaction regime is defined by χ_γ and a_0. In the case of the FOR2783/E3 experiment, pair production is achieved in the non-perturbative, quasi-static strong-field regime where $a_0 \gg 1$ and $\chi_\gamma \gg 1$.

Using the experimental parameters above, the number of expected pairs can be calculated using the following relation: $N_{pairs} = \Phi_{gamma} \cdot A_{laser} \cdot \theta_{div} \cdot N_{cycles} \cdot P$, where Φ_{gamma} is the γ-photon flux of 1.7 photons/μm^2 provided in Ref. [2], A_{laser} is the collider laser focal spot area, N_{cycles} is the number of laser cycles and P is the average pair production probability per cycle calculated using equation (1). The parameter θ_{div} represents the yield reduction due to the overlap between the large γ-ray spot and electron beam such that $\theta_{div} = \theta_\gamma^2/(\theta_e^2 + \theta_\gamma^2) \approx 0.14$ for $\theta_\gamma = 1/\gamma \approx 204\,\mu\mathrm{rad}$.

Figure 1 shows the pair creation probability rate for different laser intensities and converter target thickness. The design point of the experiment is chosen for a primary electron bunch of 2.5 GeV and 10 pC charge, tungsten converter target of $50\,\mu\mathrm{m}$ thickness which reduces significantly the background noise level at the detectors [2], and collider laser with $a_0 = 66$. A total of 0.22 pairs per shot which corresponds to about 80 pairs/h is expected at the design point for a laser repetition rate of 0.1 Hz.

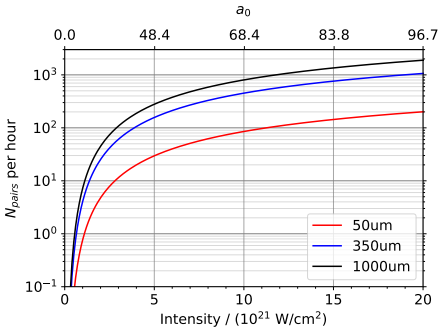

Figure 1: Pair creation rate per hour for different intensities (at constant laser spot size) and converter thickness (λ = 800 nm, $w_0 \approx 2\,\mu\mathrm{m}$, 30 fs, 2.5 GeV monoenergetic electron beam energy with 0.5 mrad FWHM divergence). A pair rate of 80 pairs/h is expected at the experiment design point for 10 pC bunches and laser repetition rate of 0.1 Hz.

In conclusion, pair creation through the nonlinear Breit-Wheeler process at the FOR2783/E3 experiment is achievable for the first time with LWFA electron beams at a PW-facility. By introducing plasma-lens to focus the electron beam, the pair yield can be increased up to an order of magnitude. The FOR2783/E3 experiment therefore paves the way for the first observation of pairs from photon-laser collisions in all-optical setups.

This work has been funded by the Deutsche Forschungsgemeinschaft (DFG) under Project No. 416708866 within the Research Unit FOR2783/1.

References

[1] V. I. Ritus, J. Sov. Laser Res. **6**, 5 (1985).

[2] F. C. Salgado *et al.*, New J. Phys. **23**, 105002 (2021).

*felipe.salgado@uni-jena.de

HILITE - updates on ion trap and ion transport line

S. Ringleb[1], M. Kiffer[1], N. Stallkamp[2], B. Arndt[3], S. Kumar[4], M. Vogel[2], W. Quint[2,5], Th. Stöhlker[1,2,6], and G. G. Paulus[1,6]

[1]Intitut für Optik und Quantenelektronik, 07743 Jena, Germany; [2]GSI Helmholtzzentrum für Schwerionenforschung, 64291 Darmstadt, Germany; [3]Goethe Universität Frankfurt, 60323 Frankfurt, Germany ; [4]Inter-University Accelerator Centre, 110067 New Delhi, India; [5]Physikalisches Institut, Ruprecht Karls-Universität Heidelberg, 69120 Heidelberg, Germany; [6]Helmholtzinstitut Jena, Fröbelstieg 3, 07743 Jena, Germany

The goal of the High-Intensity Laser-Ion-Trap Experiment (HILITE) is to investigate the interaction of stored highly-charged ions with high-energy or high-intensity radiation. Based on the results from our beamtime at FLASH in 2020, we have updated the electrode configuration which comprises a harmonic potential as well as small apertures to protect the interaction region from ambient residual gas.

The HILITE (High-Intensity Laser Ion-Trap Experiment) is intended to prepare well-defined ion targets for laser-interaction experiments with laser pulses of high photon energies or high laser intensities. The setup is designed in a transportable fashion, so it can be combined with different lasers systems at different laser facilities. In early 2020 we have connected the setup for the first time with the FLASH laser in Hamburg successfully. Unfortunately, we have not been able to form a rigid ion cloud due to high residual gas pressure of unknown origin. In order to protect the interaction region of our trap from residual gas from the surrounding setup or the laser beamline, we have updated the setup significantly. The new main features are the new aperture electrodes which have a free inner diameter of only $4\,\mathrm{mm}$. To allow strong laser focussing also the trap length was decreased to $66\,\mathrm{mm}$. A photo of the assembled trap is shown in figure 1.

In recent investigations, we have found the ion energy distribution of captured ions from an external source is about $20\,\mathrm{eV/q}$ which results in a widely distributed axial frequency of the stored ions. In consequence, efficient ion cooling will last for several minutes up to an hour. That is why, the new trap is equipped with a set of correction electrodes which are used to created a harmonic electric potential. We have simulated the expected frequency width in detail and found that with the new setup the frequency width is less than 1% of the zero-energy frequency. This is essential for efficient ion cooling and will allow for a cooling time of the order of one minute.

The ions for the laser experiments are delivered by an Electron-beam ion trap (EBIT). In order to decouple the laser path from the ion path, the ions are deflected by an electrostatic ion-beam deflector (see figure 2). The outer electrode of the deflector has a hole with a free diameter of $10\,\mathrm{mm}$ to achieve full transparency of the setup for the laser beam. Since the ions are guided perpendicularly to the stray field of the magnet, they experience a deflection off the experiment axis. This deflection is compensated by two four-fold segmented electrostatic ion lenses (Sikler lenses) at both the entrance and the exit of the ion beam deflector. This device is in operation reliably and is tested in detail.

For the year 2022 we prepared for laser-ion experiments at the Jena high-power laser system JETi200.

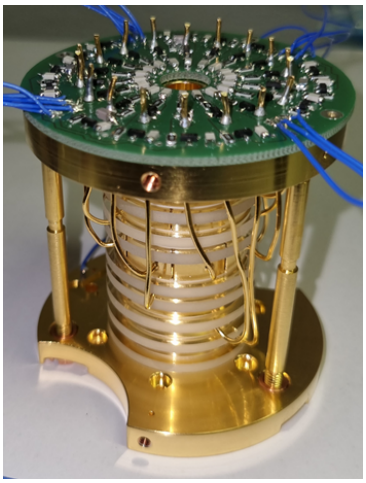

Figure 1: Photo of the new HILITE Penning trap. The Trap consists of nine electrodes. The low-pass filters are placed on one endplate.

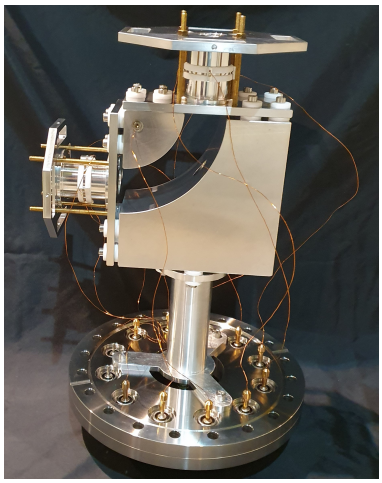

Figure 2: In-house produced electrostatic ion-beam deflector. To compensate the deflection by the magnetic stray field, segmented einzellenses (Sikler lenses) are used.

Cryogenic Current Comparator running at CRYRING@ESR

V. Tympel*[1,2], D. Haider[2], T. Sieber[2], M. Schwickert[2], Th. Stöhlker[1,2,3], and F. Schmidl[3]

[1]Helmholtz Institute Jena, Fröbelstieg 3, 07743 Jena; [2]GSI Darmstadt, Planckstraße 1; [3]University Jena, Max-Wien Platz 1

Cryogenic Current Comparator (CCC) is a non-destructive beam, easy to calibrate current measuring system for the nA range. The first CCC with FAIR-compatible dimensions (GSI-Nb-CCC-XD with 250 mm inner sensor diameter) ran in its newly designed beam cryostat. In order to adapt to currents in the µA range, it was necessary to specifically dampen the in-put circuit to avoid SQUID slew-rate overtaxing. SPICE simulations and cryo experiments at the Cryo Detector Lab in Jena were undertaken to compromise between frequency response, current noise and implementation possibilities on site.

The high linear current or magnetic field sensitivity of the CCCs is realized by superconducting quantum interference devices (SQUIDs) in Flux Locked Loop (FLL) mode. The FLL mode linearizes the periodic SQUID function by holding it in a set point. As a result, the feedback signal be-comes the actual measured value. The slew rate (here ultimately ampere per second) of the system defines how fast changes at the input may be without leaving the set point and incorrect measurements occur.

At the CRYRING@ESR, measurements are made in the nA and µA ranges. For the larger currents, however, a retrofit with a low pass filter in front of the SQUID had to be carried out. With the inductor L of a second, unused calibration winding of the pickup coil and a resistor R, an RL low pass was realized. In the run-up, spice simulations of current noise (Fig. 1) and frequency response (Fig. 2) with $RL(C)$ combinations took place, which were checked with cryogenic measurements in the Cryo Detector Lab Jena.

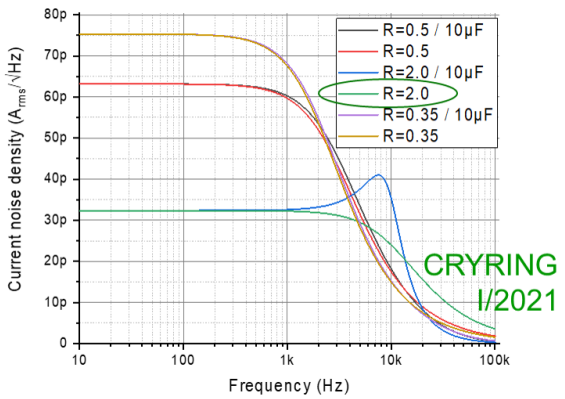

Figure 1: SPICE current noise simulation of the Nb-CCC-XD with $RL(C)$ pre-SQUID low pass filter @ 4 Kelvin.

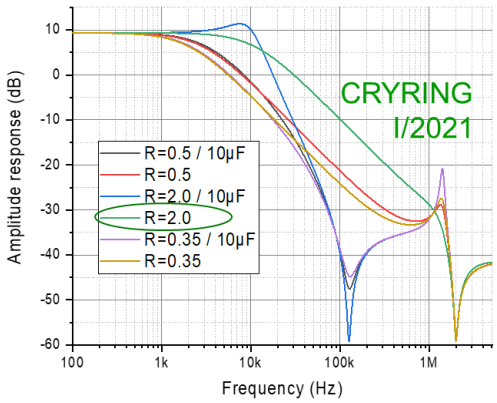

Figure 2: SPICE frequency response simulation of the Nb-CCC-XD with $RL(C)$ pre-SQUID low pass filter.

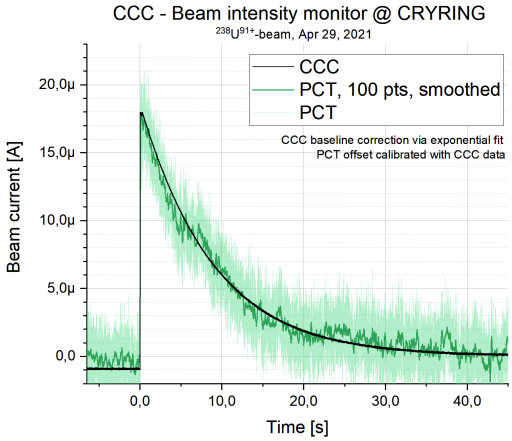

Figure 3: µ-Amp beam current measurements, CCC (black) compared to Parametric Current Transformer (green).

As a compromise, a 10 kHz low pass with $R = 2\,\Omega$ at $L = 80$ µH was realized on the cold side. The beam current measurements showed that it is thus possible to measure in the µA range (Fig. 3) [1]. For 2022, an upgrade of the SQUID cartridge is planned, with a second SQUID extending the dynamic range so that measurements can be made in nA and µA range without modifications.

The authors acknowledge funding from BMBF, project numbers 05P18SJRB1 and 05P121SJRB1.

References

[1] D. Haider *et al.*, DOI:10.18429/JACoW-IBIC2021-WEOB02

* v.tympel@hi-jena.gsi.de

Exploitation of timing capabilities of magnetic metallic microcalorimeters

Ph. Pfäfflein*[1,2,3], S. Allgeier[4], S. Bernitt[1,2,3], A. Fleischmann[4], M. Friedrich[4], Ch. Hahn[1,2,3], D. Hengstler[4], M. O. Herdrich[1,2,3], A. Kalinin[2], F. M. Kröger[1,2,3], P. Kuntz[4], M. Lestinsky[2], B. Löher[2], E. B. Menz[1,2,3], T. Over[1,2,3], U. Spillmann[2], G. Weber[1,2], B. Zhu[1,2,3], Ch. Enss[4,5], and Th. Stöhlker[1,2,3]

[1]HI Jena; [2]GSI, Darmstadt; [3]IOQ, FSU Jena; [4]KIP, Heidelberg University; [5]KIT, Karlsruhe

Within the spring 2021 beamtime block at GSI two metallic magnetic calorimeter detectors (MMCs), developed within SPARC, have been used at the electron cooler of CRYRING@ESR. These novel x-ray detectors combine a high spectral resolution typical for crystal spectrometers with the broad spectral acceptance commonly found in semiconductor detectors [1, 2]. Using a new readout system which was fully integrated into the GSI data acquisition infrastructure it was possible to exploit the time resolution of the detectors for the first time. This enables setting of coincidence conditions between x-rays and charge-changed ions to suppress background radiation.

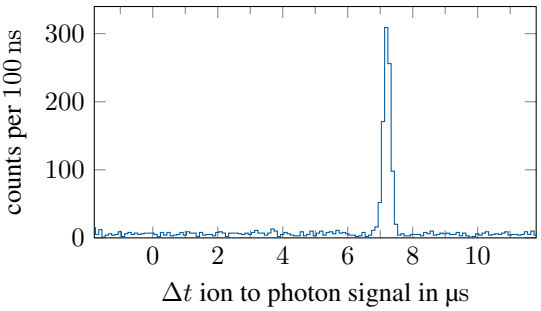

Figure 1: Difference in arrival time of photons at the MMC detector and corresponding hits on the particle detector. The peak is caused by the fixed time relation between photons which are emitted by radiative recombination of stored ions with the cooler electrons, and the detection of the respective ions by the particle detector.

X-ray spectroscopy studies can often benefit from the use of coincidence techniques to discriminate the photons of interest from unrelated radiative processes. In ion storage rings, when the photon emission is accompanied by a change in the projectile charge, this can be achieved by combining the signals of a particle detector with the time information from the photon detectors. With conventional semiconductor detectors this is a well established technique. However, to the best of our knowledge the extraction of time information from the pulses of MMC detectors has never been demonstrated before. In the present experiment, U^{91+} ions were stored in CRYRING@ESR. Their photon emission as a result of recombination inside the electron cooler was recorded by the MMC detectors in combination with counting the down-charged ions using a particle detector. The observed time-of-flight spectrum can be found in figure 1. A coincidence peak of less then 400 ns width is visible at around 7 µs.

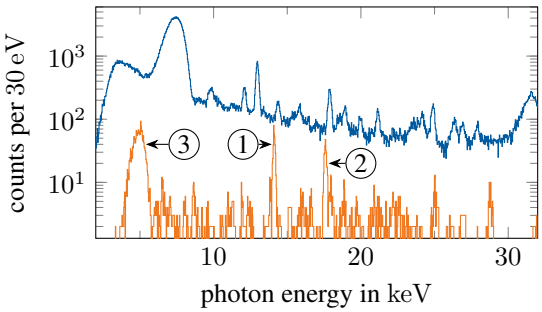

Figure 2: X-ray spectra recorded by a MMC detector at the electron cooler of CRYRING@ESR demonstrating the feasibility of coincidence measurements with MMC-based microcalorimeters. The spectrum containing all photons from the accelerator (blue) is compared to the coincident spectrum (orange). The marked peaks correspond to the $[1s_{1/2}, 3d_{5/2}] \rightarrow [1s_{1/2}, 2p_{3/2}]$ (1) and $[1s_{1/2}, 3d_{3/2}] \rightarrow [1s_{1/2}, 2p_{1/2}]$ (2) transitions, respectively; (3) arises from bremsstrahlung.

The effect of applying a coincidence condition is depicted in figure 2. The entire spectrum recorded from the electron cooler and including background is shown in blue. Filtering only those events that can be associated with a charge exchanged ion, i.e. a hit on the particle detector, results in the orange spectrum demonstrating a massive background reduction. The analysis of the now clearly revealed atomic transitions is currently ongoing.

In conclusion, the timing capability of MMC detectors has been demonstrated and applied for the first time for recording coincident x-ray spectra.

This research has been conducted in the framework of the SPARC collaboration, experiment E138 of FAIR Phase-0 supported by GSI. It is further supported by the European Research Council (ERC) under the European Union's Horizon 2020 research as well as by the innovation program (Grant No. 824109 "EMP"). We also acknowledge the support provided by ErUM FSP T05 - "Aufbau von APPA bei FAIR" (BMBF n° 05P19SJFAA and n° 05P19VHFA1).

References

[1] S. Kraft-Bermuth *et al.*, Atoms **6**, 59 (2018).

[2] D. Hengstler *et al.*, Phys. Scr. **T166**, 014054 (2015).

*p.pfaefflein@hi-jena.gsi.de

Novel Tunnel Magnetoresistive Sensor Functionalities via Oblique Incidence Deposition

Svenja Willing[1], Kai Schlage[1], Lars Bocklage[1,2], Mehdi Ramin Moayed[1], Tatiana Gurieva[1,3,4], Guido Meier[5,2], and Ralf Röhlsberger[1,2,3,4]

[1]DESY, Hamburg, Germany; [2]The Hamburg Centre for Ultrafast Imaging, Hamburg, Germany; [3]Helmholtz Institute Jena, Jena, Germany; [4]Friedrich-Schiller-Universität Jena, Germany; [5]Max-Planck Institute for the Structure and Dynamics of Matter, Hamburg, Germany

Controlling the magnetic properties of ultrathin films remains one of the main challenges to the further development of tunnel magnetoresistive (TMR) device applications. The magnetic response in such devices is mainly governed by extending the primary TMR trilayer with the use of suitable contact materials. The transfer of magnetic anisotropy to ferromagnetic electrodes consisting of CoFeB layers results in a field-dependent TMR response, which is determined by the magnetic properties of the CoFeB as well as the contact materials. We flexibly apply oblique-incidence deposition (OID) to introduce arbitrary intrinsic in-plane anisotropy profiles into the magnetic layers. The OID-induced anisotropy shapes the magnetic response and eliminates the requirement of additional magnetic contact materials. Functional control is achieved via an adjustable shape anisotropy that is selectively tailored for the ultrathin CoFeB layers. This approach circumvents previous limitations on TMR devices and allows for the design of new sensing functionalities, which can be precisely customized to a specific application.

Since the discovery of spin-dependent tunneling and tunnel magnetoresistance the race for ever increasing effect strengths of magnetic tunnel junctions (MTJs) has been ongoing. A huge leap forward was made with the invention of grain-to-grain epitaxy in amorphous CoFeB layers annealed in contact with MgO. This approach combines the advantages of smooth amorphous materials with the spin-selective properties of epitaxial interfaces and a crystalline tunnel barrier. Sensors based on the tunnel magnetoresistive (TMR) effect can be small, are robust, provide contact-free measurement, and excel in energy efficiency due to an inherently large resistance. Hence, TMR sensors are widely used in a variety of different applications.

However, great effort is required to shape the sensor response to a specific application. A given sensor is comprised of a number of sophisticated layer stacks which include various buffer layers as well as natural antiferromagnets. The latter ones are used for exchange-bias pinning of the magnetic reference layer and for the occasional soft pinning of the magnetic free layer. Modifying a given stack design to a new magnetic field sensing range has proven to be quite challenging.

Here we use oblique-incidence deposition (OID) to independently tailor the strength and orientation of the magnetic anisotropies in each of the CoFeB layers in a TMR stack [1]. The pronounced shape anisotropy induced via OID enables tuning of the magnetic properties of annealed CoFeB layers. Thus, the coercivity and direction of the magnetization axis in each ferromagnetic layer of a CoFeB/MgO/CoFeB magnetic tunnel junction can be freely adjusted through proper selection of both OID deposition angles (polar and azimuthal) and layer thickness. The OID thin films are in particular characterized by well-defined sharp magnetic switching fields. Moreover, hysteresis curves indicate domain-free remanent states.

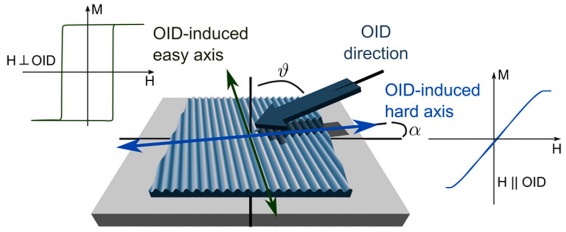

Figure 1: Oblique-incidence deposition of thin magnetic layers and induced magnetic anisotropy due to an anisotropic periodic surface roughness of the film. Typical magnetic hysteresis curves for field sweeps perpendicular and parallel to the oblique-incidence direction are shown.

Together, these unique features enable novel TMR sensor functionalities and allow for extremely flexible customization of the sensor properties to the particular application. Moreover, it eliminates the need for an elaborate exchange-bias pinning for certain sensing tasks. Our approach combines the well-known CoFeB/MgO material system with the possibility to imprint a wide range of magnetic anisotropy profiles into the layer stack, hence opening new possibilities for the design and economic realization of TMR sensors with archetypal high signal strength [1].

We acknowledge support by the Partnership for Innovation, Education and Research (PIER) between DESY and the University of Hamburg. This work is supported by the Cluster of Excellence "CUI: Advanced Imaging of Matter" of the DFG (EXC 2056, project ID 390715994)

References

[1] S. Willing, K. Schlage, L. Bocklage, M. Ramin Moayed, T. Gurieva, G. Meier and R. Röhlsberger, ACS Applied Materials and Interfaces **13**, 32343 (2021)

Generation of Isolated Attosecond Pulse due to Wavefront Rotation in Non-Collinear Gating Scheme

Dipti Bharti*[1], M. Zepf†[1,2], and M. Yeung‡[1,3]

[1]HI Jena, Helmholtzweg 4; [2]HI Jena, Fröbelstieg 3, Germany; [3]Room 01.043 - New Physics United Kingdom

The ultrafast wave-front rotation of a femtosecond laser pulse at its focus can lead to the generation of isolated attosecond pulses if the rotation velocity exceeds the radiation cone angle. Here, a non-collinear gating scheme is applied to surface high harmonic generation due to which attosecond pulses are angularly separated from each other this is shown through 2D-PIC simulations.

Significant effort has been made for the development of methods to generate isolated attosecond pulses. These pulses are suitable for probing ultrafast electronic processes in matter [1]. When a multi-cycle laser pulse with wavefront rotation is used as the driving pulse, it produces a train of attosecond pulses but the propagation direction of each pulses is angularly and spatially separated [2] . If the angular shift of these pulses is greater than the divergence of each attosecond pulses an isolated pulse can be extracted using an aperature.

Heyl *et al.* [3] proposed the non-collinear gating scheme and employed it in gaseous high harmonics generation. In this work, this scheme is to be applied to surface harmonic generation. Here, a non-collinear gating scheme is used to angularly streak the train of attosecond pulses in space. Two identical pulses ($\tau_{fwhm} = 10$ fs) having angular and peak-to-peak separation are incident on a target oriented 45° to the laser focus. Due to the non-collinear interaction of the beams, wave-front rotations take place at the focus which emits attosecond pulses each spatially separated. The schematic diagram is shown in Fig 1.

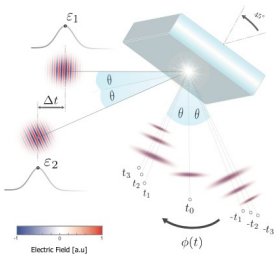

Figure 1: The geometry of the non-collinear gating scheme with two identical, temporally and angularly separated laser pulses incident on a target which is rotated 45°at the laser focus ($x = y = 0$) reproduced from [4].

The set-up in figure 1 consists of two identical pulses having peak-to-peak separation by a time Δt and angular separation by 2θ. When these pulses interact with the target oriented at 45°, ultra-fast wavefront rotation occurs at the focus which generates an isolated attosecond pulse which is separated from fundamental laser [2][3]. To isolate a pulse from the train of attosecond pulses several parameters such as: the intensity of laser pulse, the scale length and, the temporal separation between the two pulses (Δt) should be considered. The high intensity can cause denting of the plasma surface. The varying scale length affects the divergence of the individual attosecond pulses. Δt can directly affect the angular separation between central and adjacent attosecond pulses [4] since, increasing temporal delay between input pulses is responsible for increase in separation of central pulse from the neighbouring pulses but at the cost of reduced intensity.

The effectiveness of this scheme was investigated by performing 2D PIC simulations using EPOCH [5] and the obtained results are shown in Fig2.

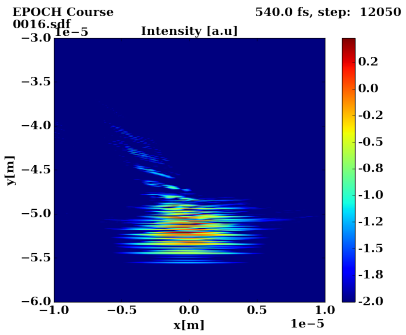

Figure 2: Plot of 2D PIC simulations of reflected intensity from the plasma surface. The simulation parameters are taken as: $\Delta t = 13.3$ fs, $\theta = 10°$, $\tau_{fwhm} = 10$ fs, $a_0 = 10$, $L = \lambda/10$, and $n_e > n_c$ [3].

Figure 2 shows the logarithm of the reflected intensity from the plasma surface. It can be observed that the gating scheme applied to Surface High Harmonic Generation was able to angularly streak the train of attosecond pulses. These results will be compared with the experimental results in coming few months. Experiment is currently being designed and plan for late this year.

References

[1] E. Balogh*et al.*, Faraday Discuss, **4**, 48 (2017).

[2] F. Quéré *et al.*J. Phys. B **47**, 124004 (2014).

[3] C. M. Heyl *et al.*New J. Phys., **16**, 52001 (2014).

[4] J. P. Kennedy *et al.*, "Isolated Ultra-bright Attosecond Pulses via Non-collinear Gating", unpublished.

[5] T. D. Arber *et al.*, PPCF **57**, 113001 (2015).

*dipti.bharti@hi-jena.gsi.de

†m.zepf@hi-jena.gsi.de

‡m.yeung@qub.ac.uk

THEORY

Derivative corrections to the Heisenberg-Euler effective action

Felix Karbstein*[1,2]

[1]Helmholtz Institute Jena, Germany; [2]Theoretisch-Physikalisches Institut, FSU Jena, Germany

We show that the leading derivative corrections to the Heisenberg-Euler effective action can be determined efficiently from the vacuum polarization tensor evaluated in a homogeneous constant background field. After deriving the explicit parameter-integral representation for the leading derivative corrections in generic electromagnetic fields at one loop, we specialize to the cases of magnetic- and electric-like field configurations characterized by the vanishing of one of the secular invariants of the electromagnetic field. In these cases, closed-form results and the associated all-orders weak- and strong-field expansions can be worked out. One immediate application is the leading derivative correction to the renowned Schwinger-formula describing the decay of the quantum vacuum via electron-positron pair production in slowly-varying electric fields.

In contrast to the classical notion of vacuum, describing the absence of everything, the vacuum of a quantum field theory (QFT) amounts to a highly non-trivial state. It is characterized by the omnipresence of quantum fluctuations of all the dynamical degrees of freedom of the underlying QFT. These fluctuations effectively endow the quantum vacuum with medium-like properties, such as a non-vanishing non-linear response to applied electromagnetic fields. The latter is in particular triggered by fluctuations of charged particles, which couple directly to electromagnetic fields, and depends on the charges and masses of all fluctuating particles. Within the Standard Model the leading effective interactions between electromagnetic fields are governed by quantum electrodynamics (QED).

A central quantity in the study of the effective nonlinear interactions of macroscopic electromagnetic fields in the QED vacuum is the Heisenberg-Euler effective Lagrangian $\mathcal{L}_{\rm HE}$ [1]. The latter arises from the microscopic theory of QED in a given prescribed electromagnetic field $F^{\mu\nu}$ by integrating out the dynamical degrees of freedom, namely the quantized spinor fields, describing electrons and positrons, and the quantum photon field. This supplements the classical Maxwell Lagrangian $\mathcal{L}_{\rm MW} = -\frac{1}{4}F_{\mu\nu}F^{\mu\nu}$ with effective, nonlinear self-interactions of the prescribed field. Apart from the applied electromagnetic field $F^{\mu\nu}$ and derivatives thereof the only physical parameters characterizing the latter are the electron mass m, and the elementary charge e mediating the coupling between charges and electromagnetic fields. In terms of Feynman diagrams $\mathcal{L}_{\rm HE}$ can be represented as an infinite set of vacuum diagrams, with the charged particle lines dressed to all orders in the external electromagnetic field and its derivatives. The simplest diagram is a one-loop diagram. Diagrams featuring more loops are parametrically suppressed with powers of the fine-structure constant $\alpha = e^2/(4\pi) \simeq 1/137$.

Reference [2] is devoted to the study of the leading derivative corrections to $\mathcal{L}_{\rm HE}$. Here, we demonstrate that the leading derivative correction to $\mathcal{L}_{\rm HE}$ can be determined from the vacuum polarization tensor evaluated in a generic constant and homogeneous background field. Our derivation constitutes an alternative route to the result of Ref. [3]. Using the explicit results available in the literature for the one-loop vacuum polarization tensor in the presence of a constant electromagnetic field as central input, we arrive at a rather compact expression for the quadratic derivative correction to $\mathcal{L}_{\rm HE}$ at one loop. In position space, this correction contains exactly two derivatives but arbitrary powers of the electromagnetic field $F^{\mu\nu}$.

The leading derivative correction to the effective interaction of four electromagnetic fields reads [2]

$$\begin{aligned}\mathcal{L}_\partial(F) = \frac{m^2}{4\pi^2}\Big(\frac{e}{m^2}\Big)^4\Big[&\frac{1}{180}F_{\mu\nu}F^{\mu\nu}\partial^\alpha F_{\rho\sigma}\partial_\alpha F^{\rho\sigma}\\ &+\frac{1}{280}F_{\mu\nu}F_{\rho\sigma}\partial^\alpha F^{\mu\nu}\partial_\alpha F^{\rho\sigma}\\ &-\frac{2}{63}F_{\rho\mu}F^{\sigma\mu}\partial^\alpha F_{\sigma\nu}\partial_\alpha F^{\rho\nu}\\ &-\frac{1}{420}F_{\rho\sigma}F^{\rho\alpha}\partial^\sigma F_{\mu\nu}\partial_\alpha F^{\mu\nu}\Big]\,. \quad (1)\end{aligned}$$

Especially for the special cases of magnetic- and electric-like field configurations characterized by the vanishing of one of the secular invariants of the electromagnetic field, we obtain closed-form expressions and work out all-orders weak- and strong-field expansions.

Apart from providing insights into fundamental aspects of strong-field QED, our results are relevant for precision studies of quantum vacuum nonlinearities in experimentally realistic field configurations beyond the locally constant field approximation. Of course, the strategy devised in the present work to determine derivative corrections to the Heisenberg-Euler effective Lagrangian for QED in four space-time dimensions can be readily extended to QED in other space-time dimensions as well as to other field theories, such as scalar QED.

This work has been funded by the DFG under Grant No. 416607684 within the Research Unit FOR2783/1.

References

[1] W. Heisenberg and H. Euler, Z. Phys. **98**, 714 (1936).

[2] F. Karbstein, JHEP **09**, 070 (2021).

[3] V. Gusynin and I. Shovkovy, J. Math. Phys. **40**, 5406 (1999).

*f.karbstein@hi-jena.gsi.de

Vacuum birefringence at x-ray free-electron lasers

F. Karbstein*[1,2], C. Sundqvist[1,2], K. S. Schulze[1,3], I. Uschmann[1,3], H. Gies[1,2], and G. G. Paulus[1,3]

[1]Helmholtz Institute Jena, Germany; [2]Theoretisch-Physikalisches Institut, FSU Jena, Germany; [3]Institut für Optik und Quantenelektronik, FSU Jena, Germany

We study the perspectives of measuring the phenomenon of vacuum birefringence predicted by quantum electrodynamics using an x-ray free-electron laser (XFEL) alone. We devise an experimental scheme allowing the XFEL beam to collide with itself under a finite angle, and thus act as both pump and probe field for the effect. The signature of vacuum birefringence is encoded in polarization-flipped signal photons to be detected with high-purity x-ray polarimetry. Our findings for idealized scenarios underline that the discovery potential of solely XFEL-based setups can be comparable to those involving optical high-intensity lasers. For currently achievable scenarios, we identify several key details of the x-ray optical ingredients that exert a strong influence on the magnitude of the desired signatures.

Vacuum birefringence is a finger print of quantum vacuum nonlinearity in strong electromagnetic fields [1]: when a strong electromagnetic field featuring a preferred direction is applied to the quantum vacuum, it can effectively supplement the latter with two different indices of refraction. Probe light with overlap to both of these polarization modes can experience a birefringence phenomenon. Originally linearly polarized probe light becomes slightly elliptically polarized, and thus gives rise to polarization-flipped signal photons.

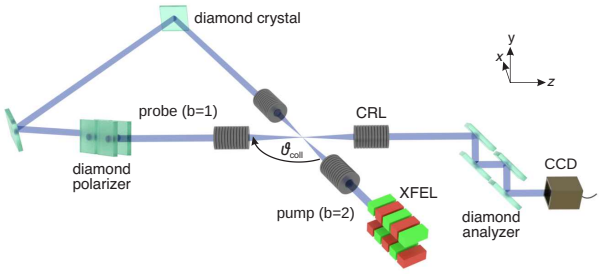

Figure 1: Illustration of the experimental setup. The original XFEL beam is focused with a compound refractive lens (CRL) to constitute the pump field. Subsequently, it is defocused with a CRL and by reflection at two diamond crystals directed back to the interaction point under an angle of $\vartheta_{\rm coll}$. Before reaching the interaction point, it is polarized with a diamond polarizer and the resulting probe beam focused to the interaction point with a CRL. Finally, it is defocused with another CRL, analyzed with a diamond analyzer and the signal registered with a CCD.

In Ref. [2], we study the perspectives of detecting vacuum birefringence solely based on the availability of an XFEL light source. The underlying idea is to introduce a self-crossing of the XFEL beam, allowing the beam to collide with itself. More precisely, we envision to make use of the well-controlled, regular pulse structure of the XFEL beam and adjust the propagation distances in our setup such as to ensure the collision of subsequent XFEL pulses. Hence, a given pulse acts as both pump and probe. After serving as a pump pulse for the preceding pulse, it probes the subsequent one. The basic setup envisioned by us for studying vacuum birefringence in a purely XFEL-based experiment is depicted in Fig. 1.

Our study is the first to consistently account for the losses of the focusing optics as well as pulse deformations induced by reflections of the original XFEL pulse at crystal surfaces. In particular, we demonstrate how severely predictions based on seemingly reasonably realistic assumptions may be affected when accounting for the details of the experimental setup devised to actually detect the phenomenon.

The attainable signal depends on the brightness of the source. In the experimental scenario envisioned by us the brightness of the source is clearly an essential key parameter: on the one hand, it determines the intensity of the pump field driving the vacuum birefringence effect. On the other hand, it controls the number of photons available for probing the phenomenon. Our study clearly identifies those building blocks that limit the quality of an experiment most severely – most prominently the sizable losses at the x-ray lenses. Improvements of these components could significantly increase the feasibility of such experiments. Moreover, we emphasize that future high-precision x-ray polarimeters have the potential to reach polarization purities $\mathcal{P} \lesssim 10^{-12}$ [3], which would generically also increase the discernible signal. Such developments will substantially improve the perspectives for precision tests of QED vacuum birefringence in XFEL based laboratory experiments.

This work has been funded by the DFG under Grant Nos. 416607684; 416611371; 416700351 within the Research Unit FOR2783/1.

References

[1] J. S. Toll, Ph.D. thesis, Princeton University (1952).

[2] F. Karbstein, C. Sundqvist, K. S. Schulze, I. Uschmann, H. Gies and G. G. Paulus, New J. Phys. **23**, 095001 (2021).

[3] K. S. Schulze, APL Photonics **3**, 126106 (2018).

*f.karbstein@hi-jena.gsi.de

Vacuum birefringence and diffraction at XFEL: towards optimal parameters

Elena A. Mosman[1] and Felix Karbstein*[2,3]

[1]National Research Tomsk Polytechnic University, Russia; [2]Theoretisch-Physikalisches Institut, FSU Jena, Germany; [3]Helmholtz Institute Jena, Germany

We study vacuum birefringence and x-ray photon scattering in the head-on collision of XFEL and high-intensity laser pulses. Resorting to analytical approximations for the numbers of attainable signal photons, we analyze the behavior of the phenomenon under the variation of various experimental key-parameters and provide new analytical scalings. Our results are essential for the identification of the optimal choice of parameters in a discovery experiment of vacuum birefringence at the Helmholtz International Beamline for Extreme Fields (HIBEF) at the European XFEL.

Quantum field theory predicts the vacuum to be characterized by the omnipresence of vacuum fluctuations. Vacuum fluctuations involving virtual charged particle-antiparticle pairs generically induce effective nonlinear couplings between electromagnetic fields; see the representative Feynman diagram describing the interaction of four electromagnetic fields via a virtual electron-positron pair shown in Fig. 1. These quantum vacuum nonlinearities result in violations of the classical superposition principle of electromagnetic waves in vacuum and give rise to a vacuum birefringence phenomenon [1]: as a consequence of the effective interaction of electromagnetic fields originally linearly polarized light traversing a strong-field region can pick up a small ellipticity, attributing a birefringence property to the quantum vacuum. This gives rise to signal photons quasi-elastically scattered into an originally empty, $\perp$-polarized mode. So far this effect has never been verified in a controlled laboratory experiment.

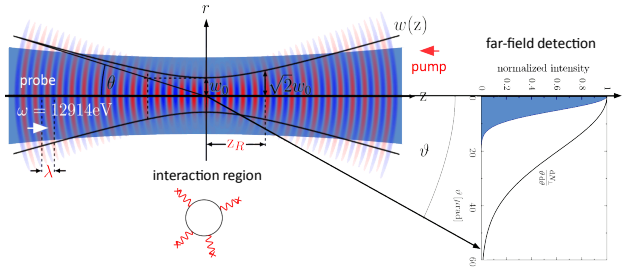

Figure 1: Schematic illustration of the scenario to detect vacuum birefringence: $\perp$-polarized probe photons scattered outside the forward cone constitute the signal.

The number of signal photons $N_\perp$ scales quadratically with the frequency of the probe and the intensity of the pump field, as well as linearly with the number of photons available for probing. This triggered theoretical proposals suggesting the use of an x-ray free electron laser (XFEL) as probe and a high-intensity laser as pump. The $\perp$-polarized signal is maximal in head-on collision of the driving laser fields. In the past years it was in particular emphasized that even the probe-photon energy preserving signature of vacuum birefringence is generically accompanied by a scattering phenomenon resulting in a different far-field angular decay of the signal photons; see Fig. 1 for an illustration.

A major challenge in experiment is the signal to background separation. Polarization-flipped signal photons are *discernible* from the large background of probe photons N traversing the interaction region without changing their properties if they fulfill the criterion

$$\frac{\mathrm{d}N_\perp}{\vartheta\,\mathrm{d}\vartheta} \geq \mathcal{P}\,\frac{\mathrm{d}N}{\vartheta\,\mathrm{d}\vartheta}\,, \tag{1}$$

where $\mathcal{P}$ is the polarization purity of the polarimeter used to detect the quantum vacuum signature. The number of discernible signal photons meeting this criterion is $N_{\perp>}$.

Focusing on the experimental parameters available at HiBEF at the European XFEL, and explicitly taking into account the non-trivial dependence of the number of photons N available for probing on the pulse duration and photon energy, in Ref. [2] we determined the optimal choices for the parameters in experiment such as to maximize the signal. See Fig. 2 for exemplary results indicating the existence of an optimal x-ray waist maximizing the birefringence signal for given other parameters. Figure 2 clearly demonstrates that the value of the optimal x-ray waist depends on the polarization purity $\mathcal{P}$.

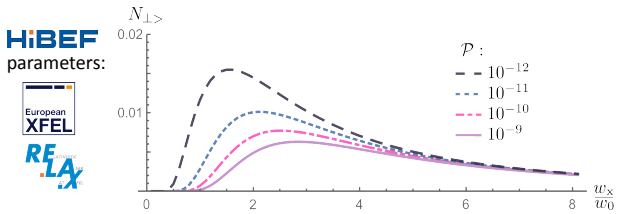

Figure 2: Dependence of the number of $\perp$-polarized signal photons meeting the criterion (1) on the probe waist w_x measured in units of w_0 for different values of $\mathcal{P}$.

This work has been funded by the DFG under Grant No. 416607684 within the Research Unit FOR2783/1.

References

[1] J. S. Toll, Ph.D. thesis, Princeton University (1952).

[2] E. A. Mosman and F. Karbstein, Phys. Rev. D **104**, 013006 (2021).

*f.karbstein@hi-jena.gsi.de

X-ray vacuum diffraction at finite spatiotemporal offset

Felix Karbstein*[1,2] and Ricardo R. Q. P. T. Oude Weernink[1,2]

[1]Helmholtz Institute Jena, Germany; [2]Theoretisch-Physikalisches Institut, FSU Jena, Germany

We study the nonlinear QED signature of vacuum diffraction in the head-on collision of optical high-intensity and x-ray free-electron laser pulses at finite spatio-temporal offsets between the laser foci. The high-intensity laser driven scattering of signal photons outside the forward cone of the x-ray probe constitutes a prospective experimental signature of quantum vacuum nonlinearity. Resorting to a simplified phenomenological ad-hoc model, it was recently argued that the angular distribution of the signal in the far-field is sensitive to the wavefront curvature of the probe beam in the interaction region with the high-intensity pump. In this work, we model both the pump and probe fields as pulsed paraxial Gaussian beams and reanalyze this effect from first principles. We focus on vacuum diffraction both as an individual signature of quantum vacuum nonlinearity and as a potential means to improve the signal-to-background-separation in vacuum birefringence experiments.

In Ref. [1] we consider the collision of two counter-propagating, linearly polarized laser pulses. Both laser pulses are assumed to be well described as paraxial Gaussian beams supplemented with a finite Gaussian temporal pulse envelope. The probe (pump) beam of oscillation frequency in the x-ray (optical) regime is propagating along the positive (negative) z axis. We furthermore allow for a finite spatio-temporal offset between the foci of these beams. Without loss of generality the probe is assumed to be focused at $\mathbf{x} = 0$. In accordance with the predictions of Ref. [2] we expect combined longitudinal and transverse focal offsets to result in an angular shift of the signal photon distribution in the far field away from the forward beam axis of the probe; see Fig. 1.

In our explicit examples the beam radius of the probe in the interaction region with the pump is always larger than the beam radius of the pump. In accordance with naive expectations, for longitudinal offsets of the order of the probe Rayleigh range and transverse offsets of the order of the probe waist wavefront curvature effects of the probe can no longer be neglected and leave an imprint on the far-field directional distribution of the signal photons. Most prominently, this can result in a finite angular shift of the main emission direction of the signal away from the forward beam-axis of the probe.

We put special attention on discernible signals in prospective discovery experiments of QED vacuum nonlinearity. To this end, we consider both polarization-insensitive measurements and the detection of polarization-flipped signal photons utilizing high-definition polarimetry. Our results allow to assess the impact of large focal offsets on the attainable signals. Hence, they are also relevant for the analysis of experimental scenarios suffering from large shot-to-shot fluctuations, which result in non-optimal collisions. We put special attention on the asymmetry imprinted on the far-field angluar distribution of the signal by utilizing both finite longitudinal and transverse focal offsets.

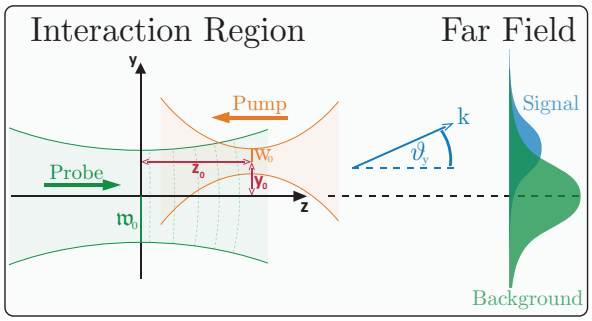

Figure 1: Sketch of the considered scenario: we envision the collision of two counter-propagating laser pulses allowing for a finite offset between the beam foci. This provides a means to shift the main emission direction of the signal photons in the far field away from the forward beam axis of the probe [2]. The probe photons traversing the interaction region unaltered constitute the background against which the signal must be discriminated.

It would certainly be very interesting to repeat the present analysis with probe beams featuring different transverse profiles in the interaction region with the high-intensity laser pulse, such as top-head or flattened-Gaussian beams [3]: while the transverse decay of the Gaussian probe inevitably comes with a reduction of the photons available for probing at finite transverse offsets, a flattened beam would not suffer from this loss. This could provide a means to increase the discernible signals.

This work has been funded by the DFG under Grant No. 416607684 within the Research Unit FOR2783/1.

References

[1] F. Karbstein and R. R. Q. P. T. Oude Weernink, Phys. Rev. D **104**, 076015 (2021).

[2] Y. Seino, T. Inada, T. Yamazaki, T. Namba and S. Asai, PTEP **2020**, 073C02 (2020).

[3] F. Karbstein and E. A. Mosman, Phys. Rev. D **101**, 113002 (2020).

*f.karbstein@hi-jena.gsi.de

Enhanced entanglement from Ince-Gaussian pump beams in the spontaneous parametric down-conversion

B. Baghdasaryan*[1,3], F. Steinlechner[3,4], and S. Fritzsche[1,3,4]

[1]Helmholtz Institute Jena, Germany; [2]Fraunhofer Institute for Applied Optics and Precision Engineering IOF, Germany; [3]Theoretisch-Physikalisches Institut, Friedrich-Schiller-Universität Jena, Germany.; [4]Abbe Center of Photonics

Spontaneous parametric down-conversion (SPDC) is a valuable source for generation of photonic entanglement. An advantage of SPDC is that simple expressions for the two-photon state can be obtained by using the thin-crystal approximation. Knowledge of the conditions under which the thin-crystal approximation remains valid is essential for the realization of experimental setups. We provide a quantitative guideline on the validity of the thin-crystal approximation in calculating the two-photon spatial state. In particular, we show that the applicability of this regime is related to the focusing parameter $\overline{w}_p = w_p/\sqrt{\lambda_p L}$, where w_p and λ_p are the beam waist and wavelength of the pump beam, respectively, and L is the length of the nonlinear crystal.

Spontaneous parametric down-conversion (SPDC) is a nonlinear (optical) process that converts high-energy photons by a nonlinear crystal into pairs of entangled photons. The state of a photon-pair also called the two-photon state, is derived from the second-order perturbation theory. The third order of the perturbation theory gives rise to four photons generation, which is an unlikely process and can be neglected. SPDC is usually described in narrowband or thin-crystal approximations at degenerate frequencies to describe the spatial correlations. The thin-crystal regime can be achieved only under very particular experimental conditions, which has not been reported before: a quantitative discussion of the two-photon mode distribution depending on the validity of the thin-crystal approximation is still missing.

In the work [1], we analyzed how the Rayleigh range of the pump beam or the crystal length should be chosen in order to reach a good fulfillment of the thin-crystal regime. In particular, we first constructed the spatial structure of the two-photon state for the thick and thin-crystal regimes. Secondly, we defined a quantity to determine the distance between these two states, namely trace distance.

Figure 1 shows the trace distance D as a function of the crystal length L and the beam waist w_p for the typical wavelength $\lambda_p = 405$ nm. The thin-crystal approximation is *well* fulfilled in the white region (upper left quarter), whereas in the purple region (region under solid line), it is not justified. Any calculations in the purple area would lead to a deviation from the thin-crystal regime and strongly affect the spatial mode distribution of the two-photon state. Especially, spatially engineered high-dimensional, entangled states based on thin-crystal approximation will dramatically change if the approximation is not well satisfied. In principle, if the pump beam waist is large enough, a good

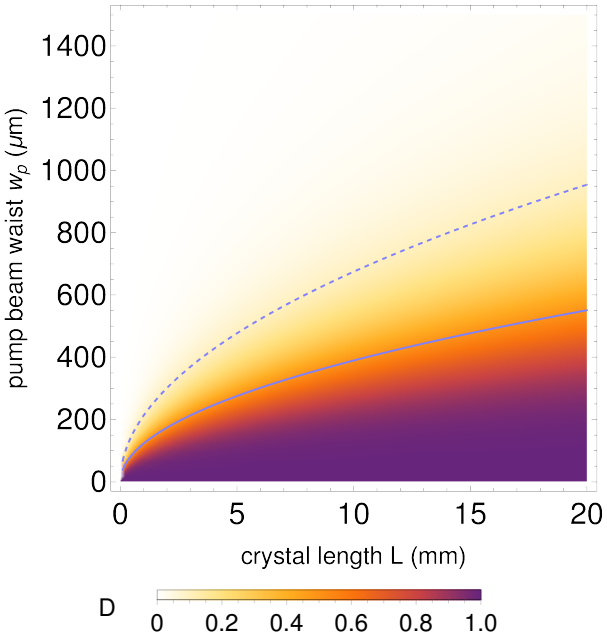

Figure 1: Trace distance D as a function of crystal length L and pump beam waist w_p for the typical wavelength, $\lambda_p = 405$ nm. The white region (upper left quarter) refers to a well fulfillment of the thin-crystal approximation. In contrast, the purple region (region under solid line) indicates a strong violation of the approximation. The dashed and solid lines display the conditions $D = 0.1$ and $D = 0.5$, respectively. These curves show a square root dependence $w_p \propto \sqrt{L}$, where the higher D is, the larger the slope of the curve.

fulfillment of the thin-crystal regime can be reached for any crystal length. Furthermore, we also indicated in Fig. 1 the curves with conditions $D = 0.1$ (solid line) and $D = 0.5$ (dashed line) to confirm the expected relation $w_p \propto \sqrt{L}$. As we can see, the smaller the selected trace distance D is, the larger the curve slope.

In conclusion, we have explored the validity of the thin-crystal approximation in the SDPC process and find that fulfillment of this often-employed approximation can be determined for many experimental situations by just calculating $\overline{w}_p$ and comparing it with Fig. 1.

References

[1] B. Baghdasaryan, F. Steinlechner, and S. Fritzsche, Phys. Rev. A **103**, 063508 (2021).

*baghdasar.baghdasaryan@uni-jena.de

Simulation of an Inverse Compton Source for LUXE

D. Dupish*[1] and D. Seipt[1]

[1]Helmholtz Institute Jena, Fröbelstieg 3, 07743 Jena, Germany

LUXE (Laser Und XFEL Experiment) aims at investigating QED processes in strong electromagnetic fields with unprecedented accuracy [1]. In particular, LUXE will study nonlinear Breit-Wheeler pair production in photon-laser collisions, making the design and optimization of the hard γ-ray sources a priority. We present here simulations of Inverse Compton scattering spectra, and we estimate the number of produced positrons by colliding the optimized γ-ray beam with a high-intensity laser pulse.

In order for nonlinear Breit-Wheeler pair production to be efficient, the quantum parameter of the high-energy photons has to be $\chi \approx 0.01161 \xi \omega_\gamma(\mathrm{GeV}) \sim 1$, where ξ is the laser intensity parameter. For values of ξ planned for LUXE [1], this means multi GeV γ-rays need to be produced for effective photon-laser collisions. Besides using a Bremsstrahlung source which provides broadband γ-rays up to 16.5 GeV, an Inverse Compton Source (ICS) could generate quasi-monoenergetic γ-rays, which would be favorable.

The simulations of the Compton source are performed using the Monte Carlo code LUXEICS [2]. The ebeam is focused at the ICS interaction point where it collides with a frequency-tripled laser pulse (300 nm) to produce GeV photons with ω_γ sufficiently large. These high-energy photons are then propagated to the strong-field IP, at a distance $L = 7.5$ m downstream, where their density and spectrum is analyzed. To optimize the γ photon flux and spectrum at $\mathrm{IP}_{\mathrm{strong}}$, we studied their behavior as a function of the electron focal spot size σ_T.

The momentum and position of the beam electrons (100 pC beam charge) were sampled using Gaussian distributions centered at 16.5 GeV with a relative energy spread of 0.1% and normalized emittance of 1.4 mm mrad. To maximize the electron-laser beam overlap, the laser waist w_{ICS} was taken as equal to σ_T while keeping the pulse energy constant at 100 mJ. Thus, increasing w_{ICS} means we decrease the laser intensity parameter ξ_{ICS} according to $w_{\mathrm{ICS}}\xi_{\mathrm{ICS}} = const.$, keeping $\xi_{\mathrm{ICS}} < 0.1$. The laser pulse duration is taken as 1 ps. The plots in Fig. 1 show that the maximum photon density is observed for smaller σ_T with a rapid decrease with increasing σ_T, where $\sigma_T \approx 5$ µm will be the smallest spot size achievable with the planned beamline design. The smaller σ_T are accompanied by a broadband energy spectrum while narrowband energy spectrum is observed for larger σ_T.

The main purpose of optimizing the photon density is to maximize the nonlinear Breit-Wheeler positron yield at

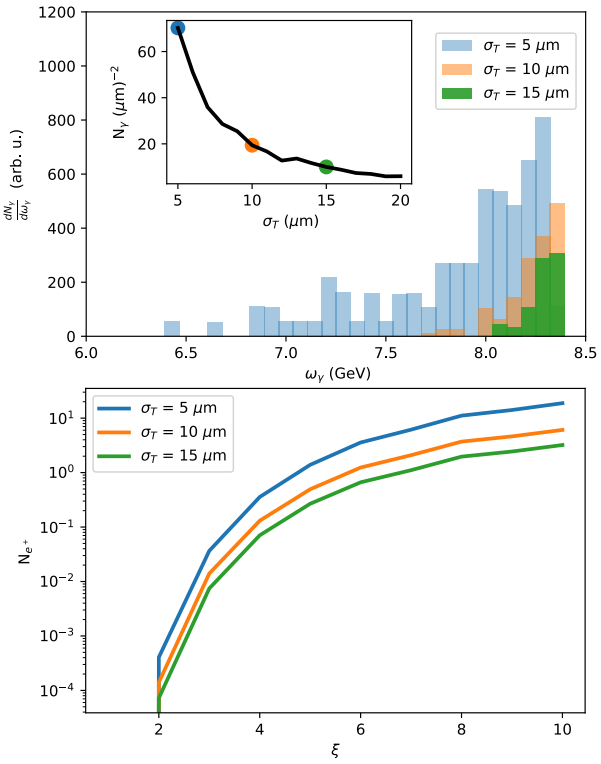

Figure 1: Upper: ICS photon spectrum at the $\mathrm{IP}_{\mathrm{strong}}$ and the photon density (inset) as a function of σ_T, calculated inside a spotsize $r = 5$ µm. Lower: Positron yield per shot as a function of peak normalised vector potential ξ.

$\mathrm{IP}_{\mathrm{strong}}$. This non-linear Breit-Wheeler pair production process is simulated using the Monte Carlo code PTARMIGAN [3]. Currently the input γ-ray beam is limited to a Gaussian spectrum. We thus approximate our simulation results of Fig. 1 by Gaussians with same mean value, standard deviation, and peak flux. The pulse energy of the high-intensity laser was taken as the design values (30 fs, 9 J) [1], thus keeping $w_0\xi$ = 48 µm. Fig. 1 shows that the largest number of positrons per shot N_{e+} are observed for small σ_T and largest ξ. In conclusion, a tightly focused ebeam maximizes the positron yield. The larger photon flux in that case clearly outperforms the lower mean energy (smaller χ) and larger bandwidth of the gamma rays.

References

[1] H. Abramowicz *et al.*, LUXE Conceptual Design Report, Eur. Phys. J.: Special Topics **230**, 2445 (2021).

[2] `https://github.com/danielseipt/luxeics`

[3] `https://github.com/tgblackburn/ptarmigan`

*`dupish.dupish@uni-jena.de`

A generalized SFA-theory of high-order harmonic generation for arbitrary spatially structured driving fields

B. Minneker*[1,2,3], B. Böning[2,3], and S. Fritzsche[1,2,3]

[1]Theoretisch Physikalisches Institut, Friedrich-Schiller-Universität, Jena; [2]Helmholtz Institut, Jena; [3]GSI Helmholtzzentrum für Schwerionenforschung GmbH, Darmstadt

This work generalizes the well-known strong-field approximation (SFA) of high-harmonic generation (HHG) by considering the spatial structure of the driving beam. Our theoretical model manages to take into account an arbitrary spatial structure with relativistic corrections up to the first order. In general, this enables investigation of non-dipole effects of linearly polarized plane waves in the high harmonic process, but also investigations related to more complex spatially structured beams. The opportunity to study those beams and their effect on the high harmonic process is not encountered by current models. We validate our theoretical model by analytically reproducing the results of the established non-dipole SFA. In addition, we point out that more complicated cases can be simulated with our model, which are not accessible for the established models. As a result, the discussed model allows for studying a broader variety of beam configurations than current theories and models.

The strong-field approximation (SFA) of high-harmonic generation is a popular technique to investigate the production of high-order harmonics. Since the SFA considers the driving beam as only time-dependent, effects from the spatial structure of the beam are not included in this theory. To take those effects into account, we develop an SFA theory that takes the spatial structure into account up to the first order in the relativistic correction. Therefore, we solved the Schrödinger equation of an electron in an arbitrary vector potential with an iterative approach. In the end, all relativistic corrections of the order $1/c^2$ are omitted. The associated non-dipole Volkov states of the electron in the continuum are

$$\chi_{\boldsymbol{p}}(\boldsymbol{r},t) = (2\pi)^{-3/2} e^{-i(E_{\boldsymbol{p}}t - \boldsymbol{p}\cdot\boldsymbol{r})} e^{-i\Gamma(\boldsymbol{r},t)}, \qquad (1)$$

with $\Gamma(\boldsymbol{r},t)$ as the non-dipole Volkov phase [1, 2]. The non-dipole Volkov phase for an elliptical polarized plane wave reads

$$\Gamma(\boldsymbol{r},t) = \frac{1}{\eta_{\boldsymbol{k}}}\left(\boldsymbol{p}\boldsymbol{A}(\boldsymbol{r},t) + \frac{\boldsymbol{A}^2(\boldsymbol{r},t)}{2}\right). \qquad (2)$$

To decouple the spatial from the temporal dependencies, we expand $\boldsymbol{A}(\boldsymbol{r},t)$ to the first relativistic correction and separate both contributions. This separation enables us to use the saddle-point approximation for the momentum integral. Applying a further saddle-point approximation for the remaining time integrals leaves the following equation

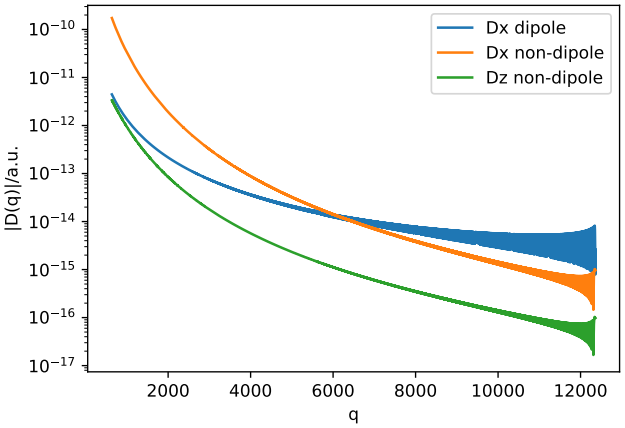

Figure 1: Modulus of the dipole moment calculated in the dipole and non-dipole SFA. The driving beam is linearly polarized, the intensity $I_0 = 10^{17}$ W/mm^2 and the wavelength $\lambda = 800$ nm with the target ion Ne^{6+}.

for the dipole moment:

$$\boldsymbol{D}(q) = \sum_{s=(p_s,t_s,t'_s)} iC(p_s,t'_s,t_s)\boldsymbol{\Upsilon}(\pi(p_s,t_s)) \boldsymbol{E}(t'_s)\boldsymbol{d}(\pi(p_s,t'_s))e^{-i(S(p_s,t'_s,t_s)-\omega_q t_s)}. \qquad (3)$$

Even though this equation may look similar to the usual SFA dipole amplitude, it accounts for non-dipole interactions due to the driving beam. A comparison of both theories is shown in Fig. 1.

In conclusion, we developed a generalization of the well-established non-dipole SFA. The generalized SFA can consider arbitrary spatially structured driving fields. However, we demonstrated this for, in general, elliptical polarized driving fields. Other spatially structured driving fields like Bessel or Laguerre-Gaussian beams will be considered in further investigations.

References

[1] B. Böning, W. Paufler and S. Fritzsche, Phys. Rev. A **99**, 053404 (2019).

[2] L. Rosenberg and F. Zhou, Phys. Rev. A **47**, 2146 (1993).

*bjoern.minneker@uni-jena.de

A curvature bound from gravitational catalysis in thermal backgrounds

Holger Gies*[1,2] and Abdol Sabor Salek[1]

[1]HI Jena, Fröbelstieg 3, 07743 Jena, Germany; [2]TPI, FSU Jena, Fröbelstieg 1, 07743 Jena, Germany

Catalysis in quantum field theory denotes symmetry breaking and fermion mass generation triggered by a strong external field. The phenomenon of magnetic catalysis [1] is widely studied in particle and solid-state physics. A similar phenomenon exists in strong gravitational fields and is influenced by thermal backgrounds [2]. We study gravitational catalysis in the early universe in conjunction with general scenarios of quantized gravity. Using a scale-dependent analysis, we derive a thermal bound on the curvature of local patches of spacetime [3]. This bound quantifies regions in parameter space that remain unaffected by gravitational catalysis and thus are compatible with the existence of light fermions as observed in nature. In an application to the Asymptotic Safety scenario of quantum gravity, our bound translates into a thermal-history-dependent upper bound on the number of fermion flavors.

Chiral symmetry breaking and fermion mass generation is a central feature of interacting fermions relevant for the standard model shaping many properties of matter in the universe. Whereas the long-range limit of gravity in the form of Einstein's general relativity is too weakly interacting to affect the status of chiral symmetry, gravity is expected to become more strongly interacting at or above the Planck scale. Whether or not gravity or its quantized form may exert a strong influence on the chiral features of fermions deserves to be studied.

In analogy to a well understood mechanism in QED in strong electromagnetic fields, gravity offers a mechanism to trigger fermion mass generation via the structure of spacetime itself. The most widely studied mechanism occurs on negatively curved spacetimes and can be summarized by *gravitational catalysis*.

In our work [3], we explore gravitational catalysis specifically by including the effects of finite temperature, using a scale-dependent approach. The advantage is that we can monitor the status of chiral symmetry on all scales, specifically in the Planckian regime and beyond. Provided a notion of curvature exists in that regime, gravitational catalysis could be active and drive fermion mass generation. This would result in correspondingly heavy fermions removing light fermions from the observable long-range spectrum – in stark contrast to the observed existence of light fermions such as the electron in nature.

This observational fact leads to the notion of curvature bounds: in order to guarantee that a given (quantum) gravity scenario is not affected by the problem of gravitational catalysis, the averaged curvature of a local patch of spacetime should not exceed a certain bound.

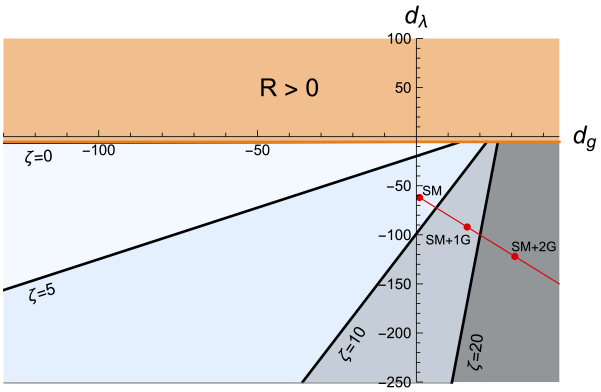

Figure 1: Space of asymptotically-safe quantum gravity theories with matter parametrized by d_g and d_λ, cf. [3]. Each of the four solid lines distinguish regions free from gravitational catalysis (region above/left of each line) from regions that violate our curvature bound (darker shaded region below/right of each line) as a function of a temperature parameter $\zeta \sim T$. The red dot marks the Standard Model (SM) matter content with the red line indicating the Standard Model with additional fermionic generations.

Monitoring also the influence of finite temperature on the mechanism is of great relevance for the cosmological evolution. Indeed, our results provide evidence for a comparatively strong dependence of gravitational catalysis on the details of the background. At the same time, finite-temperature effects can significantly relax the curvature bounds – in line with the expectation that thermal fluctuations drive the system towards the disordered symmetric phase.

Within a concrete quantum gravity scenario, the curvature bound can translate into a bound on the particle content of the matter sector. Results for Asymptotically Safe Quantum Gravity are shown in Fig. 1 illustrating the consistency of a standard-model-like particle content but indicating a tension with models with a substantially larger fermion number.

This work has been funded by the DFG under 406116891 within RTG 2522/1.

References

[1] V. P. Gusynin, V. A. Miransky and I. A. Shovkovy, Phys. Rev. Lett. **73**, 3499(1994) [E. *ibid* **76**, 1005 (1996)].

[2] I. Sachs and A. Wipf, Phys. Lett. B **326**, 105(1994).

[3] H. Gies and A. S. Salek, Phys. Rev. D **103**, 125027 (2021).

*holger.gies@uni-jena.de

Non-sequential double ionization with elliptically polarized laser beams

F. Liu*[1,2,3], B. Böning[2,3], and S. Fritzsche[1,2,3]

[1]Helmholtz Institute Jena, Fröbelstieg 3, 07743 Jena, Germany; [2]Theoretisch-Physikalisches Institut, Friedrich-Schiller-Universität Jena, 07743 Jena, Germany; [3]GSI Helmholtzzentrum für Schwerionenforschung GmbH, 64291 Darmstadt, Germany

We show through simulation that an improved quantitative re-scattering model (QRS) can successfully predict the nonsequential double ionization (NSDI) process by intense elliptically polarized laser pulses. Using the QRS model, we calculate the correlated two-electron distribution (CMD) and ion momentum distributions of NSDI of Ne exposed to intense elliptically polarized laser pulses with a wavelength of 788 nm at a peak intensity of 5.0×10^{14} W/cm^2 . We analyze the asymmetry in the doubly charged ion momentum spectra that were observed by H. Kang *et al.* [1] in the transition from linearly to elliptically polarized laser pulses. Our model reproduces their experimental data well. In addition, we find that this ellipticity-dependent asymmetry is due to the drift velocity along the minor axis of the polarization ellipse. It is indicated that the correlated electron momentum distributions along the minor axis provides access to the subcycle dynamics of recollision and distinguish recollisions before and after the zero crossing of the field.

According to the QRS model [2], the CMD for laser-induced electron re-collision direct ionization (RDI) in NSDI can be factorized as a product of the re-colliding wave packet (RWP) and the field-free differential cross section for ionization of the parent ion by the impact of the laser-induced returning electron. For a given intensity, the CMD for laser-induced RDI process in the laser field is obtained as

$$D_I^{(\mathrm{RDI})}(p_\parallel^1, p_\parallel^2) = \int_{I_p}^{\infty} dE_i\, D_{E_i,I}^{(\mathrm{RDI})}(p_\parallel^1, p_\parallel^2) W_I(E_i - \Delta E)$$

where $W_I(E_i - \Delta E)$ is the RWP describing the momentum distribution of the returning electron at a single intensity I, which can be calculated by using the strong-field approximation.

Finally, to compare with experimental measurements, the integration over the focus volume should be performed,

$$D_{I_0}^{(\mathrm{RDI})}(p_\parallel^1, p_\parallel^2) = \int_0^{I_0} dI\, D_I^{(\mathrm{RDI})}(p_\parallel^1, p_\parallel^2) \frac{dV}{dI}$$

Using the QRS model [2], we computed the ion momentum distribution for NSDI of Ne in 788 nm laser pulses at a peak intensity of 5.0×10^{14} W/cm^2 with ellipticites of 0.0 and 0.25 respectively. We present our results in Fig. 1. It can be seen from the figure that the QRS model reproduces the assymetry pattern of the experimental findings.

In the present work, we focus on unveiling the mechanisms for the ellipticity-dependent asymmetry of ion momentum distributions. Our study reveals that this ellipticity-dependent asymmetry is due to the drift velocity along the minor axis of the polarization ellipse. Our calculation confirms that the recollisions are more likely to occur after E_z crosses zero for higher elliptities. Futhermore, our results demonstrate that the distorting potential in ion momentum distributions of NSDI plays an important role. It is known that the Coulomb potential plays an important role in CMDs, however, we find that the ion momentum distributions are more in line with the experimental measurements when we consider the use of a distorted wave function to describe the returning electron.

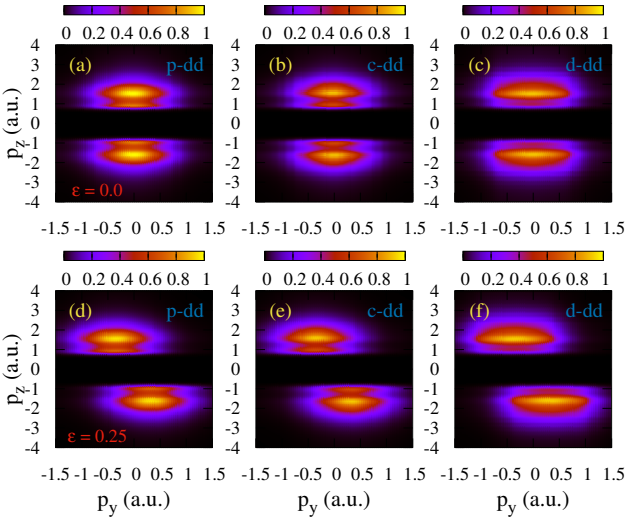

Figure 1: Normalized ion momentum distribution of Ne^{2+} in the $y-z-$ polarization plane of elliptically polarized laser pulses at a peak intensity of 5.0×10^{14} W/cm^2 and wavelength of 788 nm. The results with ellipticity $\epsilon = 0$ (top row) and the results with ellipticity $\epsilon = 0.25$ (bottom row) are compared for different initial wavefunctions: plane waves (a,d), Coulomb waves (b,e) and distorted waves (c,f), respectively.

This work was supported by the Deutsche Forschungsgemeinschaft (DFG, German Research Foundation) under Project No. 440556973.

References

[1] H. Kang *et al.*, Phys. Rev. Lett. **120**, 223204 (2018).

[2] Z. Chen *et al.*, Phys. Rev. Lett. **79**, 033409 (2009).

*fangfangliu2020@gmail.com

Photo-excitation of atoms by cylindrically polarized Laguerre-Gaussian beams

S. Ramakrishna [*1,2,3], J. Hofbrucker[1,2], and S. Fritzsche[1,2,3]

[1]Helmholtz-Institut Jena, Fröbelstieg 3, D-07743 Jena, Germany; [2]GSI Helmholtzzentrum für Schwerionenforschung GmbH, Germany; [3]Theoretisch-Physikalisches Institut, Friedrich-Schiller-Universität Jena, Germany

We analyze the photo-excitation of atoms with a single valence electron by cylindrically polarized Laguerre-Gaussian beams. Theoretical analysis is performed within the framework of first-order perturbation theory and by expanding the vector potential of the Laguerre-Gaussian beam in terms of its multipole components. We calculate the total excitation rate of electric quadrupole transition ($4s\ ^2S_{1/2} \rightarrow 3d\ ^2D_{5/2}$) in a mesoscopic target of Ca^+ ions driven by cylindrically polarized Laguerre-Gaussian beams. Our calculations show that the total rate of excitation is sensitive to beam waist and distance between center of the target and the beam axis. However, the excitation by cylindrically polarized Laguerre-Gaussian beams is found more efficient in driving electric quadrupole transitions in the mesoscopic target than circularly polarized beams.

Laguerre-Gaussian (LG) beams are paraxial twisted light beams whose amplitude distribution satisfies the paraxial wave equation in cylindrical coordinates. In addition to spin angular momentum, LG beams carry orbital angular momentum (OAM) as a result of exponential phase dependence. Along with the projection of OAM m_l, the radial index p can be used to characterize an LG beam. The width of the LG beam varies along the propagation distance and has a minimum at the focus which is known as the beam waist w_o. In contrast to plane waves, the intensity profile of an LG beam consists of an annular ring structure determined by the values of m_l and p.

In addition to circular, linear and elliptical polarization, an LG beam can have cylindrical polarization. Cylindrically polarized LG beams can be constructed as a linear combination of two circularly polarized LG beams [1]. This results in non-separable spatial and polarization modes. As a consequence of the coupling between spatial and polarization modes, the state of polarization (SOP) in the beam cross-section of cylindrically polarized LG beams is spatially in-homogeneous. LG beams with spatially in-homogeneous SOP are known as vector LG beams and two prominent examples are radially and azimuthally polarized LG beams.

For the first time in 2016 [2], excitation of atoms by an LG beam was performed to demonstrate the transfer of OAM from a circularly polarized LG beams to bound electrons. However, the excitation of atoms by cylindrically polarized LG beams remains less explored. Hence, in our theoretical work [3], we consider photo-excitation of atoms by radially and azimuthally polarized LG beams. To perform this analysis, we use first-order perturbation theory and the multipole expansion of the vector potential of the LG beam. Further, we consider a mesoscopic target of Ca^+ ions and calculate the total rate of excitation W_{fi}^{LG} for the electric quadrupole (E2) transition ($4s\ ^2S_{1/2} \rightarrow 3d\ ^2D_{5/2}$). In Fig. 1, we plot W_{fi}^{LG} as a function of width of the target for two different radial positions $b_{o,x}$ of the target in the beam cross-section. Our results explicitly show that cylindrically polarized LG beams are more efficient in driving E2 transitions in a mesoscopic target than circularly polarized beams.

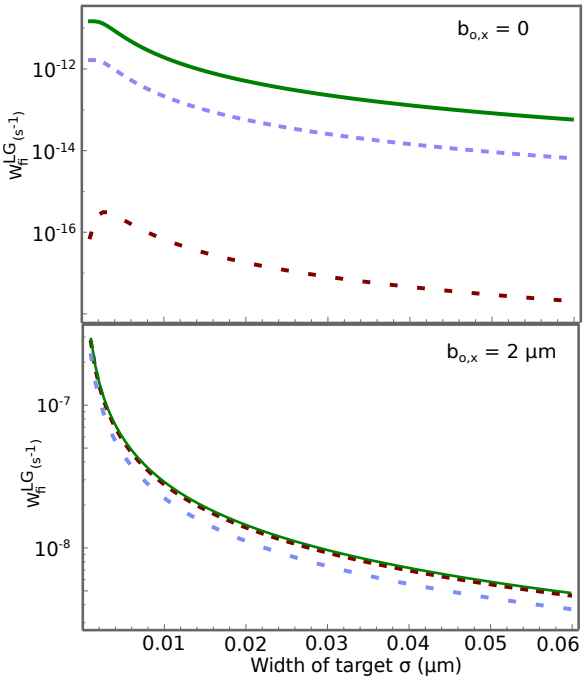

Figure 1: Log plot of total rate of excitation for electric quadrupole transition between 4s $^2S_{1/2} \rightarrow$ 3d $^2D_{5/2}$ levels of Ca^+ ion driven by LG beam is plotted as a function of width of the target σ for azimuthal (green solid line), radial (brown dashed line) and circular polarization (blue dotted line). In the above plot, $p = 0$ and $w_o = 2.7\mu m$.

The authors acknowledge funding from Research School of Advanced Photon Science (RS-APS) of Helmholtz Institute Jena, Germany.

References

[1] G. F. Quinteiro *et al.*, Phys. Rev. A. **95**, 012106 (2017).

[2] C. T. Schmiegelow *et al.*, Nat.Commun **7**, 1 (2016).

[3] S. Ramakrishna, J. Hofbrucker, S. Fritzsche, Phys. Rev. A., Accepted (2022).

* shreyas.ramakrishna@uni-jena.de

Many-electron QED with redefined vacuum approach

R. N. Soguel*[1,2,3], A. V. Volotka[4], D. A. Glazov[5], and S. Fritzsche[1,2,3]

[1]Theoretisch-Physikalisches Institut, Friedrich-Schiller-Universität Jena, Germany; [2]Helmholtz Institute Jena, Germany; [3]GSI Helmholtzzentrum für Schwerionenforschung GmbH, Germany; [4]Department of Physics and Engineering, ITMO University, Russia; [5]Department of Physics, St. Petersburg State University, Russia

The redefined vacuum approach, which is frequently employed in the many-body perturbation theory, proved to be a powerful tool for formula derivation. We elaborate this approach within the bound-state QED perturbation theory. In addition to general formulation, we consider the particular example of a single particle (electron or vacancy) excitation with respect to the redefined vacuum. Starting with simple one-electron QED diagrams, we deduce first- and second-order many-electron contributions: screened self-energy, screened vacuum polarization, one-photon exchange, and two-photon exchange. The redefined vacuum approach provides a straightforward and streamlined derivation and facilitates its application to any electronic configuration. Moreover, based on the gauge invariance of the one-electron diagrams, we can identify various gauge-invariant subsets within derived many-electron QED contributions.

Highly charged ions are considered as one of the best available natural laboratories to access strong field effects at the moment; highlighting the need to go beyond the perturbative regime since for high Z, the αZ expansion parameter is comparable to one (where Z is the nuclear charge number and α is the fine-structure constant). Although many approximate methods have access to higher-order corrections within the Breit approximation, such as relativistic many-body perturbation theory (RMBPT), relativistic configuration–interaction (CI) method, or multi-configuration Dirac–Fock (MCDF) method, the increasing precision in modern spectroscopy enforces accurate *ab initio* description of few- to many-electron systems within the bound-state QED.

In general, QED can be applied to any many-electron atoms even though it is most deeply developed for hydrogen and helium [1], and hydrogen-like ions [2], where the accuracy of the calculations has reached a remarkably high level. In the case of highly charged ions, the question arises: can we perform *ab initio* QED calculations for many-electron systems? The computations are so far limited to selected, relatively simple systems not only due to the complexity of numerical calculations but also because of difficulties in deriving formal expressions.

The concept of a vacuum redefinition naturally arose in quantum field theory due to the notion of the fully occupied negative-energy continuum of fermion states, the so-called Dirac sea. The vacuum redefinition technique is widely accepted and demonstrated within RMBPT formalism [3, 4]. In Ref. [5], we further elaborate the redefined vacuum approach within the QED perturbation theory. The essential notion in introducing a redefined vacuum is to separate the electron dynamics into the "core" and "valence" parts. The many-electron contributions are extracted as the difference of two integrals over altering integration contours, each in link with its respective vacuum state. In this way, the interaction of the reference particle (electron or hole) with core electrons is taken into account within the QED framework. The great advantage of the method is that instead of the all-electron states one deals with the few-valence-electron states, which represents a much smaller Hilbert space.

As an example, the method is applied to atoms with a single-hole electronic configuration, which occurs in halogen atoms such as fluorine, chlorine, etc. The particular interest in this system is twofold. First, in Refs [6, 7] it was demonstrated that highly accurate theoretical predictions are possible in such atoms, and thus accurate tests of the QED effects become feasible. Second, such an example is chosen due to the fact that two-photon-exchange correction is still uncalculated for fluorine-like ions as well as due to recent experimental efforts for such systems.

In Ref. [5], we have derived the formulas for the QED contributions up to the second order in α for the single-hole configuration. The screened radiative and two-photon-exchange corrections have been carefully extracted from the rigorous formulas obtained within the redefined vacuum formalism. An important advantage of the employed formalism consists in the identification of gauge-invariant subsets, which is based on the corresponding subsets of one-electron diagrams. This feature can be very useful in future derivations of the higher-order contributions since it provides a robust verification. Finally, we have checked the results by the comparison of the Breit approximation applied to the derived expression with the previously obtained RMBPT expressions.

This work was supported by DFG (VO1707/1-3) and by RFBR (Grant No. 19-02-00974).

References

[1] S. G. Karshenboim, Phys. Rep. **422**, 1-63 (2005).

[2] V. A. Yerokhin *et al.*, J. Phys. Chem. Ref. Data **44**, 0333103 (2015).

[3] I. Lindgren and J. Morrison, Springer Berlin (1985).

[4] W. R. Johnson, Springer Berlin/Heidelberg (2007).

[5] R. N. Soguel *et al.*, Symmetry **13**, 6 (2021).

[6] M. C. Li *et al.*, Phys. Rev. A **98**, 020502(R) (2018).

[7] V. M. Shabaev *et al.*, Phys. Rev. A **101**, 052502 (2020).

*romain.soguel@uni-jena.de

Polarization dependent electron beam pointing jitter in LWFA

B. Lei*[1,2], A. Seidel[1,2], C. Zepter[1,2], M. Zepf[1,2], and D. Seipt[1,2]

[1]Helmholtz Institut Jena, Fröbelstieg 3, 07743 Jena, Germany; [2]IOQ, FSU Jena

A self-steepened laser pulse in a plasma drives a wakefield bubble that oscillates in the laser polarization plane, called 'bubble wobble'. We theoretically and numerically show that these bubble oscillations contribute to the pointing jitter of laser-wakefield accelerated (LWFA) electrons, explaining experimental observations from the JETi-200 laser [1]. The mechanism is electron betatron oscillations becoming resonant with the bubble oscillation. Beam pointing jitter results from shot-to-shot fluctuations of the relative phase of those two oscillations, which contains contributions from the laser carrier envelope phase (CEP). Since the CEP is usually not stabilized, this phenomenon should be intrinsic in most LWFA electron beams.

An self-steepened laser pulse propagating in a plasma may excite bubble centroid (wobble) oscillations,

$$x_w(t) = a_w \sin(\omega_w t + \phi_w)\,. \tag{1}$$

The wobble amplitude can be estimated from polarization-dependent high-order correction of the ponderomotive force [2] as $a_w \propto a_0 \Phi / w_0$, where Φ is exponentially small except when the pulse has single-cycle features. The wobble frequency is determined by the rate of change of the carrier wave at the self-steepened pulse front, due to laser dispersion in the plasma and scales with $\omega_w \sim \omega_L/\gamma_p^2$. The phase ϕ_w contains a contribution from the CEP of laser pulse $\phi_{\rm CEP}$. Fig. 1 (a) and (b) show a comparison of the model with PIC simulation results.

The equation of motion of a trapped electron in a wobbling plasma bubble is a driven oscillator,

$$\frac{d^2x}{dt^2} + \frac{\dot\gamma}{\gamma}\frac{dx}{dt} + \omega_\beta^2 x = \omega_\beta^2 x_w(t)\,, \tag{2}$$

where γ is the Lorentz factor the electron and $\omega_\beta(t) = 1/\sqrt{2\gamma}$ is the betatron frequency, which continuously drops as the electrons get accelerated. The oscillator gets resonant if $\omega_\beta = \omega_w$ which is possible in a typical LWFA. For slowly varying coeffiecients, the analytic WKB solution of (2) for the beam centroid trajectory X is given by

$$X(t) = \omega_{\beta 0} \int_{t_0}^{t} A_{t'} A_t \sin\left[\varphi_t - \varphi_{t'}\right] x_w(\phi_w, t'))\,. \tag{3}$$

for a centrally injected beam, where $A_t = (\gamma_0/\gamma_t)^{1/4}$ and $\varphi_t = \int_{t_0}^{t} dt\, \omega_\beta(t')$ is the betatron phase advance. Here the assumption is that the electron beam is injected on a time scale much shorter than the wobble oscillation time scale

*b.lei@gsi.de

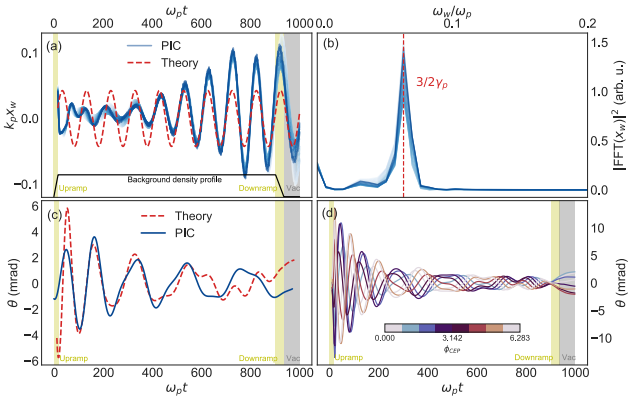

Figure 1: (a) Bubble centroid trajectory according to the model (dashed) and determined from various lineouts of the transverse focusing force (solid) calculated using the PIC code SMILEI [3]. (b) The Fourier transformation of the bubble centroid trajectory determines the wobble frequency. (c) Comparison of the betatron-wobble-resonance model and PIC simulation results for the evolution of the beam pointing angle θ. (d) Evolution of beam pointing as a function of the laser CEP from PIC simulations, yielding about 3 mrad shot-to-shot beam jitter (peak-to-valley), equivalent to $\Delta\theta \approx 1$ mrad rms.

(Bubble wobble contributes to the single-shot beam emittance in case of long injection times.). Then, the final beam pointing angle $\theta = \dot X(t_f)$ in the ultrarelativistic paraxial beam approximation. The model is compared to PIC simulations in Fig. 1 (c), the CEP dependence is shown in (d).

Calculating the moments of θ with respect to random shot-to-shot value of CEP, hence ϕ_w, shows that $\langle\theta\rangle = 0$, i.e. on average the beam is not deflected due to the resonance. The second moment, $\Delta\theta^2 = \langle(\theta - \langle\theta\rangle)^2\rangle$, describes the shot-to-shot pointing jitter. From our model we find

$$\Delta\theta^2 \simeq \frac{\omega_{\beta 0}^4 A_{t_f}^6}{8}\left|\int_{t_0}^{t_f} a_w(t') A_{t'} e^{i(\varphi_{t'} - \omega_w t')} dt'\right|^2, \tag{4}$$

which contains the resonance condition as the stationary phase condition of the integral.

In conclusion, the betatron-wobble resonance can qualitatively explain the experimentally observed polarization dependence of the beam-pointing jitter.

References

[1] See contribution by A. Seidel *et al.* in this Annual Report.

[2] E. N. Nerush and I. Y. Kostyukov, PRL **103**, 035001 (2009).

[3] J. Derouillat *et al.*, Comput. Phys. Commun. **222**, 351 (2018).

Electron Energy in Ponderomotive Scattering

Thomas Teter*[1,2,3], Daniel Seipt[1,2], and Matt Zepf[1,2,3]

[1]Helmholtz Institute Jena, Germany; [2]GSI Darmstadt, Germany; [3]Friedrich-Schiller-Universität Jena, Germany

We examine the ponderomotive scattering of electrons in rarefied noble gases by relativistic laser pulses. Electrons in a plane wave scatter at characteristic angles for a given intensity offering a route to an intensity diagnostic. Scattering angles occur at characteristic energies in the electron spectra between 1 and 10 MeV. The range of energies set requirements for electron detectors in such ponderomotive scattering experiments.

In support of upcoming strong-field QED experiments such as LUXE, we examine various techniques for measuring the intensity of the laser pulse [1]. One such technique is ponderomotive scattering, examining the final scattering angle of electrons ionized and ejected from a rarefied gas target. From the case of the relativistic electron in a plane wave, we know that the final scattering angle θ is related to the amplitude of the laser's vector potential by $\theta = \tan(2/a_0)$. For a laser focusing in a gas target, electrons are ejected with a range of angles due to the intensity distribution and diffraction. Previous experiments attempting to utilize this technique to measure laser intensity could not detect electrons at the required energies and in order to correct this we must consider those energies [2].

We utilize 3D EPOCH simulations of Kr and Xe at density $n_0 = 10^{10}$ cm^{-3} with a $w_0 = 4\,\mu$m and $8\,\mu$m spot focused in the center of the target. The peak laser strength is permuted over $a_0 = 2.77$, 5.06, and 8.7. The momenta and positions of all simulated electrons are stored in each time step after they are ionized and from these the final scattering angles and kinetic energies are calculated.

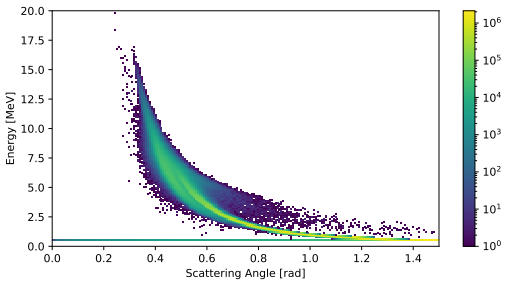

Figure 1: 2D histogram of the final kinetic energies plotted against final scattering angle for electrons in Xe for $a_0 = 8.7$ and $w_0 = 8\,\mu$m. Counts are scaled logarithmically. The band of high counts under 1 MeV are ionized at the edges of the laser and not significantly accelerated.

Figure 1 is an example histogram of final kinetic energies plotted against scattering angles. A well defined minimum scattering angle is visible at $\theta = 0.46$ (transition from from blue to green). At this angle, the energetic spectrum of Figure 2 is taken. The sharp edge corresponds spectrally to electrons with 10.4 MeV ± 1 MeV (the very low energy electrons can be ignored) . Figure 3 shows the scaling from PIC simulations for a range of laser strengths for two spotsizes. A clear dependence of the scattering angle on intensity is visible with the absolute angle a function of spot size, allowing scattering measurements combined with simulations to be used as an intensity fiducial.

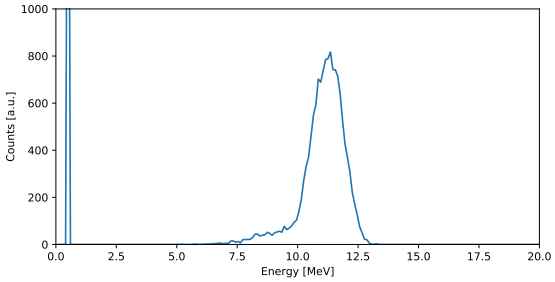

Figure 2: The energy spectrum of Fig. 1 at the point of the rising edge located at $\theta = 0.46$ rad. The band of low energy electrons lies on the left hand side. The high energy scattered electrons necessary for inferring the intensity are distributed about 10.4 MeV.

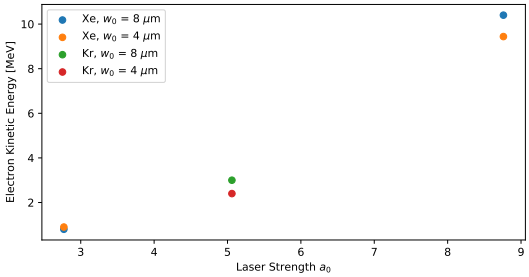

Figure 3: The central energies of electron energy spectra for two spotsizes and a range of input laser amplitudes. To detect electrons scattered by the laser focus for $a_0 > 3$, a detector must be sensitive to electrons with kinetic energies above 2.5 MeV. Xe is used for $a_0 = 2.77$ and 8.7 while Kr is used for $a_0 = 5.06$.

References

[1] H. Abramowicz *et al.*, arXiv:2102.02032.

[2] M. Kalashnikov *et al.*, Laser Part. Beams **33**, 361 (2015).

*thomas.christopher.teter@uni-jena.de

PUBLICATIONS

Z. W. Wu, Z. Q. Tian, J. Jiang, C. Z. Dong, and S. Fritzsche
Hyperfine-induced effects on the K_{α_1} angular distribution following electron-impact excitation of heliumlike spin-1/2 Tl^{79+} ions
Physical Review A **104**, 062814 (2021).

A. Weber, B. Böning, B. Minneker, and S. Fritzsche
Generation of elliptically polarized high-order harmonic radiation with bi-elliptical two-color laser beams
Physical Review A **104**, 063118 (2021).

S. Fritzsche
Dielectronic recombination strengths and plasma rate coefficients of multiply charged ions
Astronomy & Astrophysics **656**, A163 (2021).

W. Middents, G. Weber, U. Spillmann, T. Krings, M. Vockert, A. Volotka, A. Surzhykov, and Th. Stöhlker
Possible Polarization Measurements in Elastic Scattering at the Gamma Factory Utilizing a 2D Sensitive Strip Detector as Dedicated Compton Polarimeter
Annalen der Physik **534**, 2100285 (2021).

E. Appi, C. C. Papadopoulou, J. L. Mapa, C. Jusko, P. Mosel, A. Schoenberg, J. Stock, T. Feigl, S. Alisauskas, T. Lang, C. M. Heyl, B. Manschwetus, M. Brachmanski, M. Braune, H. Lindenblatt, F. Trost, S. Meister, P. Schoch, A. Trabattoni, F. Calegari, R. Treusch, R. Moshammer, I. Hartl, U. Morgner, and M. Kovacev
Synchronized beamline at FLASH2 based on high-order harmonic generation for two-color dynamics studies
Review of Scientific Instruments **92**, 123004 (2021).

J. Hornung, Y. Zobus, S. Roeder, A. Kleinschmidt, D. Bertini, M. Zepf, and V. Bagnoud
Time-resolved study of holeboring in realistic experimental conditions
Nature Communications **12**, 6999 (2021).

S. Skruszewicz, A. Przystawik, D. Schwickert, M. Sumfleth, M. Namboodiri, V. Hilbert, R. Klas, P. Gierschke, V. Schuster, A. Vorobiov, C. Haunhorst, D. Kip, J. Limpert, J. Rothhardt, and T. Laarmann
Table-top interferometry on extreme time and wavelength scales
Optics Express **29**, 40333 (2021).

A. Perry-Sassmannshausen, T. Buhr, M. Martins, S. Reinwardt, F. Trinter, A. Müller, S. Fritzsche, and S. Schippers
Multiple photodetachment of silicon anions via K-shell excitation and ionization
Physical Review A **104**, 053107 (2021).

L. Du, F. Roeder, Y. Li, M. Shalaby, B. Beleites, F. Ronneberger, and A. Gopal
Organic crystal-based THz source for complex refractive index measurements of window materials using single-shot THz spectroscopy
Applied Physics A-materials Science & Processing **127**, 846 (2021).

B. Kettle, D. Hollatz, E. Gerstmayr, G. M. Samarin, A. Alejo, S. Astbury, C. Baird, S. Bohlen, M. Campbell, C. Colgan, D. Dannheim, C. Gregory, H. Harsh, P. Hatfield, J. Hinojosa, Y. Katzir, J. Morton, C. D. Murphy, A. Nurnberg, J. Osterhoff, G. Perez-Callejo, K. Poder, P. P. Rajeev, C. Roedel, F. Roeder, F. C. Salgado, G. Sarri, A. Seidel, S. Spannagel, C. Spindloe, S. Steinke, M. J. V. Streeter, A. G. R. Thomas, C. Underwood, R. Watt, M. Zepf, S. J. Rose, and S. P. D. Mangles
A laser-plasma platform for photon-photon physics: the two photon Breit-Wheeler process
New Journal of Physics **23**, 115006 (2021).

M. Zimmer, S. Scheuren, T. Ebert, G. Schaumann, C. Rödel, M. Roth, B. Schmitz, V. Bagnoud, and J. Hornung
Analysis of laser-proton acceleration experiments for development of empirical scaling laws
Physical Review E **104**, 045210 (2021).

F. Karbstein and R. R. Q. P. T. Oude Weernink
X-ray vacuum diffraction at finite spatiotemporal offset
Physical Review D **104**, 076015 (2021).

J. Buldt, H. Stark, M. Müller, C. Grebing, C. Jauregui, and J. Limpert
Gas-plasma-based generation of broadband terahertz radiation with 640 mW average power
Optics Letters **46**, 5256 (2021).

A. G. R. Thomas and D. Seipt
Modeling chromatic emittance growth in staged plasma wakefield acceleration to 1 TeV using nonlinear transfer matrices
Physical Review Accelerators and Beams **24**, 104602 (2021).

M. Chambonneau, M. Blothe, Q. Li, V. Y. Fedorov, T. Heuermann, M. Gebhardt, C. Gaida, S. Tertelmann, F. Sotier, J. Limpert, S. Tzortzakis, and S. Nolte
Transverse ultrafast laser inscription in bulk silicon
Physical Review Research **3**, 043037 (2021).

C. Jauregui, C. Stihler, S. Kholaif, Y. Tu, and J. Limpert
Control and stabilization of the modal content of fiber amplifiers using traveling waves
Optics Express **29**, 34452 (2021).

J. B. Ohland, Y. Zobus, U. Eisenbarth, B. Zielbauer, D. Reemts, and V. Bagnoud
Alignment procedure for off-axis-parabolic telescopes in the context of high-intensity laser beam transport
Optics Express **29**, 34378 (2021).

D. Wanisch and S. Fritzsche
Delocalization of quantum information in long-range interacting systems
Physical Review A **104**, 042409 (2021).

G. Gaigalas and S. Fritzsche
Angular coefficients for symmetry-adapted configuration states in jj-coupling
Computer Physics Communications **267**, 108086 (2021).

F. C. Salgado, K. Grafenstein, A. Golub, A. Döpp, A. Eckey, D. Hollatz, C. Müller, A. Seidel, D. Seipt, S. Karsch, and M. Zepf
Towards pair production in the non-perturbative regime
New Journal of Physics **23**, 105002 (2021).

F. M. Kröger, G. Weber, S. Hirlaender, R. Alemany-Fernandez, M. W. Krasny, Th. Stöhlker, I. Y. Tolstikhina, and V. P. Shevelko
Charge-State Distributions of Highly Charged Lead Ions at Relativistic Collision Energies
Annalen der Physik **534**, 2100245 (2021).

A. V. Volotka, J. Hofbrucker, and S. Fritzsche
Steering of circular dichroism in biharmonic ionization of atoms
Physical Review A **104**, L031103 (2021).

A.-L. Viotti, S. Alisauskas, H. Tuennermann, E. Escoto, M. Seidel, K. Dudde, B. Manschwetus, I. Hartl, and C. M. Heyl
Temporal pulse quality of a Yb:YAG burst-mode laser post-compressed in a multi-pass cell
Optics Letters **46**, 4686 (2021).

F. Karbstein
Derivative corrections to the Heisenberg-Euler effective action
Journal of High Energy Physics **09**, 070 (2021).

A. Müller, M. Martins, A. Borovik Jr., T. Buhr, A. Perry-Sassmannshausen, S. Reinwardt, F. Trinter, S. Schippers, S. Fritzsche, and A. S. Kheifets
Role of L-shell single and double core-hole production and decay in m-fold ($1 \leq m \leq 6$) photoionization of the Ar^+ ion
Physical Review A **104**, 033105 (2021).

H. Abramowicz, U. Acosta, M. Altarelli, R. Assmann, Z. Bai, T. Behnke, Y. Benhammou, T. Blackburn, S. Boogert, O. Borysov, M. Borysova, R. Brinkmann, M. Bruschi, F. Burkart, K. Buesser, N. Cavanagh, O. Davidi, W. Decking, U. Dosselli, N. Elkina, A. Fedotov, M. Firlej, T. Fiutowski, K. Fleck, M. Gostkin, C. Grojean, J. Hallford, H. Harsh, A. Hartin, B. Heinemann, T. Heinzl, L. Helary, M. Hoffmann, S. Huang, X. Huang, M. Idzik, A. Ilderton, R. Jacobs, B. Kaempfer, B. King, H. Lahno, A. Levanon, A. Levy, I. Levy, J. List, W. Lohmann, T. Ma, A. J. Macleod, V. Malka, F. Meloni, A. Mironov, M. Morandin, J. Moron, E. Negodin, G. Perez, I. Pomerantz, R. Poschl, R. Prasad, F. Quere, A. Ringwald, C. Rödel, S. Rykovanov, F. Salgado, A. Santra, G. Sarri, A. Saevert, A. Sbrizzi, S. Schmitt, U. Schramm, S. Schuwalow, D. Seipt, L. Shaimerdenova, M. Shchedrolosiev, M. Skakunov, Y. Soreq, M. Streeter, K. Swientek, N. T. Hod, S. Tang, T. Teter, D. Thoden, A. I. Titov, O. Tolbanov, G. Torgrimsson, A. Tyazhev, M. Wing, M. Zanetti, A. Zarubin, K. Zeil, M. Zepf, and A. Zhemchukov
Conceptual design report for the LUXE experiment
European Physical Journal–Special Topics **230**, 2445 (2021).

B. Ying, F. Machalett, V. Huth, M. Kübel, A. M. Sayler, Th. Stöhlker, G. G. Paulus, and P. Wustelt
Experimental study of the laser-induced ionization of heavy metal and metalloid ions: Au^{+} and Si^{2+} in intense and sculpted femtosecond laser fields
Journal of Physics B–Atomic Molecular and Optical Physics **54**, 174002 (2021).

S. Fritzsche
Symbolic Evaluation of Expressions from Racah's Algebra
Symmetry **13**, 1558 (2021).

F. Karbstein, C. Sundqvist, K. S. Schulze, I. Uschmann, H. Gies, and G. G. Paulus
Vacuum birefringence at x-ray free-electron lasers
New Journal of Physics **23**, 095001 (2021).

Y. Zhang, C. L. Zhong, S. P. Zhu, X. T. He, M. Zepf, and B. Qiao
Obtaining Intense Attosecond Pulses in the Far Field from Relativistic Laser-Plasma Interactions
Physical Review Applied **16**, 024042 (2021).

B. Lei, D. Seipt, M. Shi, B. Liu, J. Wang, M. Zepf, and S. G. Rykovanov
Relativistic modified Bessel-Gaussian beam generated from plasma-based beam braiding
Physical Review A **104**, L021501 (2021).

M. Müller, C. Aleshire, J. Buldt, H. Stark, C. Grebing, A. Klenke, and J. Limpert
Scaling potential of beam-splitter-based coherent beam combination
Optics Express **29**, 27900 (2021).

A. Koszorus, L. J. Vormawah, R. Beerwerth, M. L. Bissell, P. Campbell, B. Cheal, C. S. Devlin, T. Eronen, S. Fritzsche, S. Geldhof, H. Heylen, J. D. Holt, A. Jokinen, S. Kelly, I. D. Moore, T. Miyagi, S. Rinta-Antila, A. Voss, and C. Wraith
Proton-neutron pairing correlations in the self-conjugate nucleus ^{42}Sc
Physics Letters B **819**, 136439 (2021).

Z. Sun, F. Tuitje, and C. Spielmann
A review of high-resolution microscopic ghost imaging with a low-dose pseudothermal light
Journal of Microscopy **284**, 3 (2021).

E. A. Mosman and F. Karbstein
Vacuum birefringence and diffraction at an x-ray free-electron laser: From analytical estimates to optimal parameters
Physical Review D **104**, 013006 (2021).

P. Wustelt, F. Oppermann, S. Mhatre, M. Kübel, A. M. Sayler, M. Lein, S. Graefe, and G. G. Paulus
Laser-Driven Anharmonic Oscillator: Ground-State Dissociation of the Helium Hydride Molecular Ion by Midinfrared Pulses
Physical Review Letters **127**, 043202 (2021).

J. Gollwitzer, L. Bocklage, R. Röhlsberger, and G. Meier
Connecting Fano interference and the Jaynes-Cummings model in cavity magnonics
NPJ Quantum Information **7**, 114 (2021).

P.-M. Hillenbrand, K. N. Lyashchenko, S. Hagmann, O. Y. Andreev, D. Banas, E. P. Benis, A. I. Bondarev, C. Brandau, E. De Filippo, O. Forstner, J. Glorius, R. E. Grisenti, A. Gumberidze, D. L. Guo, M. O. Herdrich, M. Lestinsky, Y. A. Litvinov, E. V. Pagano, N. Petridis, M. S. Sanjari, D. Schury, U. Spillmann, S. Trotsenko, M. Vockert, A. B. Voitkiv, G. Weber, and Th. Stöhlker
Electron-loss-to-continuum cusp in collisions of U^{89+} with N_2 and Xe
Physical Review A **104**, 012809 (2021).

R. Hollinger, E. Haddad, M. Zapf, V. Shumakova, P. Herrmann, R. Roeder, I. Uschmann, U. Reisloehner, A. Pugzlys, A. Baltuska, F. Legare, M. Zuerch, C. Ronning, C. Spielmann, and D. Kartashov
Role of free-carrier interaction in strong-field excitations in semiconductors
Physical Review B **104**, 035203 (2021).

B. Böning and S. Fritzsche
Above-threshold ionization driven by Gaussian laser beams: beyond the electric dipole approximation
Journal of Physics B–Atomic Molecular and Optical Physics **54**, 144002 (2021).

S. Willing, K. Schlage, L. Bocklage, M. M. R. Moayed, T. Gurieva, G. Meier, and R. Röhlsberger
Novel Tunnel Magnetoresistive Sensor Functionalities via Oblique-Incidence Deposition
ACS Applied Materials & Interfaces **13**, 32343 (2021).

F. Liu, Z. Chen, T. Morishita, K. Bartschat, B. Böning, and S. Fritzsche
Single-cycle versus multicycle nonsequential double ionization of argon
Physical Review A **104**, 013105 (2021).

W. Eschen, S. Wang, C. Liu, R. Klas, M. Steinert, S. Yulin, H. Meissner, M. Bussmann, T. Pertsch, J. Limpert, and J. Rothhardt
Towards attosecond imaging at the nanoscale using broadband holography-assisted coherent imaging in the extreme ultraviolet
Communications Physics **4**, 154 (2021).

F. Karbstein
Vacuum Birefringence at the Gamma Factory
Annalen der Physik **534**, 2100137 (2021).

V. Schuster, C. Liu, R. Klas, P. Dominguez, J. Rothhardt, J. Limpert, and B. Bernhardt
Ultraviolet dual comb spectroscopy: a roadmap
Optics Express **29**, 21859 (2021).

V. Schuster, V. Hilbert, R. Klas, C. Liu, M. Tschernajew, B. Bernhardt, J. Rothhardt, and J. Limpert
Agile spectral tuning of high order harmonics by interference of two driving pulses
Optics Express **29**, 22117 (2021).

M. Alamoudi, M. A. Sattari, M. Balubaid, E. Eftekhari-Zadeh, E. Nazemi, O. Taylan, and E. M. Kalmoun
Application of Gamma Attenuation Technique and Artificial Intelligence to Detect Scale Thickness in Pipelines in Which Two-Phase Flows with Different Flow Regimes and Void Fractions Exist
Symmetry **13**, 1198 (2021).

J. Hofbrucker, B. Böning, A. V. Volotka, and S. Fritzsche
Elliptical dichroism in biharmonic ionization of atoms
Physical Review A **104**, 013102 (2021).

T. Kaaden, V. Tympel, M. Kober, F. Schmidl, M. Rettenmayr, and S. Lippmann
Electric pulse heating device for the analysis of solid/solid phase transformations
Review of Scientific Instruments **92**, 074703 (2021).

G. von Gersdorff, S. Panahiyan, and W. Chen
Unification of topological invariants in Dirac models
Physical Review B **103**, 245146 (2021).

H. Gies and A. S. Salek
Curvature bound from gravitational catalysis in thermal backgrounds
Physical Review D **103**, 125027 (2021).

B. Baghdasaryan, F. Steinlechner, and S. Fritzsche
Justifying the thin-crystal approximation in spontaneous parametric down-conversion for collinear phase matching
Physical Review A **103**, 063508 (2021).

S. Salman, Y. Ma, K. Gürel, S. Schilt, C. Li, P. Pfäfflein, C. Mahnke, J. Fellinger, S. Droste, A. S. Mayer, O. H. Heckl, T. Suedmeyer, C. M. Heyl, and I. Hartl
Comparison of two low-noise CEO frequency stabilization methods for an all-PM Yb:fiber NALM oscillator
OSA Continuum **4**, 1889 (2021).

A. Gumberidze, D. B. Thorn, A. Surzhykov, C. J. Fontes, D. Banas, H. F. Beyer, W. Chen, R. E. Grisenti, S. Hagmann, R. Hess, P.-M. Hillenbrand, P. Indelicato, C. Kozhuharov, M. Lestinsky, R. Martin, N. Petridis, R. V. Popov, R. Schuch, U. Spillmann, S. Tashenov, S. Trotsenko, A. Warczak, G. Weber, W. Wen, D. F. A. Winters, N. Winters, Z. Yin, and Th. Stöhlker
Angular Distribution of Characteristic Radiation Following the Excitation of He-Like Uranium in Relativistic Collisions
Atoms **9**, 20 (2021).

Y. Ma, D. Seipt, K. Krushelnick, and A. G. R. Thomas
Generation of straight and curved hollow plasma channels by laser-generated nonlinear wakefields and studies of ultra-intense laser pulse guiding
Physics of Plasmas **28**, 063104 (2021).

Y. Ma, D. Seipt, A. E. Hussein, S. Hakimi, N. F. Beier, S. B. Hansen, J. Hinojosa, A. Maksimchuk, J. Nees, K. Krushelnick, A. G. R. Thomas, and F. Dollar
The effects of laser polarization and wavelength on injection dynamics of a laser wakefield accelerator
Physics of Plasmas **28**, 063101 (2021).

M. Müller, J. Buldt, H. Stark, C. Grebing, and J. Limpert
Multipass cell for high-power few-cycle compression
Optics Letters **46**, 2678 (2021).

R. N. Soguel, A. V. Volotka, D. A. Glazov, and S. Fritzsche
Many-Electron QED with Redefined Vacuum Approach
Symmetry **13**, 1014 (2021).

C. Gaida, M. Gebhardt, T. Heuermann, Z. Wang, C. Jauregui, and J. Limpert
Transverse mode instability and thermal effects in thulium-doped fiber amplifiers under high thermal loads
Optics Express **29**, 14963 (2021).

J. Koerner, S. Zuli, J. Reiter, M. Lenski, J. Hein, R. Boedefeld, D. Rostohar, T. Mocek, and M. C. Kaluza
Compact, diode-pumped, unstable cavity Yb:YAG laser and its application in laser shock peening
Optics Express **29**, 15724 (2021).

S. Fritzsche and A. Surzhykov
Approximate Atomic Green Functions
Molecules **26**, 2660 (2021).

T. Helk, E. Berger, S. Jamnuch, L. Hoffmann, A. Kabacinski, J. Gautier, F. Tissandier, J.-P. Goddet, H.-T. Chang, J. Oh, C. Das Pemmaraju, T. A. Pascal, S. Sebban, C. Spielmann, and M. Zuerch
Table-top extreme ultraviolet second harmonic generation
Science Advances **7**, eabe2265 (2021).

M. Ruijter, V. Petrillo, T. C. Teter, M. Valialshchikov, and S. Rykovanov
Signatures of the Carrier Envelope Phase in Nonlinear Thomson Scattering
Crystals **11**, 528 (2021).

D. Seipt, C. P. Ridgers, D. Del Sorbo, and A. G. R. Thomas
Polarized QED cascades
New Journal of Physics **23**, 053025 (2021).

D. Winzen, V. Hannen, M. Bussmann, A. Buss, C. Egelkamp, L. Eidam, Z. Huang, D. Kiefer, S. Klammes, T. Kühl, M. Loeser, X. Ma, W. Noertershaeuser, H.-W. Ortjohann, R. Sánchez, M. Siebold, Th. Stöhlker, J. Ullmann, J. Vollbrecht, T. Walther, H. Wang, C. Weinheimer, and D. F. A. Winters
Laser spectroscopy of the $^2S_{1/2}$–$^2P_{1/2}$, $^2P_{3/2}$ transitions in stored and cooled relativistic C^{3+} ions
Scientific Reports **11**, 9370 (2021).

R. N. Soguel, A. V. Volotka, E. V. Tryapitsyna, D. A. Glazov, V. P. Kosheleva, and S. Fritzsche
Redefined vacuum approach and gauge-invariant subsets in two-photon-exchange diagrams for a closed-shell system with a valence electron
Physical Review A **103**, 042818 (2021).

H. Gies, F. Karbstein, and L. Klar
Quantum vacuum signatures in multicolor laser pulse collisions
Physical Review D **103**, 076009 (2021).

S. Skruszewicz, S. Fuchs, J. J. Abel, J. Nathanael, J. Reinhard, C. Roedel, F. Wiesner, M. Wünsche, P. Wachulak, A. Bartnik, K. Janulewicz, H. Fiedorowicz, and G. G. Paulus
Coherence tomography with broad bandwidth extreme ultraviolet and soft X-ray radiation
Applied Physics B–Lasers and Optics **127**, 55 (2021).

L. Stoyanov, Y. Zhang, A. Dreischuh, and G. G. Paulus
Long-range quasi-non-diffracting Gauss-Bessel beams in a few-cycle laser field
Optics Express **29**, 10997 (2021).

S. Sadashivaiah, J. A. Wolny, L. Scherthan, K. Jenni, A. Omlor, C. S. Mueller, I. Sergueev, M. Herlitschke, O. Leupold, H.-C. Wille, R. Röhlsberger, and V. Schuenemann
High-Repetition Rate Optical Pump-Nuclear Resonance Probe Experiments Identify Transient Molecular Vibrations after Photoexcitation of a Spin Crossover Material
Journal of Physical Chemistry Letters **12**, 3240 (2021).

J. Koerner, V. Jambunathan, F. Yue, J. Reiter, P. Navratil, S. P. David, A. Lucianetti, J. Hein, T. Mocek, and M. C. Kaluza
Diode-pumped, electro-optically Q-switched, cryogenic Tm:YAG laser operating at 1.88 µm
High Power Laser Science and Engineering **9**, e11 (2021).

M. Kübel, P. Wustelt, Y. Zhang, S. Skruszewicz, D. Hoff, D. Würzler, H. Kang, D. Zille, D. Adolph, G. G. Paulus, A. M. Sayler, M. Dumergue, A. Nayak, R. Flender, L. Haizer, M. Kurucz, B. Kiss, S. Kühn, B. Fetić, and D. B. Miloševic
High-Order Phase-Dependent Asymmetry in the Above-Threshold Ionization Plateau
Physical Review Letters **126**, 113201 (2021).

J. White, S. Wang, W. Eschen, and J. Rothhardt
Real-time phase-retrieval and wavefront sensing enabled by an artificial neural network
Optics Express **29**, 9283 (2021).

S. Fritzsche, P. Palmeri, and S. Schippers
Atomic Cascade Computations
Symmetry **13**, 520 (2021).

M. Gebhardt, E. B. Amuah, R. Klas, H. Stark, J. Buldt, A. Steinkopff, and J. Limpert
Investigation of spatiotemporal output beam profile instabilities from differentially pumped capillaries
Optics Express **29**, 6957 (2021).

H. Kang, S. Chen, J. Chen, and G. G. Paulus
Frustrated double ionization of atoms in circularly polarized laser fields
New Journal of Physics **23**, 033041 (2021).

H. Stark, J. Buldt, M. Müller, A. Klenke, and J. Limpert
1 kW, 10 mJ, 120 fs coherently combined fiber CPA laser system
Optics Letters **46**, 969 (2021).

Z. Sun, F. Tuitje, and C. Spielmann
Improving the Contrast of Pseudothermal Ghost Images Based on the Measured Signal Distribution of Speckle Fields
Applied Sciences **11**, 2621 (2021).

L. Wollenweber, T. R. Preston, A. Descamps, V. Cerantola, A. Comley, J. H. Eggert, L. B. Fletcher, G. Geloni, D. O. Gericke, S. H. Glenzer, S. Goede, J. Hastings, O. S. Humphries, A. Jenei, O. Karnbach, Z. Konopkova, R. Lötzsch, B. Marx-Glowna, E. E. McBride, D. McGonegle, G. Monaco, B. K. Ofori-Okai, C. A. J. Palmer, C. Plückthun, R. Redmer, C. Strohm, I. Thorpe, T. Tschentscher, I. Uschmann, J. S. Wark, T. G. White, K. Appel, G. Gregori, and U. Zastrau
High-resolution inelastic x-ray scattering at the high energy density scientific instrument at the European X-Ray Free-Electron Laser
Review of Scientific Instruments **92**, 013101 (2021).

F. Wiesner, M. Wünsche, J. Reinhard, J. J. Abel, J. Nathanael, S. Skruszewicz, C. Roedel, S. Yulin, A. Gawlik, G. Schmidl, U. Huebner, J. Plentz, G. G. Paulus, and S. Fuchs
Material-specific imaging of nanolayers using extreme ultraviolet coherence tomography
Optica **8**, 230 (2021).

K. P. Heeg, A. Kaldun, C. Strohm, C. Ott, R. Subramanian, D. Lentrodt, J. Haber, H.-C. Wille, S. Goerttler, R. Rueffer, C. H. Keitel, R. Röhlsberger, T. Pfeifer, and J. Evers
Coherent X-ray-optical control of nuclear excitons
Nature **590**, 401 (2021).

M. Ruijter, V. Petrillo, and M. Zepf
Decreasing the bandwidth of linear and nonlinear Thomson scattering radiation for electron bunches with a finite energy spread
Physical Review Accelerators And Beams **24**, 020702 (2021).

M. Gebhardt, T. Heuermann, R. Klas, C. Liu, A. Kirsche, M. Lenski, Z. Wang, C. Gaida, J. E. Antonio-Lopez, A. Schulzgen, R. Amezcua-Correa, J. Rothhardt, and J. Limpert
Bright, high-repetition-rate water window soft X-ray source enabled by nonlinear pulse self-compression in an antiresonant hollow-core fibre
Light-science & Applications **10**, 36 (2021).

A.-L. Calendron, J. Meier, E. Kueny, S. Velten, L. Bocklage, R. Röhlsberger, and F. X. Kaertner
Bulk, cascaded pulse compression scheme and it s application to spin emitter characterization
Applied Optics **60**, 912 (2021).

M. Dragowski, M. Adamus, G. Weber, and M. Wlodarczyk
Polarized electron Mott scattering model for the Geant4 Monte Carlo toolkit
Nuclear Instruments & Methods in Physics Research Section B–Beam Interactions with Materials and Atoms **488**, 37 (2021).

S. Schippers, R. Beerwerth, S. Bari, T. Buhr, K. Holste, A. L. D. Kilcoyne, A. Perry-Sassmannshausen, R. A. Phaneuf, S. Reinwardt, D. W. Savin, S. Fritzsche, M. Martins, A. Müller, and K. Schubert
Near L-edge Single and Multiple Photoionization of Doubly Charged Iron Ions
Astrophysical Journal **908**, 52 (2021).

L. Stoyanov, M. Zhekova, A. Stefanov, B. Ivanov, I. Stefanov, G. G. Paulus, and A. Dreischuh
Generation of long range low-divergent Gauss-Bessel beams by annihilating optical vortices
Optics Communications **480**, 126510 (2021).

B. Böning, P. Abele, W. Paufler, and S. Fritzsche
A strong-field approach with realistic wave functions to the above-threshold ionization of Ba^+
Journal of Physics B–Atomic Molecular and Optical Physics **54**, 025602 (2021).

A. T. Schmitt, Y. Joly, K. S. Schulze, B. Marx-Glowna, I. Uschmann, B. Grabiger, H. Bernhardt, R. Lötzsch, A. Juhin, J. Debray, H.-C. Wille, H. Yavaş, G. G. Paulus, and R. Röhlsberger
Disentangling x-ray dichroism and birefringence via high-purity polarimetry
Optica **8**, 56 (2021).

A. Seidel, J. Osterhoff, and M. Zepf
Characterizing ultralow emittance electron beams using structured light fields
Physical Review Accelerators and Beams **24**, 012803 (2021).

S. Panahiyan and S. Fritzsche
Toward simulation of topological phenomena with one-, two-, and three-dimensional quantum walks
Physical Review A **103**, 012201 (2021).

L. Bocklage, J. Gollwitzer, C. Strohm, C. F. Adolff, K. Schlage, I. Sergeev, O. Leupold, H.-C. Wille, G. Meier, and R. Röhlsberger
Coherent control of collective nuclear quantum states via transient magnons
Science Advances **7**, eabc3991 (2021).

R. Hollinger, P. Herrmann, V. Korolev, M. Zapf, V. Shumakova, R. Roeder, I. Uschmann, A. Pugzlys, A. Baltuska, M. Zurch, C. Ronning, C. Spielmann, and D. Kartashov
Polarization Dependent Excitation and High Harmonic Generation from Intense Mid-IR Laser Pulses in ZnO
Nanomaterials **11**, 4 (2021).

B. Marx-Glowna, I. Uschmann, K. S. Schulze, H. Marschner, H.-C. Wille, K. Schlage, Th. Stöhlker, R. Röhlsberger, and G. G. Paulus
Advanced X-ray polarimeter design for nuclear resonant scattering
Journal of Synchrotron Radiation **28**, 120 (2021).

K. S. Schulze, R. Lötzsch, R. Rueffer, I. Uschmann, R. Röhlsberger, and G. G. Paulus
X-ray dichroism in polyimide caused by non-resonant scattering
Journal of Synchrotron Radiation **28**, 176 (2021).

A.-L. Viotti, S. Alisauskas, A. Bin Wahid, P. Balla, N. Schirmel, B. Manschwetus, I. Hartl, and C. M. Heyl
60 fs, 1030 nm FEL pump-probe laser based on a multi-pass post-compressed Yb:YAG source
Journal of Synchrotron Radiation **28**, 36 (2021).

S. Strnat, V. A. Yerokhin, A. V. Volotka, G. Weber, S. Fritzsche, R. A. Müller, and A. Surzhykov
Polarization studies on Rayleigh scattering of hard x rays by closed-shell atoms
Physical Review A **103**, 012801 (2021).

M. Stapelfeld, F. Schmidl, P. Seidel, S. Stück, V. Tympel, T. Stöhlker, D. Haider, M. Schwickert, T. Sieber, M. Schmelz, T. Schönau, and R. Stolz
Application Driven Optimization of Cryogenic Current Comparators (CCC) for Beam Storage Rings
IEEE Transactions on Applied Superconductivity **31**, 1600504 (2021).

R. Klas, A. Kirsche, M. Gebhardt, J. Buldt, H. Stark, S. Hädrich, J. Rothhardt, and J. Limpert
Ultra-short-pulse high-average-power megahertz-repetition-rate coherent extreme-ultraviolet light source
PhotoniX **2**, 4 (2021).

Y. Ma, S. Salman, C. Li, C. Mahnke, Y. Hua, S. Droste, J. Fellinger, A. Mayer, O. Heckl, C. Heyl, and I. Hartl
Compact, All-PM Fiber Integrated and Alignment-Free Ultrafast Yb:Fiber NALM Laser With Sub-Femtosecond Timing Jitter
Journal of Lightwave Technology **39**, 4431 (2021).

D. Wu, Z. M. Sheng, W. Yu, S. Fritzsche, and X. T. He
A pairwise nuclear fusion algorithm for particle-in-cell simulations: Weighted particles at relativistic energies
AIP Advances **11**, 075003 (2021).

B. Minneker, B. Böning, A. Weber, and S. Fritzsche
Torus-knot angular momentum in twisted attosecond pulses from high-order harmonic generation
Physical Review A **104**, 053116 (2021).

M. Almassarani, S. Meng, B. Beleites, F. Ronneberger, G. Paulus, and A. Gopal
Parametric Study of Proton Acceleration from Laser-Thin Foil Interaction
Plasma **4**, 670 (2021).

THESES

S. Hell
Space- and Polarization-Resolved Investigations of Rear Side Optical Radiation from High-Intensity Laser-Solid Interaction
Master thesis
Friedrich-Schiller-Universität Jena, Physikalisch-Astronomische Fakultät, (2021).

D. Hollatz
Detection of positrons from Breit-Wheeler pair formation
Doctoral thesis
Friedrich-Schiller-Universität Jena, Physikalisch-Astronomische Fakultät, (2021).

R. Klas
Efficiency scaling of high harmonic generation using ultrashort fiber lasers
Doctoral thesis
Friedrich-Schiller-Universität Jena, Physikalisch-Astronomische Fakultät, (2021).

S. Tietze
Compact XUV and X-Ray sources from laser-plasma interactions: theoretical and numerical study
Doctoral thesis
Friedrich-Schiller-Universität Jena, Physikalisch-Astronomische Fakultät, (2021).

N. Stallkamp
Confined ensembles of highly charged ions for studies of light-matter interaction at high intensities: the HILITE Penning trap setup
Doctoral thesis
Friedrich-Schiller-Universität Jena, Physikalisch-Astronomische Fakultät, (2021).

A. T. Schmitt
Kombination von hochpräziser Polarimetrie mit Spektroskopie im Röntgenbereich
Doctoral thesis
Friedrich-Schiller-Universität Jena, Physikalisch-Astronomische Fakultät, (2021).

J. Hornung
Study of preplasma properties using time-resolved reflection spectroscopy
Doctoral thesis
Friedrich-Schiller-Universität Jena, Physikalisch-Astronomische Fakultät, (2021).

S. Panahiyan
Toward quantum control in discrete-time quantum walks
Doctoral thesis
Friedrich-Schiller-Universität Jena, Physikalisch-Astronomische Fakultät, (2021).